



**HAL**  
open science

# Spectroscopie d'impédance appliquée au suivi chronique de la fibrose induite par implants cardiaques actifs

Amélie Degache

► **To cite this version:**

Amélie Degache. Spectroscopie d'impédance appliquée au suivi chronique de la fibrose induite par implants cardiaques actifs. Sciences de l'ingénieur [physics]. Université de Bordeaux, 2019. Français. NNT: . tel-02534728

**HAL Id: tel-02534728**

**<https://hal.science/tel-02534728>**

Submitted on 7 Apr 2020

**HAL** is a multi-disciplinary open access archive for the deposit and dissemination of scientific research documents, whether they are published or not. The documents may come from teaching and research institutions in France or abroad, or from public or private research centers.

L'archive ouverte pluridisciplinaire **HAL**, est destinée au dépôt et à la diffusion de documents scientifiques de niveau recherche, publiés ou non, émanant des établissements d'enseignement et de recherche français ou étrangers, des laboratoires publics ou privés.

THÈSE PRÉSENTÉE POUR OBTENIR LE GRADE DE

**DOCTEUR DE**

**L'UNIVERSITÉ DE BORDEAUX**

École doctorale des Sciences Physiques et de l'Ingénieur  
Spécialité Électronique

Par Amélie Degache

---

**Electrical impedance spectroscopy  
applied to the chronic monitoring of  
the fibrosis induced by cardiac  
active implants**

---

Sous la direction de Pr. Noëlle Lewis et de Pr Olivier Bernus

Soutenue le 20 Décembre 2019

Membres du jury :

DR Catherine Moali	CNRS, LBTI	Rapporteuse
PU Djilali Kourtiche	Université de Lorraine	Rapporteur
Dr. Maud Gorbet	University of Waterloo	Examinatrice
PU Olivier Romain	Université de Cergy-Pontoise	Examineur
Dr. Florence Poulletier de Gannes	CNRS, IMS	Examinatrice
PH Philippe Ritter	CHU Bordeaux	Examineur
PU Noëlle Lewis	Université de Bordeaux	Directrice de thèse
PU Olivier Bernus	Université de Bordeaux	Co-Directeur de thèse



# Résumé

Les **arythmies cardiaques** représentent environ 50% des maladies cardiovasculaires qui sont la première cause de mortalité dans le monde. Les implants médicaux jouent un rôle majeur dans le traitement de ces arythmies. En France c'est environ 250 000 patients qui sont équipés d'un implant cardiaque et qui nécessitent un suivi régulier. Ces implants utilisent les dernières technologies de micro-nano électronique et possèdent un boîtier de stimulation qui est placé en sous-cutané, connecté aux électrodes via une sonde intraveineuse. Un des principaux points faibles de tout implant réside dans l'**interface électrode-tissu**, en raison d'une réaction inflammatoire soutenue appelée la **fibrose**. Ce phénomène compromet la **biocompatibilité** de l'implant, encapsulant la sonde avec un tissu « isolant ». Cela crée des adhérences le long de la sonde et au niveau de l'électrode, ce qui entraîne souvent une hausse des seuils de stimulation au cours du temps et une diminution des durées de vie des batteries. Cette réponse est connue et peut être minimisée lors de l'implantation grâce à des sondes à élution de stéroïdes mais la fibrose reste tout de même un obstacle pour les implants, justifiant notre intérêt d'étude sur le long terme de la biocompatibilité des implants cardiaques.

La compréhension des mécanismes de la fibrose est primordiale pour ce travail. La fibrose est due à une **activation et différenciation** de certaines **cellules cardiaques** sous une contrainte mécanique, et le tissu cardiaque se retrouve modifié localement. Pour caractériser cette modification, on utilise la **mesure d'impédance** qui consiste à envoyer un courant électrique sinusoïdal  $I$  et recueillir la tension résultante  $U$  dans le tissu, l'impédance  $Z$  est le ratio  $U/I$ . en fonction de la fréquence de mesure, on peut explorer le tissu à une échelle microscopique ou macroscopique. Comme les patients sont déjà équipés de sondes cardiaques reliées à un circuit de stimulation qui peut aussi enregistrer l'activité cardiaque, l'idée principale de ce travail est d'examiner l'utilisation d'une mesure électrique qui pourrait caractériser l'encapsulation fibrotique de la sonde, avec pour objectif final d'embarquer cette méthode de caractérisation dans le circuit implanté. Cela nous amène à la problématique de ce projet : **est-ce que la fibrose qui se développe autour des sondes cardiaques a une signature électrique ?**

Mon travail de thèse s'organise en trois axes. Deux axes expérimentaux sont conduits aux **niveaux cellulaire et tissulaire**. On envisage en plus un axe discutant la faisabilité de **mesures d'impédance embarquées** pour des conditions proches de l'*in vivo*. La partie tissulaire ou *ex vivo* présente la caractérisation de différentes natures de tissu, sain ou riche en collagène, et a été développée à l'IHU LIRYC, sur des ventricules de cochons ou de brebis avec des sondes cardiaques implantées chez l'homme. Les spectres d'impédance obtenus sont analysés avec des modèles électriques connus et dont les paramètres sont extraits pour chaque type de tissus. Une analyse statistique montre que les deux natures de tissu sont caractérisées par des paramètres significativement différents. La partie cellulaire ou *in vitro* présente la caractérisation électrique, par mesure d'impédance, et biologique, par marquages immunocytochimiques, d'un modèle cellulaire de fibrose. Ce modèle est développé en cultivant des cellules cardiaques humaines, activées ou non par un facteur de croissance. Après une analyse statistique, les valeurs d'impédance des cultures activées montrent une différence significative par rapport aux cultures non activées, tandis que la caractérisation biologique montre une augmentation du nombre des cellules activées au cours du temps. Le dernier axe présente des résultats préliminaires sur de mesure d'impédance embarquée en vue d'une utilisation ultérieure *in vivo*.

Mots-clés : Bioélectronique, Spectroscopie d'impédance, Interface tissue-électrode, Pacemaker, Fibrose cardiaque



# Abstract

**Cardiac arrhythmias** represent about 50% of the cardiovascular diseases which are the first cause of mortality in the world. Implantable medical devices play a major role for treating these cardiac arrhythmias. In France, about 250.000 patients are equipped with an implanted device for arrhythmia treatment and need a regular monitoring. These devices use the latest technology of micro-nano-electronics and integrate a subcutaneous pulse generator connected to electrodes placed into the heart via intravenous leads. One of the main weaknesses of every implantable device lies in the **electrode-tissue interface** due to a sustained inflammatory response called **fibrosis**. This phenomenon jeopardizes the device **biocompatibility**, because it encapsulates the stimulation lead with an “insulating” tissue, creating adherences along the lead and often leading to an increase of the stimulation threshold over time and a larger electrical consumption. This response is well-known and minimized during the implantation surgery thanks the use of steroid-elution electrodes, however fibrosis still remains an impediment even for the most recent devices, enhancing the interest of studying long-term biocompatibility of cardiac implanted devices.

The understanding of fibrosis mechanisms is essential for this work. It consists in some **cardiac cells' activation and differentiation** under a mechanical stress, inducing fibrosis initiation and modifying locally the active cardiac tissue. To characterize this modification, we use **electrical impedance measurements**, consisting in sending a sinusoidal electrical current  $I$  and then measuring the resulting voltage  $U$  in the tissue; the impedance  $Z$  is the  $U/I$  ratio. Depending on the frequency of the measurement signal, we can explore the tissue from the microscopic to the macroscopic scales. As a patient is already equipped with cardiac leads connected to a stimulation device which can also record the cardiac electrical activity, the main idea of this work is to investigate the use of an electrical measurement that could characterize the fibrotic lead encapsulation, with the final objective to embed this characterization method in the implanted circuit. This brings us to the main question of our project: **does the fibrosis developing around the cardiac leads have an electrical signature?**

My thesis work is organized along three axes. Two experimental axes are conducted at cellular and tissue levels, on ***in vitro* or *ex vivo* models**. In addition, an axis studying the feasibility of **embedded impedance measurement** for *in vivo* mimicking conditions is also discussed. The *ex vivo* part presents the characterization of tissue of different natures, healthy or collagenous, it was developed with the IHU LIRYC laboratory, on porcine or ovine cardiac tissue (ventricles mainly), with stimulation electrodes used on patients. The impedance spectra are analysed using a known electrical model from which characteristic parameters of the two tissue types are extracted. After statistical analysis, these parameters are found to be significantly different allowing us to distinguish both tissue types. The *in vitro* part presents the electrical characterization, using impedance measurements, in parallel to the biological characterization, using immunocytochemistry, of a cellular fibrosis model. It consists in culturing human cardiac cells, activated or not by a growth factor. After a statistical analysis, the impedance values show a significantly different signature for cultures with growth factor, with respect to sham cultures, while the biological characterization confirmed the presence of more activated and differentiated cells over time. The last axis gives preliminary results of embedded impedance measurements in custom systems for later use *in vivo*.

Keywords: Bioelectronics, Impedance spectroscopy, Tissue-electrode interface, Pacemaker, Cardiac fibrosis



# Remerciements

Même si une thèse reste une aventure personnelle, il me semble présomptueux de penser qu'on puisse s'en sortir sans aide et soutien extérieurs, je me permets donc ces quelques lignes en français pour humblement remercier toutes les personnes qui m'ont accompagnée pendant ces trois années de travail et qui ont participé de près ou de loin à cet accomplissement personnel et professionnel.

Tout d'abord, je tiens à remercier Mme Catherine Moali et Mr Djilali Kourtiche, rapporteurs de ce manuscrit, d'avoir apporté leur expertise dans la lecture de mon travail, leurs questions et remarques d'une grande justesse ont permis une discussion extrêmement enrichissante et ont ouvert des pistes d'exploration pour la suite de ce travail. Mes remerciements vont également aux autres membres du jury : Mme Maud Gorbet, qui a tout de suite accepté d'évaluer mes travaux, et qui a traversé un océan pour venir discuter de mes résultats ; Mr Philippe Ritter, d'avoir pris le temps d'assister à ma soutenance et pour son recul sur les possibles applications cliniques de mes travaux ; Mr Olivier Romain, investi de la mission de président du jury, qui, malgré sa connaissance du projet, a su trouver encore des pistes d'amélioration possibles des différents systèmes utilisés au cours de mes travaux.

Mes pensées vont immédiatement vers mes deux directeurs de thèse, Noëlle Lewis et Olivier Bernus. Noëlle, merci de m'avoir permis de vivre cette aventure, de m'avoir si justement accompagnée, conseillée, encadrée, d'avoir toujours été là dans mes moments de doute comme dans mes moments d'euphorie, merci pour ces discussions scientifiques et pour ces moments de partage ; Olivier, merci de m'avoir ouvert les portes de l'IHU LIRYC, la plupart de mes résultats n'auraient pas vu le jour si tu ne m'avais pas donnée tant d'opportunités d'expérimentations, merci pour ton recul sur mon travail et pour tes conseils toujours avisés. Ces trois années à vos côtés ont été d'une richesse incroyable, vous m'avez guidée tout en me laissant une grande liberté, je me sens privilégiée d'avoir pu évoluer dans un tel environnement de travail et pour cela je vous en remercie du fond du cœur.

Je remercie le professeur Yann Deval, directeur de l'IMS, de m'avoir reçue au sein de ce laboratoire de l'Université de Bordeaux.

Je tiens à remercier Yannick Bornat, de m'avoir accueillie au sein de l'équipe EIBio. Tu as toujours eu à cœur de m'intégrer aux différentes problématiques de l'équipe malgré mes faibles connaissances en électronique et mon sujet de thèse un peu divergent des domaines de compétences de l'équipe, merci pour les gaufres du ch'Nord, ta ponctualité, ta minutie, tes efforts de vulgarisation et ta disponibilité. J'ai une pensée toute particulière pour Sylvie Renaud, merci pour ton accompagnement certes plus distant, mais toujours emprunt d'une douceur qui rend cette équipe si accueillante, et pour Gilles N'Kaoua, merci pour ta décontraction sans faille et ta capacité à trouver des solutions quand je perdais espoir.

Une équipe est certes constituée de membres permanents mais également de gens de passage, doctorants, ingénieurs et stagiaires, et je me dois de les remercier plus que chaleureusement. Je pense tout d'abord à mes contemporains qui m'ont toujours considérée comme leur égale alors qu'ils m'ont tout appris : Antoine et Jonathan, je ne sais pas si les mots suffiront à traduire ce que je ressens pour vous. Merci pour les frites marécages, les soirées Sherlock/mont d'or, nos hebdomadaires au Black Velvet, Sweeney Todd ou autres pubs bordelais, les Kebab Days et j'en passe, votre départ prématuré durant mon séjour à l'IMS a été difficile à encaisser. Antoine, j'admire ta vision de la vie, ta décontraction à toute épreuve, ta clairvoyance sur n'importe quelle situation. Merci pour les découvertes musicales et maltées, les moules/frites, d'avoir partagé ta culture qui me semble infinie quel que soit le domaine. Merci du fond du cœur pour ton soutien sans faille quand j'étais moi-même au bord de la démence, tu es et resteras une personne très chère dans mon cœur. Jonathan, collègue de bureau et ami, tu m'as toujours impressionnée par ton enthousiasme sans faille. Merci de m'avoir initiée à l'escalade, je n'oublierai jamais la force de

ta poigne, merci pour les discussions infinies au bureau, pour tous les services rendus, ton départ du bureau a été un déchirement et me remémorer ces souvenirs m'a toujours mis du baume au cœur.

Je me dois maintenant de remercier Loïc qui a pris la place vacante dans « le bureau des doctorants », deux années en ta compagnie qui sont passées à la vitesse de l'éclair. Merci pour tes conseils toujours avisés, ton aide incroyable, tes idées toujours plus innovantes, merci pour les livraisons de fromage, qui a fait son effet jusqu'en pays lyonnais. Ton dévouement m'a toujours rendue admirative et je te souhaite tout le courage du monde pour la fin de ta propre aventure l'année prochaine. Je pense également à Louis, stagiaire que j'ai eu l'honneur d'encadrer, je te remercie pour ton aide précieuse et pour ta patience malgré mon manque de connaissances en électronique. Je te souhaite de vivre une thèse aussi belle que celle que j'ai eu la chance de vivre. Enfin, un immense merci à Donnie, petit dernier de la bande, toujours le mot pour rire malgré une discrétion à toute épreuve, je te souhaite une belle expérience au sein de l'équipe.

Je tiens également à remercier chaleureusement les membres de l'équipe BioEm. Tout d'abord, Yann et Isabelle, pour m'avoir permis d'effectuer une bonne partie de mes expériences et pour vos questions toujours pertinentes. J'ai une pensée particulière pour Florence, ma deuxième maman pendant cette aventure, tu m'as tout appris en biologie, sans jamais perdre patience, toujours sécurisante, tu m'as laissée sortir des sentiers battus dans la plus grande des décontractions. Un immense merci pour ton accompagnement, il a largement dépassé le simple passage de connaissances en biologie et j'en garderai un souvenir joyeux pendant longtemps. Je veux également remercier Emmanuelle, merci pour tes conseils, pour nos échanges, je te souhaite tout l'épanouissement possible dans ton nouveau poste. Je souhaite remercier Mélody, rencontrée sur la fin de mon contrat, tu es une personne solaire comme on en rencontre peu dans sa vie, merci infiniment pour ta bonté, je suis plus que ravie d'avoir fait ta connaissance, j'espère sincèrement que c'est le début d'une belle amitié. Enfin merci à Ian, Ayelen, Yann, Alexandre, Naïa, Clément, de passage dans l'équipe qui m'ont accompagnée dans les différentes salles de manip.

Merci également à l'équipe AS2N, dernière équipe du groupe Bioélectronique qui m'a accueillie pendant ces trois années de travail, merci à Sylvain Saighi et Jean Tomas, Farad, on a commencé ensemble, on a soutenu à une semaine d'intervalle, une sacrée aventure parallèle, Charly, une collaboration de bureau haute en couleur, je te souhaite beaucoup de bonheur pour la suite.

Pour finir avec l'IMS, je souhaite remercier Valérie, pour ton accompagnement pédagogue dans l'explication de l'administratif, Simone, pour ta gentillesse à toute épreuve et ton accueil inégalé, Jocelyn et Christophe, pour votre aide précieuse dans l'exploitation de mes résultats.

Du fait d'être en co-direction, j'ai eu accès aux installations de l'IHU Lyric grâce à Olivier Bernus, que je remercie encore une fois pour toute son aide. Je tiens à remercier particulièrement Philippe Pasdois, grâce à toi j'ai obtenu une bonne partie de mes résultats de manière simple, ta patience et ton calme à toute épreuve m'ont montrée que malgré une charge de travail importante on a toujours le temps d'être pédagogue. Merci également à Marine et Virginie de m'avoir acceptée durant leurs expérimentations et je me suis toujours senti la bienvenue.

Vient maintenant le temps de remercier toutes les personnes qui ont gravité autour de moi sans participer à l'élaboration direct de ce travail mais qui m'ont motivée, conseillée et accompagnée durant ces trois années bordelaises. Je me dois de commencer par mes colocs, les différents habitants de notre humble le château : Vanille aka Vanish et Alizée aka Paris, mes amies, mes confidentes, toujours disponibles et jamais les dernières pour une petite boutade, vous êtes à l'origine de mon bien être, Antho aka Jean-Mich, pour ta culture architecturale, tes goûts musicaux inégalés et ta cuisine toujours plus innovante, Crystal te remercie, Clément aka Clemclem, ton second degré et tes conseils m'ont sauvée, on se voit au bloc pour se muscler les bibis, Sergio aka Sergione, pour ton accent charmant et tes fautes de français à tomber, pour ta cuisine, pour ton aide inconditionnelle et pour ton cœur grand comme notre appartement, un immense merci à tous d'avoir partagé ces quelques années avec moi, elles restent gravées dans ma mémoire. Une pensée particulière me pousse à partager quelques mots avec la coloc du cœur, qui dans l'adversité a eu du mal à survivre, Davide, comme dirait Chef Stefano Barbato... on ne peut faire que des progrès

en cuisine, mi manchi tantissimo, Lucie, Luigi, je vous souhaite le bonheur que vous méritez pour la suite de vos aventures, merci d'avoir fait partie de la mienne pour un temps. Je pense maintenant à tous les archis, qui ont investi la colocation de temps à autre, qui ont toujours le mot pour rire et le don de partager des repas fabuleux, merci à vous Antoine, Mimi, Lili, Thomas, Emile, Marie, Flo, Oscar, Alix... Je me dois aussi de remercier le gang des italiens bordelais, que je n'aurai rencontré sans Katrin, mon allemande au grand cœur, qui a rythmé ma vie sociale et sans qui cette aventure n'aurait pas eu la même saveur, merci à Nadia, Giovanni, Cristina, Silvia, Giuliano, Alessandro, Sally, grazie mille a tutti, siete i benvenuti a Lyon cuando volete. Merci aux mathématiciens, que je connais grâce à Sergio, Costi, tu verras Toulouse c'est cool et surtout, on se voit dans les Dolomites, Philippe, un immense merci pour ta bonne humeur et ton aide précieuse dans les derniers moments de cette thèse.

Merci à toi Mom'sou d'avoir été et d'être toujours aussi présente dans ma vie, merci à Olivier, Jérémie, Amélie, Isaure et tous les autres bordelais qui ont croisé mon chemin.

Je veux finalement remercier toutes mes copines de longues dates, présentes par intermittence mais toujours là, de vrais rocs sur lesquels je sais que je peux me reposer à tout moment : Nelly, Alice, Charlène, Bertille, Clémence, Isaure, Julie, Titi, Zoé, Nessrine, Lucile, la période où on jouait de la musique ensemble, trainait à la sortie du collège/lycée me paraît si loin et en même temps je n'ai pas vu le temps passer, MERCI ! Je ne pourrai finir sans remercier ma famille, mes parents pour votre soutien moral durant ces trois années, d'être venus me voir et découvrir un peu ma vie à Bordeaux, mes sœurs Charlotte et Camille, accompagnée d'Hugo depuis maintenant plusieurs années, pour vos venues surprises ou pas, qui m'ont toujours réchauffé le cœur, et surtout, une reconnaissance éternelle pour votre patience sans nom lors de ma soutenance, je sais que c'était un moment aussi ennuyant pour vous qu'il était exaltant pour moi.



# Table of Contents

List of acronyms .....	16
List of Figures.....	18
List of Tables.....	21
Introduction .....	22
Chapitre 1 Scientific context.....	26
1.1. The heart anatomy and functions .....	26
1.1.1. Cardiac anatomy .....	26
1.1.2. Cardiac action potential .....	27
1.1.3. Cardiac conduction system .....	30
1.2. Cardiac arrhythmias.....	31
1.2.1. Arrhythmia mechanisms .....	31
1.2.2. Cardiac arrhythmia groups.....	32
1.3. Electrotherapy.....	33
1.3.1. History of electrical stimulation .....	33
1.3.2. Artificial Pacemaker .....	37
1.3.3. Implantable Cardioverter Defibrillator.....	38
1.4. Foreign body response and biocompatibility.....	39
1.5. Objective and methodology of this PhD.....	40
1.6. Outline of the manuscript .....	41
1.7. A collaborative project .....	42
Chapitre 2 State of the art.....	44
2.1. Cardiac fibrosis and implants .....	44
2.1.1. The Cardiac Fibroblast .....	44
2.1.1.1. Generalities .....	44
2.1.1.2. Function.....	45
2.1.2. The Myofibroblast .....	46
2.1.3. Foreign body response to cardiac implants .....	46
2.1.3.1. The inflammatory response.....	47
2.1.3.2. The proliferative phase.....	48
2.1.3.3. The maturation phase .....	48
2.1.4. Fibrosis .....	49
2.2. Electrical Impedance Spectroscopy .....	50
2.2.1. Electrical properties of biological tissues .....	50
2.2.1.1. Electrolytes and ionic conductivity.....	50

2.2.1.2.	Dielectric properties of a medium .....	52
2.2.2.	Dispersion in biological tissues .....	55
2.2.3.	Electrical impedance of biological tissue.....	58
2.2.4.	Equivalent electrical models .....	60
2.2.4.1.	Equivalent model for the tissue.....	60
2.2.4.2.	Electrode-electrolyte interface .....	61
2.2.4.3.	Global equivalent model.....	62
2.2.5.	Impedance measurement .....	63
2.2.5.1.	Measurement technique.....	63
2.2.5.2.	Impedance analyzers.....	66
2.2.6.	Fields of application.....	67
2.3.	Motivation for this work.....	68
Chapitre 3 Electrical impedance spectroscopy exploration at the cardiac tissue level....		70
3.1.	Material and Methods .....	70
3.1.1.	Animal model.....	70
3.1.2.	Pacing leads.....	71
3.1.3.	Measurement bench .....	73
3.1.3.1.	Measurement principle.....	73
3.1.3.2.	Measurement protocol.....	74
3.1.3.3.	Electrode characterization .....	74
3.1.3.4.	Bench characterization .....	75
3.2.	Results.....	76
3.2.1.	Bode diagram.....	76
3.2.2.	Modelling and analysis .....	77
3.2.2.1.	Model 1.....	78
3.2.2.2.	Model 2.....	80
3.2.2.3.	Comparison between both parameters sets.....	82
3.2.2.4.	Statistical analysis and discussion.....	82
3.3.	Conclusion .....	84
Chapitre 4 Electrical impedance spectroscopy monitoring of <i>in vitro</i> cardiac fibrosis....		86
4.1.	Material and Methods .....	87
4.1.1.	Cell culture protocol .....	87
4.1.2.	Cell cultures for xCELLigence experiments .....	87
4.1.3.	Cell growth characterization .....	88
4.1.4.	Immunocytochemistry.....	89
4.1.4.1.	Principle of fluorescent staining .....	89

4.1.4.2.	Protocol.....	89
4.1.5.	xCELLigence measurements technique.....	90
4.1.5.1.	Measurement principle.....	90
4.1.5.2.	Measurement protocol.....	91
4.1.6.	Data analysis and visualization.....	91
4.2.	Results.....	91
4.2.1.	Bench characterization.....	91
4.2.2.	Cell counting.....	92
4.2.3.	Cell staining.....	93
4.2.4.	Cell Index time course.....	95
4.3.	Discussion.....	98
4.3.1.	Assessment of our characterization method.....	98
4.3.2.	Confrontation of our characterization method.....	100
4.3.3.	Potential of our characterization.....	100
4.4.	Impedance spectroscopy characterization.....	101
4.4.1.	Solartron 1260.....	101
4.4.1.1.	Measurement principle.....	101
4.4.1.2.	Measurement protocol.....	101
4.4.2.	Bench description and characterization.....	102
4.4.2.1.	Electrical characterization.....	103
4.4.2.2.	Characterization of the culture medium influence.....	107
4.4.3.	Results.....	107
4.4.4.	Discussion.....	109
4.5.	Conclusion.....	110
Chapitre 5	Preliminary results towards <i>in vivo</i> embedded measurements.....	112
5.1.	Multisine EIS evaluation on <i>in vitro</i> measurements.....	112
5.1.1.	EIS measurement bench.....	112
5.1.1.1.	Optimal excitation source.....	112
5.1.1.2.	Material constraints.....	113
5.1.1.3.	Sensing method and triggers management.....	113
5.1.1.4.	Post-processing for impedance spectrum.....	114
5.1.2.	Proof of concept on <i>in vitro</i> impedance measurement.....	114
5.2.	Orthogonal Multitone EIS (OMEIS) applied to cardiac tissues.....	115
5.2.1.	EIS measurement bench.....	115
5.2.2.	Proof of concept on cardiac tissues impedance measurements.....	116
5.2.2.1.	Static tissues in cardioplegia.....	117

5.2.2.2. Perfused tissues.....	118
5.3. Conclusion.....	119
Chapitre 6 Conclusion .....	120
Synthesis.....	120
Perspectives .....	121
Bibliography.....	124
Annexe A.....	133
Annexe B.....	135
Annexe C .....	136



# LIST OF ACRONYMS

AC	Alternative Current
AP	Action Potential
ArP	Artificial Pacemaker
AV node	Atrioventricular node
BCI	Brain Computer Interface
BIA	Bioelectrical Impedance Analysis
CF	Cardiac Fibroblast
CrF	Crest Factor
CPE	Constant Phase Element
DC	Direct Current
DMSO	Dimethyl Sulfoxide
DPBS	Dulbecco's Phosphate-Buffered Saline
ECG	Electrocardiogram
ECM	Extracellular Matrix
EIS	Electrical Impedance Spectroscopy
EIT	Electrical Impedance Tomography
FBR	Foreign Body Response
FFT	Fast Fourier Transform
FGM	Fibroblast Growth Medium
HCF	Human Cardiac Fibroblast
ICD	Implantable Cardioverter Defibrillator
IFFT	Inverse Fast Fourier Transform
IGC	Impedance Cardiography
IL-1 $\beta$	Interleukin 1Beta
LV	Left Ventricle
MF	Myofibroblast
MMP	Matrix Metalloproteinase
NCX	Sodium-Calcium Exchanger
NRMSE	Normalised Root-Mean-Square Error
OFDM	Orthogonal Frequency Division Multiple
OMEIS	Orthogonal Multitone Electrical Impedance Spectroscopy
RMSE	Root-Mean-Square Error
RV	Right Ventricle
SA node	Sinoatrial node
SNR	Signal to Noise Ratio
SVC	Superior Vena Cava
SVT	Supra Ventricular Tachycardia
TGF- $\beta$	Transforming Growth Factor $\beta$
TIMP	Tissue Inhibitor of Metalloproteinase
VT	Ventricular Tachycardia
$\alpha$ -SMA	$\alpha$ -Smooth Muscle Actin



# LIST OF FIGURES

Figure 1-1: The human circulatory system and the heart anatomy, the arrows represent the blood circulation (red for O<sub>2</sub> charged blood, blue for CO<sub>2</sub> charged blood) ..... 27

Figure 1-2: (A) Cardiomyocyte membrane with the three ionic channels of interest (Sodium, Calcium and Potassium); (B) Myocardial excitation representation, with the cells numbered in their excitation order creating an excitation wave front..... 28

Figure 1-3: Representation of the effect of an AP on a cell membrane potential, the five phases of the AP are represented by numbers from 0 to 4, and the temporal relationship with the force developed by a ventricular muscle (redrawn from Kavalier F. *et al.*, 1965) ..... 29

Figure 1-4: Cardiac conduction system, with the sinoatrial node in orange, the atrioventricular node in blue and the Purkinje fibres in red. On the right part of the figure, the different action potentials of each conducting parts of the myocardium are represented and projected on a normal ECG representation ..... 30

Figure 1-5: Schematised re-entry phenomenon ..... 32

Figure 1-6: ECG recordings for (A) a normal heart, (B) a bradycardia, (C) a Supra Ventricular Tachycardia, (D) a Ventricular tachycardia, (E) an atrial fibrillation and (F) a ventricular fibrillation..... 33

Figure 1-7: (A) Illustration of the laboratory of Galvani with limbs and electrical generators from Galvani and Aldini; (B) Hyman's device; (C) Zoll's external pacemaker; (D) First wearable pacemaker on a patient (1958) ..... 35

Figure 1-8: (A) First implanted pacemaker; (B) Roth electrode; (C) Elema-Ericsson lead ..... 36

Figure 1-9: Leadless pacemakers: (A) Empower from Boston Scientific, (B) Micra leadless pacemaker from Medtronic, (C) Nanostim from St. Jude Medical..... 37

Figure 1-10: Fibrotic encapsulation of the Micra Leadless Pacemaker, image extracted and arranged from Kypka *et al.* ..... 40

Figure 2-1: (A) from Souders et al, Circulation Research, 2009, Confocal micrograph of adult rat heart stained with phalloidin (red), DAPI (blue), and wheat germ agglutinin (green); (B) Role of cardiac fibroblast (redrawn from Souders et al, 2009) ..... 45

Figure 2-2: Schematic representation of the FBR after cardiac lead implantation into the myocardium (A) before the implantation, the myocardium contains mainly cardiomyocytes, fibroblasts and ECM components; (B) inflammatory response consisting in myocytes apoptosis and cytokines release; (C) proliferative phase with fibroblasts migration and activation into myofibroblasts; (D) maturation phase leading to tissue remodelling..... 47

Figure 2-3: The three phases of wound healing process for the skin (redrawn from Darby et al)..... 48

Figure 2-4: Schematic representation of the different type of polarizations induced by an applied electric field, (A) Electronic polarization, (B) Ionic polarization and (C) Orientational polarization ..... 54

Figure 2-5: Permittivity and conductivity spectra of a biological sample..... 56

Figure 2-6: (A) relative permittivity in the Cole-Cole representation plotted on a Wessel diagram; (B) Bode representation of the impedance of a RC series circuit (taken from Martinsen *et al*) ..... 57

Figure 2-7: Schematic representation of basic capacitor experiment with the current flow in biological tissue at low and high frequencies (redrawn from Martinsen *et al*)..... 59

Figure 2-8: (A)Representation of the Fricke's equivalent circuit of a cell with $C_m$ the surface capacitance, $R_i$ the intracellular medium resistance and $R_e$ the extracellular medium resistance; (B) Representation of the CPE model with $R_\infty$ is the combination of the lead and medium's resistances, $\Delta R$ is equivalent of $R_\infty - R_0$ with $R_0$ the charge transfer resistance.....	61
Figure 2-9: Schematic representation of the double layer capacitance at the electrode-electrolyte interface.....	62
Figure 2-10: Electrical model of the double layer impedance .....	62
Figure 2-11: Schematic representation of a typical spectrometer using ohm's law to measure impedance. The instrument can have a user interface and/or a data communication unit in order to control the instrument and read out the impedance data. ....	63
Figure 2-12: Linearly and logarithmically distributed swept-sine signals .....	64
Figure 2-13: Example of a periodic signal with a poor CrF and its amplitude histogram (right). Most signal amplitude values are concentrated in a small y-axis amplitude range (1) compared to the signal overshoot (2), extracted from Sanchez <i>et al</i> , 2012.....	64
Figure 2-14: Representation of the different broadband excitation signals, extracted from Sanchez <i>et al</i> , 2012.....	65
Figure 2-15: Schematic representation of the different electrode configurations for impedance measurements, (A) 4-electrode configuration; (B) 3-electrode configuration; and (C) 2-electrode configuration.....	66
Figure 3-1: Localisation of the healthy zone in orange and the collagen zone in green on a swine left ventricle.....	71
Figure 3-2: (A) 5554 Capsure Z Novus lead; (B) Zoom on the electrodes, the stimulation electrode pointed in orange and the counter electrode pointed in red .....	72
Figure 3-3: (A) 6947M SprintQuattro Secure lead; (B) Zoom on the pacing/sensing electrodes with the proximal electrode pointed in orange and the distal electrode pointed in red.....	72
Figure 3-4: Schematic representation of the test bench for <i>ex vivo</i> measurements.....	73
Figure 3-5: SprintQuattro and ZNovus characterization and fitting curves.....	74
Figure 3-6: Simplified R- $Z_{CPE}$ model used to fit the lead characterization measurements .....	74
Figure 3-7: Bench calibration with the measurement of three known resistances on the frequency range 1Hz-1MHz.....	75
Figure 3-8: Impedance spectra of the mean over the 6 ventricles for both healthy and collagen conditions, the grey ribbon represents the standard deviation over the 6 samples .....	76
Figure 3-9: Bode diagram of a typical bioimpedance spectrum, accompanied with the equivalent electrical circuit for both the electrode-tissue interface and the extra- and intracellular frontier.....	77
Figure 3-10: Gain and phase impedance spectra of the measured and fitted values of Model 1 for the ventricle n°6 .....	79
Figure 3-11: Magnitude and phase impedance spectra of the measured and fitted values of Model 2 for the ventricle n°6 .....	81
Figure 3-12: Box-and-whiskers plots for the parameters difference of both the healthy and collagen (ns = not significant, $p > 0.5$ ).....	83
Figure 4-1: (A) 3D representation of the xCELLigence plate used for the measurements; (B) Schematic representation of the electrodes' repartition at the bottom of the culture wells.....	87
Figure 4-2: Representation of the conditions repartition in the xCELLigence plate.....	88

Figure 4-3: Representation of the cell staining principle on a cytoplasmic protein .....	89
Figure 4-4: Schematic representation of the xCELLigence measurement bench.....	90
Figure 4-5: CI measurements of well containing the culture medium without cells .....	92
Figure 4-6: Time course of the cell counting every 24 hours during 96h, the represented values are the mean of the counting for P3 and P41 ; the solid line corresponds to an exponential fitting with regression coefficients of $R_{sham} = 0.7$ , $R_{tgf} = 0.61$ , $R_{lam} = 0.88$ , $R_{lam\_tgf}=0.85$ .....	93
Figure 4-7: Fluorescent staining of myofibroblasts for each condition represented in grey scale; the last column on the right represents a zoomed in-selection (x3) of the main cell phenotype after 96 hours of culture for each condition .....	95
Figure 4-8: Cell impedance recordings. HCFs were cultured with the four conditions described in part 2.3. For each set of measurement, the data are presented as following: the colour plot is the average value and the mean standard error is filled in grey.....	96
Figure 4-9: Box-and-whiskers plots of mean CI values for the four culturing conditions, along the three time intervals: (A) 0 to 48h, (B) 52 to 100h and (C) 104h to 148h. The significance is expressed with the letters a, b, c and d, when the letter is different, the conditions are significantly different ( $p<0,05$ ).....	98
Figure 4-10: Schematic representation of the Solartron measurement bench.....	102
Figure 4-11: Impedance spectra of the 16 wells filled with DPBS, the frequency range of the graphs is reduced to improve the readability of the measurements.....	103
Figure 4-12: Impedance spectra of the 16 wells after the application of $R_{corr}$ correction coefficient, the three xCELLigence measuring frequencies are represented; the frequency range of the graphs is reduced to improve the readability of the measurements.....	104
Figure 4-13: Magnitude and phase impedance spectra for each condition over 120 hours, each curve is the mean of 4 wells with the application of the correction coefficient; the frequency range of the graphs is reduced to improve the readability of the measurements .....	105
Figure 4-14: Magnitude and phase impedance spectra of each culturing condition for the different measuring times, the frequency range of the graphs is reduced to improve the readability of the measurements .....	106
Figure 4-15: Impedance magnitude values (mean over 4 wells) at 10kHz, 25 kHz, and 50 kHz over time, the colour plot is the average value and the mean standard error is filled in grey. ....	108
Figure 4-16: CI equivalence with the Solartron measurements for the measuring frequencies 10, 25 and 50 kHz.....	109
Figure 5-1: Photograph of the measurement bench. (a) Stimulation system, (b) Interface circuit for current sensing, (c) 16-well culture plate, (d) Oscilloscope, (e) Microcontroller, (f) Stimulator power supply.....	114
Figure 5-2: Impedance magnitude and phase graphs for one well at day 7 of fibroblasts culture.....	115
Figure 5-3: The OMEIS system board, extracted from De Roux <i>et al.</i> , 2019.....	115
Figure 5-4: Impedance magnitude measurements for 3 conditions: 'Muscle', 'Collagen' and 'CPG' the reference condition in cardioplegia. OFDM is performed at $F_s = 1\text{MHz}$ . Colored curves represent OMEIS measurements, grey ones represent Solartron measurements. ....	117
Figure 5-5: Langendorff system maintaining the ventricle in <i>in vivo</i> conditions. A picture of the ventricle in the perfusion chamber is shown on the right.....	118
Figure 5-6: Impedance magnitude of 'Muscle' and 'Collagen' conditions for the ventricle reperfused, measured by the OMEIS system at $F_s = 1\text{MHz}$ .....	119

# LIST OF TABLES

Table 2-1: Molar conductivities ( $\text{mS}\cdot\text{m}^2/\text{mol}$ ) of the main ions in biological tissues.....	51
Table 2-2: Overview table of the comparative study of the possible optimization of the broadband signals .....	65
Table 3-1: Solartron fitting parameters for both the SprintQuattro and the ZNovus leads .....	75
Table 3-2: Modelling parameters for the first model for the 6 measured ventricles.....	79
Table 3-3: Modelling parameters for the second model for the 6 measured ventricles...	81
Table 4-1: Calculated doubling times for each culturing conditions.....	93

# INTRODUCTION

## *Societal, medical and technological context*

Cardiovascular diseases are the first cause of mortality in the world, with more than 700.000 deaths per year in Europe. About half of these deaths are due to heart failure, a chronic phenomenon gradually leading to a deterioration of the cardiac pump which limits the heart capacity to send the blood to the rest of the body. The other half is due to arrhythmias or cardiac rhythm trouble.

Implantable medical devices play a major role for treating the cardiac arrhythmias. Pacemakers treat mainly bradycardia, delivering the proper stimulation signal while the implantable defibrillators are used for tachycardia, delivering an electrical shock. In France, 250.000 patients are equipped with an implanted device for arrhythmia treatment and need a regular monitoring.

These devices use the latest technology of micro-nano-electronics and integrate a subcutaneous pulse generator connected to electrodes placed into the heart via intravenous leads. One of the main weaknesses of every implantable device lies in the electrode-tissue interface due to a biological response called fibrosis. This phenomenon jeopardizes the device biocompatibility because it encapsulates the stimulation lead with an “insulating” material. This modifies the therapeutic signal, often leading to an increase of the stimulation threshold over time. This response is well-known and minimized during the implantation surgery thanks the use of steroid-elution electrodes. However, fibrosis remains an impediment for the most recent devices as leadless pacemakers or cardiac resynchronization therapy (CRT). In the first case, fibrotic encapsulation, even controlled, will induce a larger electrical consumption; for the CRT, fibrosis will affect the lead in several places, given the high number of electrodes. Finally, in the current demographic context, these devices will be implanted over longer periods of time, enhancing the interest of studying long term biocompatibility of cardiac implanted devices.

## *Scientific question*

Biocompatibility can be defined as an equipment (cardiac implantable device) capacity to not interfere with or degrade the biological environment (myocardium) with which it is in contact. In the context of active cardiac implants, this PhD focuses on fibrosis development at the electrode-tissue interface. Fibrosis mechanisms are yet not fully understood and still no method exists for its long-term in vivo characterization.

As a patient is already equipped with cardiac leads connected to a stimulation device which can also record the cardiac electrical activity, the main idea of this work is to investigate the use of an electrical measurement that could characterize the fibrotic lead encapsulation, with the final objective to embed this characterization method in the implanted stimulation circuit. This would allow performing a non-invasive monitoring of the biocompatibility of cardiac leads and find new solutions to improve it. This brings us to the main question of our project: does the fibrosis developing around the cardiac leads have an electrical signature?

## *Impedance spectroscopy approach, from cell to tissue*

The characterization technique investigated is the electrical impedance measurement, used for several decades for the characterization of biological tissues and which consists in sending a sinusoidal electrical current  $I$  and then measuring the resulting voltage  $U$ ; the impedance  $Z$  is the  $U/I$  ratio. Impedance spectroscopy is a measurement made over several frequencies, spread over a given interval. Depending on the frequency of the measurement signal, we can explore the tissue at different scales. At low frequencies, the current will pass between the cells, the cell membrane appearing as an insulator. The higher the frequency of the signal, the more the applied current will be allowed to flow through the cell membrane. Thus, at low frequencies, we will have extracellular information, by increasing the frequency of the signal we access to intracellular information.

Fibrosis has several mechanisms, from cell to tissue scales. Cardiac fibroblasts compose about 50% of the cardiac cell population, alongside cardiomyocytes and other structural cells. Under a mechanical stress, they are activated, and they differentiate into another cellular type, myofibroblasts. This phenomenon also causes a local overproduction of extracellular matrix of which collagen is an essential component. Myofibroblasts, which do not have the same morphology or function as fibroblasts, coupled with overproduction of collagen, will modify the active heart tissue locally.

## *Thesis axes of work and manuscript outline*

My thesis work is organized along three axes. Two experimental axes are conducted at cellular and tissue levels, on *in vitro* or *ex vivo* models. In addition, an axis studying the feasibility of embedded impedance measurement *in vivo* is also discussed. The manuscript is divided into five chapters.

Chapter 1 gives the minimal knowledge on the multidisciplinary context of this thesis and develops its motivation.

Chapter 2 presents a state of the art along two axes, addressing at first cardiac fibrosis, its mechanisms when induced by an implant and secondly electrical impedance spectroscopy (EIS), its theoretical aspects and applications.

Chapter 3 presents the *ex vivo* work. These experiments are carried out at the IHU LIRYC laboratory, on porcine or ovine cardiac tissue (ventricles mainly), with stimulation electrodes used on patients. Cardiac ventricles are maintained *ex vivo* at 4 °C in a cardioplegic solution, saturated in potassium leading to heartbeat inhibition. The spectrum of electrode-tissue impedance is measured from 0.1 Hz to 1 MHz, in two distinct regions of the ventricle: a "normal" region and a region containing a high proportion of collagen, close to the mitral/tricuspid valve. The impedance spectra are analyzed using a known electrical model from which characteristic parameters of the two tissue types are extracted. After statistical analysis, these parameters are found to be significantly different allowing us to distinguish both tissue types.

Chapter 4 develops the *in vitro* part, presenting the electrical and biological characterization protocols, the results and their interpretation. Human cardiac fibroblasts cultures have been developed in wells with interdigital electrodes. Their differentiation into myofibroblasts can be spontaneous or accelerated using a growth factor. These cultures are characterized electrically and biologically over time. Electrical impedance

measurements are performed with the xCelligence RTCA-DP device which provides unique cellular index (Cell Index) containing information about cell viability, proliferation and morphology; we also perform EIS over a frequency range from 1 Hz to 1 MHz, using the impedancemeter Solartron 1260. In parallel, an immunocytochemical characterization allows a visual control of cells proliferation and differentiation. After a statistical analysis, the cell index shows a significantly different signature for cultures with and without growth factor.

Chapter 5 gives preliminary results in the perspective of the chronic use of *in vivo* impedance spectroscopy. On one hand, the integration of an algorithm adapted to this measurement in implanted stimulation devices will be discussed, on the other hand *in vivo* preliminary measurements on sheeps equipped with stimulators for several months are performed. For the first part, two methods were tested: one based on a standard multi-sinus excitation signal, using a neurostimulator developed in a previous thesis at the IMS laboratory, and the other based on the OFDM technique (Orthogonal Frequency Division Multiple) developed by our collaborators from the ETIS laboratory. Both methods respect the constraint of a fast broadband measurement, for periods of time much shorter than the cardiac rhythm.



# CHAPTER I

## SCIENTIFIC CONTEXT

This first chapter is dedicated to the societal, medical and scientific issues of this multidisciplinary work which involves different fields of expertise. We will expose the bases of cardiac electrical therapies and electrical impedance allowing all the readers with either background in biology or physics to a full understanding of all the stakes of this thesis.

We will begin with the description of the different cardiac arrhythmias and their respective existing electrical therapies. Then an introduction to bioimpedance and bioelectricity will lead us to the definition of biocompatibility. Finally, the specific issues covered by this work, the experimental approach and expected achievements will be introduced.

### 1.1. The heart anatomy and functions

#### 1.1.1. Cardiac anatomy

The heart is a vital and autonomous organ of the human body and the centre of the circulatory system. It is composed of two independent parts: the right heart and the left heart, separated by a wall called the **septum** (Figure 1-1). The inner wall of the muscle is known as the **endocardium** and the outside part is called the **epicardium**. The cardiac muscle is also called the **myocardium** (Figure 1-1).

Each part contains two cavities, an **atrium** and a **ventricle** working in a coordinated way. The blood enters the atria, and then passes the ventricles to be sent to either the lungs or the rest of the body. As shown in Figure 1-1, the right and left hearts receive respectively CO<sub>2</sub> charged blood to send it to the lungs (**pulmonary circulation**), and O<sub>2</sub> charged blood from the lungs to send it to the rest of the body (**systemic circulation**). The cavities are separated by valves: the tricuspid (right part) and mitral (left part) separating the atria from the ventricles and the pulmonary and aortic valves separating the ventricles from the circulatory system. Thanks to these valves, the blood can only follow one direction and is not allowed to enter the heart from the ventricles for example.

The myocardium is composed of various cell types; in proportion of about 30% **cardiomyocytes** (contractile cells) and 70% non-myocyte cells like **fibroblasts**, endothelial cells and smooth muscle cells [1], [2]. Nevertheless, the cardiomyocytes represent about 70-80% in volume of the cardiac muscle.

The heart has both mechanical and electrical properties: its mission to send the blood through the body is achieved by its mechanical ability to contract its cavities. This action is triggered by its electrical functions.

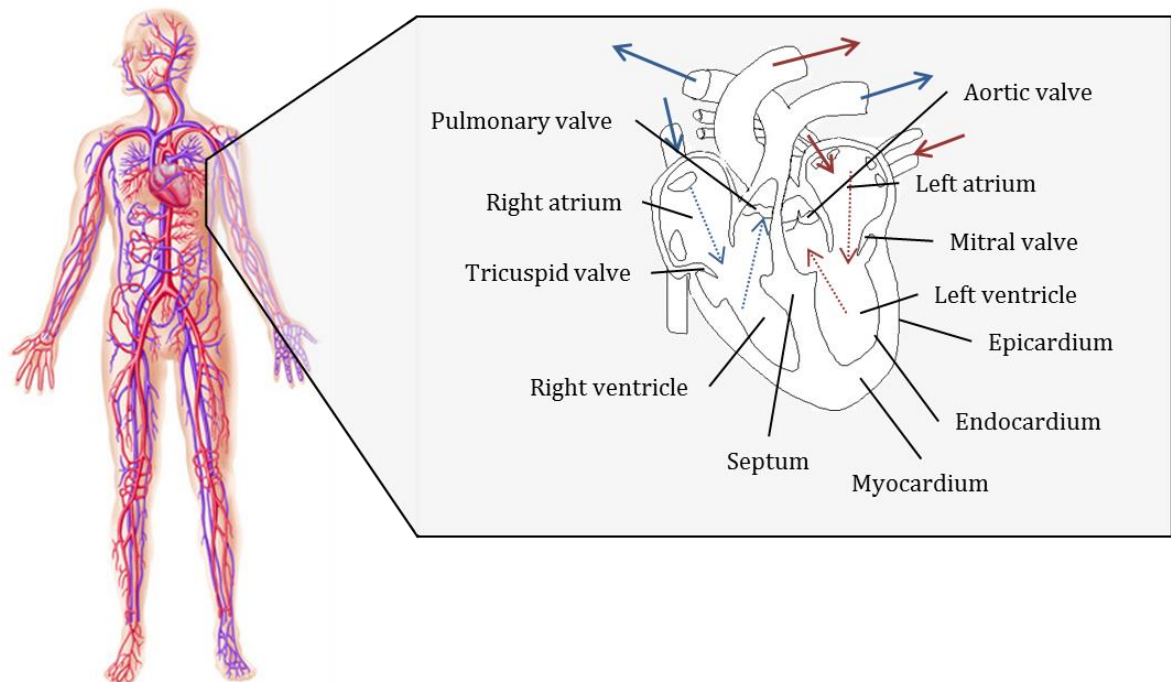


Figure 1-1: The human circulatory system and the heart anatomy, the arrows represent the blood circulation (red for O<sub>2</sub> charged blood, blue for CO<sub>2</sub> charged blood)

### 1.1.2. Cardiac action potential

The cardiomyocyte's contractions follow the electrical activation sequence largely determined by the cardiac conduction system. It is composed of three main parts: the **sinoatrial node** (SA node), the **atrioventricular node** (AV node) and the **Purkinje fibres** (Figure 1-4), which will be described in part 1.1.3. This conduction system is autonomous and independent. These three components of the cardiac conduction system are composed of cells that have the ability to spontaneously produce an electrical impulse: **an action potential** (AP).

These particular cells, represented by the cell 1 in Figure 1-2.B, have a property called automaticity meaning that this type of cell does not need a neighbouring cell to induce an AP. They are at the origin of APs that will spread into the myocardium through the main conduction paths.

The cell membrane is a semi-permeable barrier between the intra and extra cellular medium. The concentration gradient of the different ionic species from both sides of the cellular membrane induces a membrane potential of about -90 mV. The most important ionic species for the cardiomyocytes are the potassium K<sup>+</sup> with an extracellular concentration lower than the intracellular one ( $[K^+]_o \ll [K^+]_i$ ), the calcium Ca<sup>2+</sup> ( $[Ca^{2+}]_o \gg [Ca^{2+}]_i$ ) and the sodium Na<sup>+</sup> ( $[Na^+]_o \gg [Na^+]_i$ ). The corresponding ionic channels are represented on Figure 1-2.A.

The AP is caused by ion movements between the inside and outside of the cell [3]. Different transport mechanisms exist: the **diffusion** (ion channels) which is a passive mechanism and dependent of the membrane potential, and the **ion pumps or exchangers** (ion pumps and voltage-gated ion channels) which are active mechanisms. The detailed mechanisms that allow the ions to cross the membrane [4] are:

- The **ion channels** are highly selective and allow only certain ions to pass the membrane. The movement of ions through the ion channels is driven by the ionic concentration gradient from either side of the ion channels. For example, if a cardiomyocyte voltage is negative relative to the outside, positively charged ions will be forced into the cell, or if the extra- and intracellular ion concentrations are different, ions will be driven in the direction of the lowest concentration. The **voltage gated ion channels** are a specific type of ion channels sensitive to the voltage across the cell membrane. If the voltage reaches a certain level, the channel opens and stays open for a limited amount of time. It exists three important voltage gated ion channels in the cardiac myocytes, respectively the Sodium ( $\text{Na}^+$ ) Channel which is a very fast channel (open for about 1 ms), the Calcium ( $\text{Ca}^{2+}$ ) Channel which is a slow channel (open for several tens of ms) and the Potassium ( $\text{K}^+$ ) Channel which is a slow channel (open for tens of ms).
- The **ion pump** is a mechanism allowing ions to pass the membrane against the concentration gradient. The **ion exchanger** allows the swap of an ion species for another, one very important exchanger for the cardiomyocytes' contraction mechanism is the Sodium-Calcium exchanger (NCX).

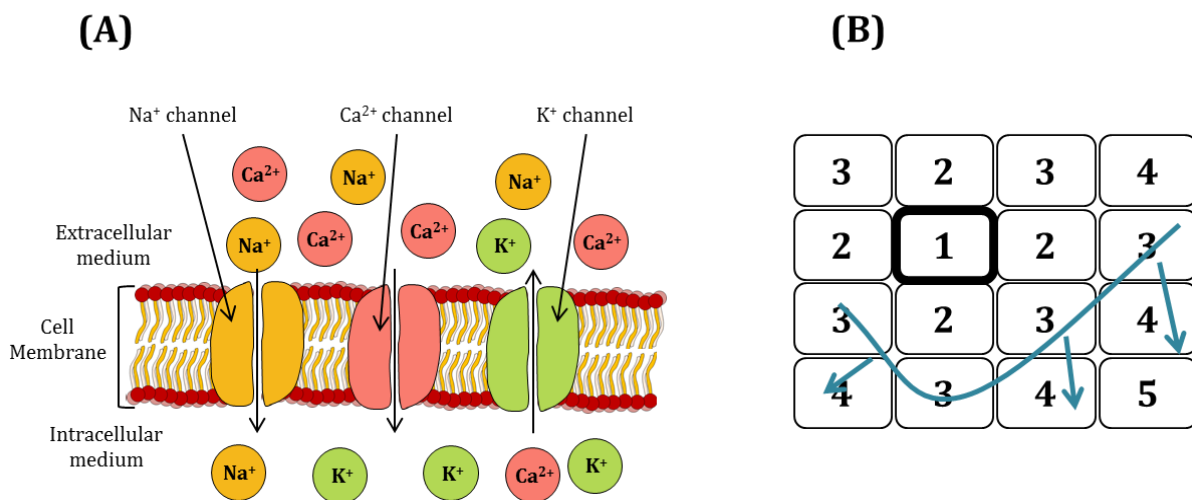


Figure 1-2: (A) Cardiomyocyte membrane with the three ionic channels of interest (Sodium, Calcium and Potassium); (B) Myocardial excitation representation, with the cells numbered in their excitation order creating an excitation wave front

The AP will spread along the cardiac tissue from cell to cell as shown in Figure 1-2.B. For a cell, the AP is divided into five phases, starting from the resting phase where the membrane potential is about -90 mV. The different phases of a cardiac AP for the ventricular cardiomyocytes are:

- Phase 0 or the **Rapid Depolarization** is started once the membrane potential reaches a certain 20 mV threshold due to neighbouring cell depolarization, driving the membrane potential increase to about -70 mV. This produces the activation of the voltage gated Na<sup>+</sup> channels, and a rapid influx of Na<sup>+</sup> ions into the cell, corresponding to the upstroke of the AP and the depolarization of the cell membrane to about +20 mV. This phenomenon takes place in only few milliseconds.
- Phase 1 or the **Early Rapid Repolarization** is due to the closing of the Na<sup>+</sup> channel after the immediate depolarization and the opening of the K<sup>+</sup> channels, allowing the K<sup>+</sup> ions to flow out of the cell. This induces a drop in the potential membrane to about +5 mV.
- Phase 2 or the **Plateau** is induced by the opening of voltage gated Calcium (Ca<sup>2+</sup>) channels allowing Ca<sup>2+</sup> ions to enter the cell, the K<sup>+</sup> channels are still open permitting the K<sup>+</sup> ions to exit the cell. These channels are slow-changing, and the potential will remain stable for about 150 ms.
- Phase 3 or the **Final rapid Repolarization** is caused by the inactivation of the Ca<sup>2+</sup> channels and the remaining activation of the K<sup>+</sup> channels. The membrane potential will lower rapidly as the K<sup>+</sup> ions continue to flow out of the cell, in about 100 ms.
- Phase 4 or the **Resting Stage** is reached when the membrane potential is back at its resting value of -90 mV. The K<sup>+</sup> channels will then be inactivated and the cell stays at its resting state until the next AP comes.

These five phases are represented in Figure 1-3 in parallel with the muscle contraction. The rapid depolarization (phase 0) precedes the force development, the plateau and the repolarization coincides approximately with the peak force and the duration of the contraction parallels the duration of the action potential [5], [6].

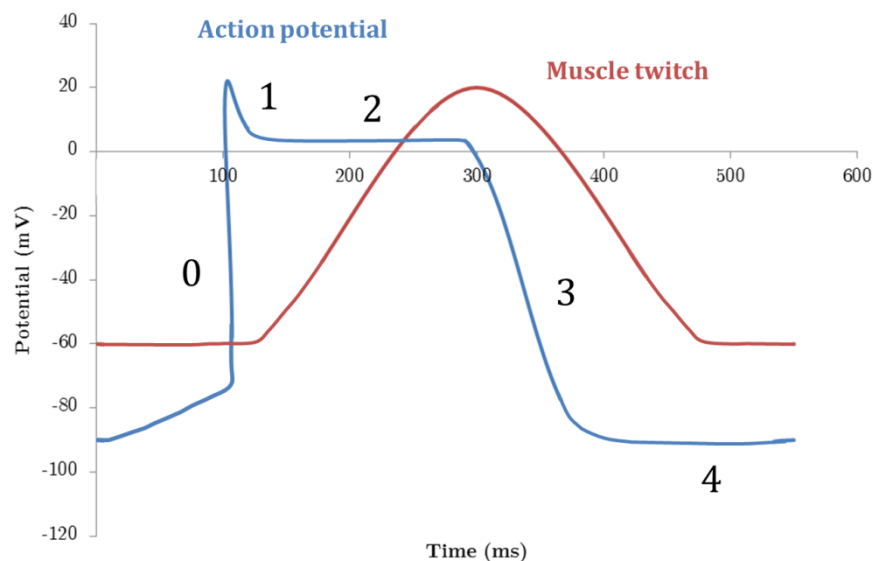


Figure 1-3: Representation of the effect of an AP on a cell membrane potential, the five phases of the AP are represented by numbers from 0 to 4, and the temporal relationship with the force developed by a ventricular muscle (redrawn from Kavalier F. *et al.*, 1965)

### 1.1.3. Cardiac conduction system

The cardiac conduction system is composed of three main parts introduced in the part 1.1.2. It is composed of a specialized conducting tissue spreading the electrical signals from the atria to the ventricles<sup>1</sup>. This function is controlled predominantly by the autonomic nervous system.

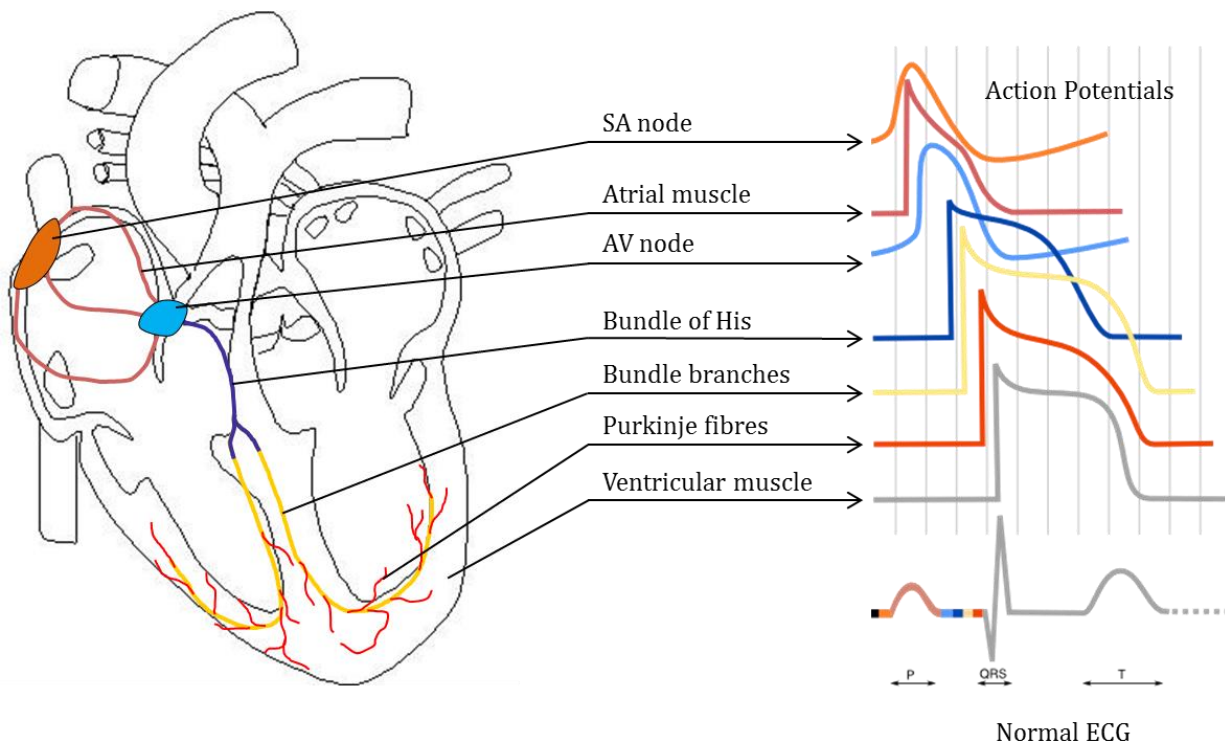


Figure 1-4: Cardiac conduction system, with the sinoatrial node in orange, the atrioventricular node in blue and the Purkinje fibres in red. On the right part of the figure, the different action potentials of each conducting parts of the myocardium are represented and projected on a normal ECG representation

This conduction system is represented on Figure 1-4<sup>1</sup> with the corresponding action potentials depending on the part of the conductive system. The different action potentials are reported on the representation of a normal electrocardiogram (ECG).

- The **SA node** is a small structure (about 10-20 mm long for 2-3 mm wide) and contains pacemaker cells which discharge synchronously resulting in an activation wave front activating the rest of the atrium as shown in Figure 1-2.B. In a healthy heart, the SA node (primary automatism centre) continuously produces action potentials, about 60 to 100 every minute, setting the rhythm of the heart and so is known as the **heart's natural pacemaker**.
- The **AV node** facilitates the conduction between atria and ventricles and lies in the lower back section of the interatrial septum. It is known as the secondary automaticity centre, with an intrinsic rate at about 40 to 60 AP per minute. Once

<sup>1</sup> [https://www.textbookofcardiology.org/wiki/Cardiac\\_Arrhythmias#Cardiac\\_conduction](https://www.textbookofcardiology.org/wiki/Cardiac_Arrhythmias#Cardiac_conduction)

the signal has reached the AV node, it enters a fast-conducting system called the **Bundle of His**. The Bundle of His and its two **branches** lead to the Purkinje fibres. The two bundle branches allow spreading the electrical signal to both left and right ventricles. The AV node has a **slow conduction** that induces the delay between the atria and the ventricles contractions (delay between the P wave and the QRS complex on the ECG).

- The **Purkinje fibres** are a network of fibres in the ventricle's walls, just beneath the endocardium. They are known as the tertiary automaticity centre, able to fire about 15 to 40 times per minute. They have a very **fast conduction** for a simultaneous contraction of the ventricles.

The three automaticity centres are prioritized from the fastest (SA node) to the slowest (Purkinje fibres). If the primary pacemaker is defective, the second automaticity centre will take over the AP production and so on. The resting heartbeat rate is considered clinically normal at about 60 beats per minute, a brutal change at a resting state can be dangerous if not controlled, for the patient.

## 1.2. Cardiac arrhythmias

A cardiac arrhythmia is defined as a cardiac rhythm disorder resulting from an irregularity in rhythm, rate or the origin of activation. Cardiac arrhythmias then have different origins and induce several cardiac diseases. They are a medical condition in which the heart does not beat with a regular rhythm or at the normal rate<sup>2</sup>. We will first discuss the arrhythmia mechanisms and then we will expose the different types of cardiac arrhythmias.

### 1.2.1. Arrhythmia mechanisms

Structural abnormalities or electrical changes in the cardiomyocytes can impede AP formation or change cardiac propagation, therefore inducing arrhythmias. Mechanisms can arise in single cells (automaticity, triggered activity), others require multiple cells (re-entry) [7]. There are two main types of mechanisms<sup>3</sup>:

- The **abnormal impulse formation** can come from *abnormal automaticity* or *triggered activity*. Abnormal automaticity can be caused by changes in the cell ion channel characteristics due to drugs or to the tissue environment (myocardial infarction). Triggered activity is a depolarization of the cell membrane produced by a preceding activation. Early depolarizations are induced by a disturbance of the balance of influx or efflux of ions during the plateau phase and delays

---

<sup>2</sup> <https://dictionary.cambridge.org/fr/dictionnaire/anglais/arrhythmia>

<sup>3</sup> [https://www.textbookofcardiology.org/wiki/Cardiac\\_Arrhythmias#bibkey\\_Berne](https://www.textbookofcardiology.org/wiki/Cardiac_Arrhythmias#bibkey_Berne)

afterdepolarizations are due to an abnormal  $\text{Ca}^{2+}$  handling of the cell, releasing  $\text{Ca}^{2+}$  ions into the cell and therefore increasing the membrane potential.

- The **disorder of impulse conduction** can come from the *conduction block* or the *re-entry* [8]. Conduction block is induced by the slowdown or the interruption of the electrical signal through the myocardium and re-entry develops when the electric signal follows a circular pathway, as represented on Figure 1-5<sup>4</sup> with a slow and a fast conducting ways, reactivating the recovered surrounding myocardium [9].

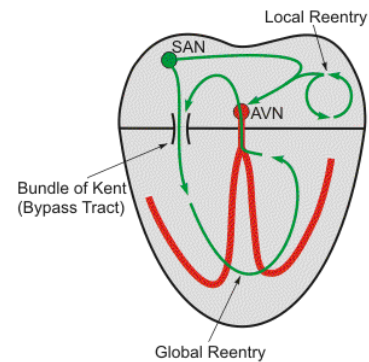


Figure 1-5: Schematised re-entry phenomenon

These mechanisms induce different types of arrhythmias which we describe in the following part. The ECG recordings of different types of arrhythmias are represented in Figure 1-6<sup>5</sup>.

## 1.2.2. Cardiac arrhythmia groups

The four main types of arrhythmias are the following:

- **Tachycardia**, which presents a resting heartbeat rate faster than a normal heartbeat and regular, with more than 100 beats per minute, it can arise from the re-entry phenomenon. Two main types of tachycardia exist, the Supra-Ventricular (SVT's, Figure 1-6.C) and the ventricular (VT's, Figure 1-6.D) tachycardias<sup>6</sup>. SVT's originate in the atria or in the AV node; they are quite common and rarely life-threatening. VT's are rhythm disorders from the ventricles.
- **Bradycardia**, which presents a resting heartbeat rate slower than a normal heartbeat and regular, with less than 60 beats per minute, typically arises from the conduction block phenomenon. This type of arrhythmia is rarely life-threatening and its ECG recording can be seen in Figure 1-6.B.
- **Fibrillation**, which corresponds to a fast and disordered heartbeat rate, it can arise from the triggered activity or the abnormal automaticity. Both atrial (Figure 1-6.E) and ventricular (Figure 1-6.F) fibrillations exist, the first having a limited consequence depending on the disease, nevertheless the second one is one of the most serious arrhythmias, without an immediate medical intervention, it leads to the death of the patient.

<sup>4</sup> <https://www.cvpphysiology.com/Arrhythmias/A008c>

<sup>5</sup> <https://ecg-educator.blogspot.com/>

<sup>6</sup>

[https://www.textbookofcardiology.org/wiki/Tachycardia#Differentiation\\_between\\_SVT\\_and\\_VT](https://www.textbookofcardiology.org/wiki/Tachycardia#Differentiation_between_SVT_and_VT)

- **Extra systole**, which consists in the production of extra beats appearing between two regular heartbeats, originating from the triggered activity or the abnormal automaticity. If they are only few, their dangerousness is not a concern.

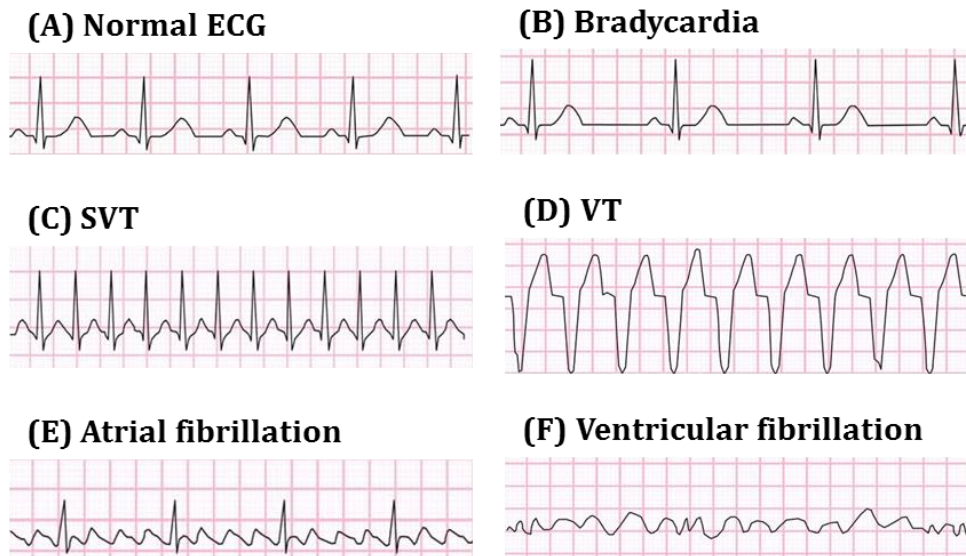


Figure 1-6: ECG recordings for (A) a normal heart, (B) a bradycardia, (C) a Supra Ventricular Tachycardia, (D) a Ventricular tachycardia, (E) an atrial fibrillation and (F) a ventricular fibrillation

As we can see, the different arrhythmias arise from different mechanisms and have different treatments which can be either by drugs ingestion or using an electrical therapy.

### 1.3. Electrotherapy

Electrical stimulation is a widely used technique to induce physiological reactions in excitable cells and tissue, for a wide range of therapeutic applications. In the case of cardiac pathologies, the implantation of electrical stimulators is a common procedure nowadays. We will go through a quick historical presentation of the cardiac electrical therapy and then we will describe the two main types of implantable devices for the cardiac application.

#### 1.3.1. History of electrical stimulation

The discovery of bioelectricity has been made about two thousand years ago [10]. The first modern foundation of experimental electrophysiology was performed around 1660 by the Dutch biologist Jan Swammerdam. His setup was based on a nerve-muscle preparation, on which an “irritation” of the nerve can be performed, inducing a

mechanical reaction of the muscle. The irritation was performed with a silver wire that could cause electrical stimulation [11].

First enhancements of the stimulation were made at the end of the 18<sup>th</sup> century. The first demonstration of a stimulation basic circuit was performed after the invention of Leyden jar, the first electrical storage device. The best example is the experiment performed by Galvani and Aldini [12] on “animal electricity”. This experiment illustrated the electrical nature of the neural impulse and allowed a first investigation correlating stimulation strength and mechanical response; we can see an illustration in Figure 1-7.A. It was also the first demonstration of functional electrical stimulation on a limb. Similar experiments were performed by Volta at the beginning of the 19<sup>th</sup> century [13]. In a letter dated of 1800, A. Volta signed a major contribution on both electrophysiology and electrical engineering, with the design of the first electrochemical battery; Volta described effects of this electricity on body, and wrote the first description of “crackling and boiling” sensations.

The work of Michael Faraday was important both in electrochemistry and for the discovery of magnetic induction, and he was also interested in bioelectricity. In 1820, H.C. Ørsted published his discovery of the relationship between flowing electricity and magnetism [14]. In 1831, Faraday invented the induction coil which became important for bioelectric research and practical use [15]. In continuation, the work of M. Faraday and N. Tesla allowed to develop new sources of electricity with high-voltage/current pulses [15]. In parallel, the detection of small bioelectric current became possible with the apparition of the first galvanometers in the 1820's. After about 20 years of technological improvements (increasing the sensitivity and developments of new sources able to follow the rapid changes of muscles and nerve currents), Matteucci was able to measure the first muscle current impulses in 1838 [16].

The first human electrocardiogram (ECG) was measured in 1887 with a capillary galvanometer by August Waller [17], [18]. Nevertheless, this type of galvanometer was not quick enough to record a reliable ECG curve. In 1903, Willem Einthoven presented a new sensitive and quick quartz string galvanometer to record correct ECG curves [19]. Three leads were used to construct Einthoven's triangle, an important concept to this day [20]. In 1924, Einthoven was awarded the Nobel Prize in physiology and medicine for the invention of electrocardiograph. In 1942, the 12-leads electrocardiogram as we know it today was completed.

In the early 1930's, the first pacing machines appeared and the credit for the first external cardiac pacemaker has been shared by two doctors: the Australian anaesthesiologist Mark Lidwell and the American physiologist Albert Hyman. A. Hyman became interested in reviving the “stopped heart” by means of “intracardial (his term) therapy”. Initially this therapy consisted of the intra-cardiac injection of stimulant drugs but soon he realised that it was possible using electricity.

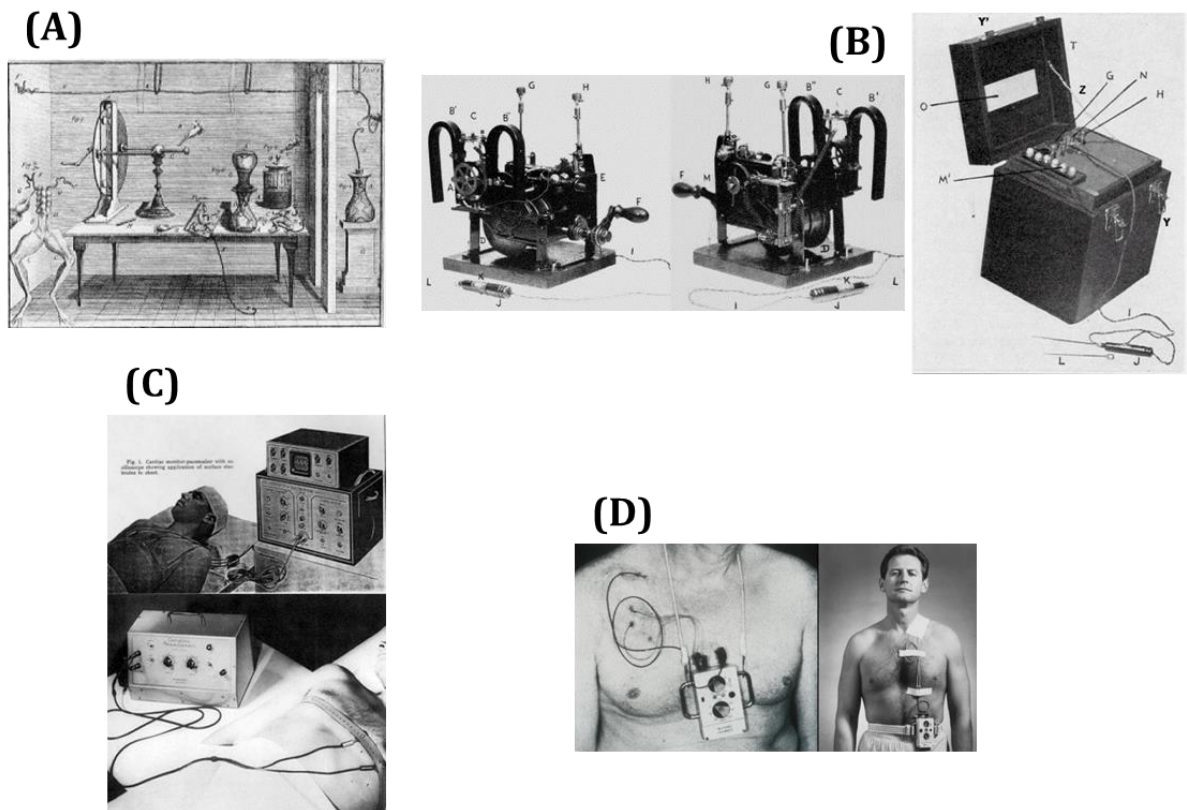


Figure 1-7: (A) Illustration of the laboratory of Galvani with limbs and electrical generators from Galvani and Aldini; (B) Hyman's device; (C) Zoll's external pacemaker; (D) First wearable pacemaker on a patient (1958)

Hyman's device (Figure 1-7.B), described in 1932, was powered by a spring-wound hand-cranked motor and called by Hyman himself an “artificial pacemaker”, a term still in current use.

Unfortunately, no one agreed to manufacture such a device and we had to wait until the early 1950's for the development of the first mains-powered portable pacemakers, portable only in name as they need an electrical outlet to work.

In 1951, Paul Zoll developed an external table-top pacemaker as we can see in Figure 1-7.C, successfully used in the treatment of heart block and containing an electrocardiograph to monitor the cardiac rhythm and an electric pulse generator to pace the heart. The signal, a periodic electric impulse (2 ms duration, and 50 to 150 V alternating voltage) was delivered through a pair of metal electrodes strapped to the patient chest. In 1956, applying transthoracic electric shocks, he managed to reverse ventricular fibrillation in man [21].

The late 1950's and early 1960's are known as the 'Golden years' in the field of cardiac pacing, witnessing important achievements in devices development. In 1957, the first **battery-operated wearable pacemaker** was produced by Earl E. Bakken, co-founder of Medtronic Inc. in 1949. By the mean of a myocardial wire implanted, either by a stab incision or through a hollow needle, directly into the myocardium, effective pacing of 1.5 V were sufficient and the wire easily removable once normal conduction resumed (example of the 5800, Medtronic Inc., 1958, (Figure 1-7.D). Bakken's work allowed the

first successful applications of transistor technology to medical devices helping to launch the new field of “medical electronics” [22], [23]. In 1958, the first **totally implantable pacemaker** (Figure 1-8.A) was implanted in Sweden [24] on a hopeless patient with a complete heart block. The generator delivered impulses of 2 V with a width of 1.5 ms; the pulse rate was fixed at 70 to 80 beats per minute. The whole device was entirely handmade. The patient lived until 2001 with five leads systems implanted over time and 22 different pulses generator of 11 different models, his death was totally unrelated to his cardiac implant or his conduction tissue.

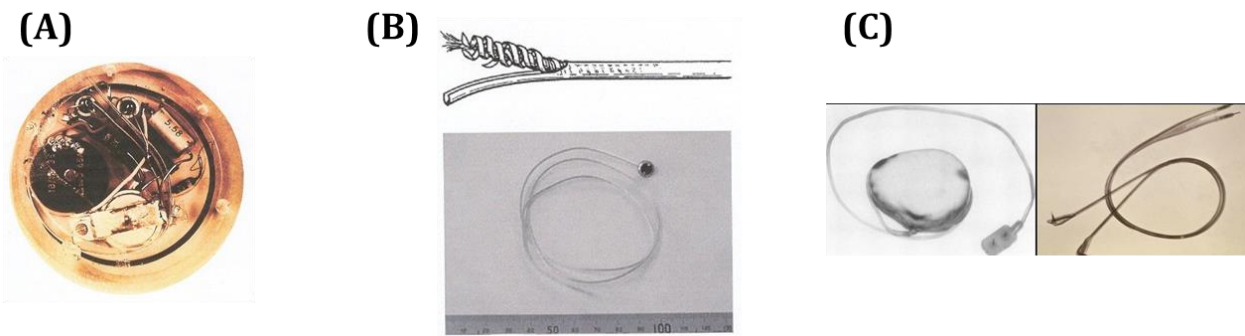


Figure 1-8: (A) First implanted pacemaker; (B) Roth electrode; (C) Elema-Ericsson lead

As we described just above, the 1950’s and the 1960’s permitted a great breakthrough in the pacing technology through a tight collaboration between engineers, physicians and patients. Over 2 million pacemakers have been implanted worldwide since 1960 [22]. Major progresses have been achieved also on the lead part with the **Roth electrode** (bipolar stainless steel electrode secured in a silicone rubber base) represented in Figure 1-8.B and the **Elema-Ericsson lead** that can be seen in Figure 1-8.C (four thin bands of stainless steel wound around a core of polyester braid and insulated with soft polyethylene with a unipolar platinum epicardial electrode) [22]. The transvenous leads replaced the epicardial leads in the mid 1960’s.

In the mid 1970’s, the pacemakers became non-invasively programmable, and by the end of the 1970’s dual-chambers pacemakers were developed to pace and sense in both atria and ventricles. The main companies of this medical field were founded in the 1970’s decade: Guidant Corporation (1972, now part of Boston Scientific), St. Jude Medical (1976), and became the main competitors. In the early 1980’s, **steroid eluting leads** were developed decreasing the inflammatory response post-implantation [25]. Nowadays, the major actors in the field of implantable cardiac devices are Medtronic, St. Jude Medical, Johnson and Johnson (Biosense Webster) and Guidant Corporation (Boston Scientific).

As we can see, the development of the cardiac pacing technology arose quickly, in only two decades, due to the breakthrough of the semi-conductor industry. The invention of the silicon transistor, opening the era of integrated circuits and computers, coupled with advances in battery technology, accelerated the miniaturization of medical devices that could move from “portable” to “implantable”. At the same time, the leads have known also great improvements in their manufacture but also concerning their biocompatibility (see

Part 1.4.). In 2014, the first leadless pacemaker, Micra from Medtronic Inc. (Figure 1-9.B<sup>7</sup>), was implanted in a patient [26], [27]. St. Jude Medical and Boston Scientific also developed their own leadless pacemakers respectively Nanostim (Figure 1-9.C<sup>8</sup>) and Empower (Figure 1-9.A<sup>9</sup>).



Figure 1-9: Leadless pacemakers: (A) Empower from Boston Scientific, (B) Micra leadless pacemaker from Medtronic, (C) Nanostim from St. Jude Medical

The different types of arrhythmias described in part 1.2.2. do not require the same treatment and we will now see the two main sorts of existing electrical therapies.

### 1.3.2. Artificial Pacemaker

An implantable stimulator, also called an **Artificial Pacemaker** (AP, not to be confused with the natural pacemaker which is the heart) is a medical implantable device that generates electrical impulses delivered by electrodes to stimulate the myocardium and regulate the electrical activity of the heart<sup>10</sup>. The primary purpose of a pacemaker is to maintain an adequate heart rate, either because the heart's natural pacemaker is not fast enough, or because there is a block in the heart's electrical conductive system. They are normally used to treat bradycardia, atrial fibrillation, heart failure (dyssynchrony) and syncope.

Nowadays, pacemakers are externally programmable and allow a cardiologist to set the optimum pacing mode individually for patients. Some devices combine a pacemaker and a defibrillator in a single implantable device while others have multiple electrodes stimulating different positions within the myocardium to improve the synchronisation of the ventricles.

Implantable pacemakers involve transvenous placement of one or more pacing electrodes in one or more cavities of the heart, while the pacemaker is implanted under the skin under the collar bone. The procedure is performed by incision of a suitable vein into which the electrode lead is inserted and passed along the vein, through the valve of the heart, until positioned in the chamber. The procedure is facilitated by fluoroscopy or angiography which enables the monitoring of the lead's passage. Once it is correctly

<sup>7</sup> <https://www.medscape.com/viewarticle/854527>

<sup>8</sup> <https://health.usnews.com/health-news/patient-advice/articles/2015/10/14/next-in-heart-pacemakers-look-no-leads?offset=20>

<sup>9</sup> <https://www.mddionline.com/exclusive-details-boston-scientifics-leadless-pacer-emerge>

<sup>10</sup> [https://everipedia.org/wiki/lang\\_en/Artificial\\_cardiac\\_pacemaker/](https://everipedia.org/wiki/lang_en/Artificial_cardiac_pacemaker/)

located, the opposite end of the lead is connected to the pacemaker generator. The battery in the generator lasts 5 to 10 years and must be replaced when it runs out<sup>11</sup>.

There are different types of artificial pacemakers, classified according to the number of cavities involved and their basic operating mechanism<sup>11</sup>:

- **Single Chamber Pacemaker** has one wire placed in the right upper chamber (atrium) or lower chamber (ventricle).
- **Dual Chamber Pacemaker** has two leads, one in the atrium and one in the ventricle.
- **Biventricular Pacemaker** has three wires, one in the right atrium, one in the right ventricle and a third one in the left ventricle. These pacemakers take more time to implant and can be used to improve pumping in patients with heart failure.

Today, pacemakers are **Rate Responsive** meaning they adjust the stimulation rate to a patient's level of activity. They pace faster when a patient is exercising and slower when a patient is resting.

Artificial pacemakers are used to take over the heart's own natural pacemaker. When the heart rate become too fast or too irregular, another type of implantable device called **Implantable Cardioverter Defibrillator (ICD)** can be used.

### 1.3.3. Implantable Cardioverter Defibrillator

In case of ventricular fibrillation, the ventricles do not have the time to be fully filled with blood at each heartbeat, inducing a sudden drop in blood pressure and a stop of the blood circulation within the circulatory system, leading to death in some cases. To prevent this event, internal defibrillation or shock can be the best way to avoid sudden cardiac arrest<sup>12</sup>. Implantable cardioverter defibrillators (ICDs) are used to detect dangerous fast heartbeats and give a lifesaving shock to correct the heart rhythm. Some severe cases of ventricular tachycardia and ventricular fibrillation are treated using ICDs.

Just as the APs, they are made of leads implanted in the myocardium with the opposite end of the lead connected to a generator. They are implanted in the same way as APs and the battery lifespan lasts from 5 to 8 years and the battery must be replaced when running out. Nowadays, almost all ICDs also act as pacemakers and can prevent slow heart rate.

---

<sup>11</sup> <https://www.hrsonline.org/pacemaker>

<sup>12</sup> <https://www.hrsonline.org/implantable-cardioverter-defibrillator>

## 1.4. Foreign body response and biocompatibility<sup>13</sup>

As for all medical implanted devices, the question of **biocompatibility** arises, especially when the implanted material must last for long periods of time. The word biocompatibility appears to be mentioned for the first time in 1970 in a chemistry peer-reviewed journal, the equivalent of the *Journal of Macromolecular Science*, but it took almost two decades before it began to be commonly used in the scientific literature.

The first definition of biocompatibility was given in the Williams Dictionary of Biomaterials (1999) as the “ability of a material to perform with an appropriate host response in a specific situation” and it was defined in the European Society for Biomaterials Consensus Conference. This definition is very general and can be clarified depending of the context.

In our case, we are particularly interested in the biocompatibility of long-term implanted devices as a cardiac pacemaker is implanted for 10 years on average. As explained by Morais *et al.* [28], biocompatibility consists basically of two elements: (a) biosafety, i.e., appropriate **host response** not only systemic but also local (the surrounding tissue), the absence of cytotoxicity, mutagenesis, and/or carcinogenesis, and (b) biofunctionality, i.e., the ability of material to perform the specific task for which it is intended.

The “host response” is governed by a series of mechanisms known as “Foreign Body Response” that will be explained in detail in the following chapter. Implanted devices induce an immediate and sustained inflammatory response until the material becomes encapsulated in a dense layer of fibrotic connective tissue, which isolates it from the surrounding tissues. This phenomenon is called **fibrosis**.

In the case of implanted pacemakers, fibrous encapsulation has two types of consequences:

- **Electrical consequence:** the electrical stimulation threshold increases.

Fibrosis of the myocardial tissue-electrode interface is cited as an important problem, which increases the stimulation threshold and adversely affects any sensing/feedback function. Despite the revolution in steroid-eluting leads, fibrosis remains a current challenge and will become even more important in the recent miniaturized leadless pacemakers.

- **Medical consequence:** tissue attachments make lead extraction a risky procedure for the patient.

By decreasing the mortality of the concerned patients, the devices last longer and are thus exposed to more problems<sup>14</sup>. Some complications such as obstruction of the access veins, leads fracture and, rarer but more serious, chronic or acute infections, require the removal of the leads. Fibrotic attachments that develop between chronically implanted pacemaker leads and the venous, valvular and cardiac structures are the major obstacles

---

<sup>13</sup> <https://www.sciencedirect.com/topics/materials-science/biocompatibility>

<sup>14</sup> From Philippe Ritter talk, at the 18<sup>th</sup> international congress CARDIOSTIM, 13-16 June 2012, Nice, France.

to safe and consistent lead extraction. Note finally that the more recent devices for resynchronisation therapy include a higher number of electrodes for stimulating or sensing and this will only exacerbate the problems.

Even if the inflammatory reaction is minimized during the implantation, especially thanks to the steroid eluting leads [25], which reduce the inflammation during the weeks following the surgery, the mechanism of fibrosis is still an area of research. As cardiac implants are long-term implanted devices, fibrosis remains an issue for the 5 to 10 years of implantation, even for the most recent leadless devices [26], [27]. These last types of device have not yet been implanted for more than 5 years, but even after one year of implantation, fibrosis develops around the pacemaker as we can see in Figure 1-10. A method for a systematic characterisation of this implant-induced fibrosis is lacking; this is a real obstacle to the development of clinically applicable diagnostic, preventive and therapeutic measures.

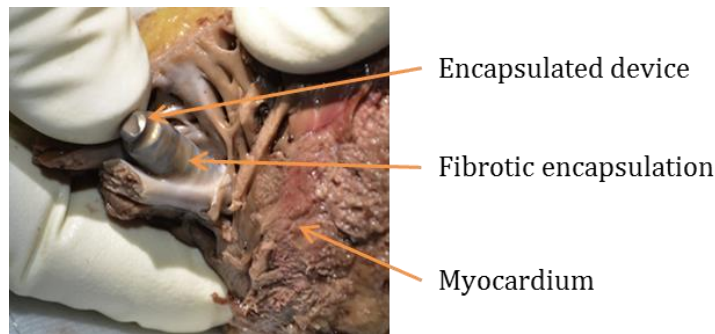


Figure 1-10: Fibrotic encapsulation of the Micra Leadless Pacemaker, image extracted and arranged from Kypta *et al.*

## 1.5. Objective and methodology of this PhD

In the context of cardiac active implants, this PhD focuses on fibrosis development at the electrode-myocardium interface.

As a patient is already equipped with cardiac leads connected to a stimulation device which can record the cardiac electrical activity, the main idea of this work is to investigate the use of an electrical measurement characterizing the fibrotic lead encapsulation and using this characterization method embedded in the stimulation circuit of the device. This would allow us to perform a non-invasive monitoring of the biocompatibility of cardiac leads and try to find new technical solutions to improve it. This brings us to the main question of our project: does the fibrosis developing around the cardiac leads have an electrical signature?

The characterization technique used is the Electrical Impedance Measurement (EIS), technique used for several decades for the characterization of biological tissues and which consists in sending a sinusoidal electrical current  $I$  and then measuring the resulting voltage  $U$ ; the impedance  $Z$  is the  $U/I$  ratio. Impedance spectroscopy is a measurement made over several frequencies, spread over a given interval. Depending on the frequency of the measurement signal, we can explore the tissue at different scales. At low

frequencies, the current will pass between the cells, the cell membrane appearing as an insulator. The higher the frequency of the signal, the more the applied current will be allowed to flow through the cell membrane. Thus, at low frequencies, we will have extracellular information, by increasing the frequency of the signal we access to intracellular information.

Fibrosis has several mechanisms, from cell to tissue scale. Cardiac Fibroblasts (CFs) compose about 50% of the cardiac cell population, alongside cardiomyocytes and other structural cells. Under a mechanical stress, they are activated and they differentiate into another cellular type, myofibroblasts. This phenomenon also causes a local overproduction of extracellular matrix of which collagen is an essential component. Myofibroblasts, which do not have the same morphology or function as fibroblasts, coupled with overproduction of collagen, will locally modify the active heart tissue.

## 1.6. Outline of the manuscript

My thesis work is organized along three axes. Two experimental approaches are conducted at cellular and tissue levels, using *in vitro* or *ex vivo* models. In addition, the feasibility of embedded impedance measurement *in vivo* is also discussed. The manuscript is divided into four chapters.

Chapter 2 presents a state of the art on this multidisciplinary topic, addressing cardiac fibrosis, its mechanisms when induced by an implant, impedance spectroscopy and its applications, and finally modeling of impedance measurements in this field.

Chapter 3 presents the *ex vivo* work. These experiments are carried out at the IHU LIRYC laboratory, on porcine or ovine cardiac tissue (ventricles mainly), with stimulation electrodes used on patients. Cardiac ventricles are maintained *ex vivo* at 4 ° C in a cardioplegic solution, saturated in potassium leading to heartbeat inhibition. The spectrum of electrode-tissue impedance is measured from 0.1 Hz to 1 MHz, in two distinct regions of the ventricle: a "normal" region and a region containing a high proportion of collagen, close to the mitral/tricuspid valve. The impedance spectra are analyzed using a known electrical model from which characteristic parameters of the two tissue types are extracted. After statistical analysis, these parameters are found to be significantly different allowing us to distinguish both tissue types.

Chapter 4 develops the *in vitro* part, presenting the electrical and biological characterization protocols, the results and their interpretation. Human cardiac fibroblasts cultures have been developed in wells with interdigital electrodes. Their differentiation into myofibroblasts can be spontaneous or accelerated using a growth factor. These cultures are characterized electrically and biologically over time. Electrical impedance measurements are performed with the xCelligence RTCA-DP device which provides unique cellular index (Cell Index) containing information about cell viability, proliferation and morphology; we also perform EIS over a frequency range from 1 Hz to 1 MHz, using the impedancemeter Solartron 1260. In parallel, an immunocytochemical characterization allows a visual control of cells proliferation and differentiation. After a

statistical analysis, the cell index shows a significantly different signature for cultures with and without growth factor.

Chapter 5 plans the chronic use of *in vivo* impedance spectroscopy. On one hand, the integration of an algorithm adapted to this measurement in the implanted stimulation devices will be discussed, on the other hand *in vivo* preliminary measurements on sheeps equipped with stimulators for several months are performed. For the first part, two methods were tested: one based on a standard multi-sinus excitation signal, using a neurostimulator developed in a previous thesis at the IMS laboratory, and the other based on the OFDM technique (Orthogonal Frequency Division Multiple) developed by our collaborators from the ETIS laboratory. Both methods respect the constraint of a fast broadband measurement, for periods of time much shorter than the cardiac rhythm.

## 1.7. A collaborative project

This PhD work results from an historical collaboration between several laboratories having different fields of expertise. My work was co-supervised by the IMS laboratory and the LIRYC institute, giving me the possibility to perform biological experiments easily as well as being in contact with experts in both impedance measurements and medical considerations. The ETIS laboratory is a long-term partner of the Bioelectronics group at IMS laboratory and has a strong experience on circuit design and embedded measurements. Along the time, this work was supported by CNRS MITI<sup>15</sup> thanks to many projects (FibroSES in 2013-2015 Defisens program, ICARE in 2018 PEPS program and currently SMARSTIM consortium).

IMS Laboratoire de l'Intégration du Matériau au Système	Bordeaux University CNRS UMR 5218	Bioelectronics	Cell cultures, immunocytochemistry, impedance measurements
IHU LIRYC L'Institut de RYthmologie et Modélisation Cardiaque	Bordeaux University Bordeaux University Hospital INSERM U 1045	Cardiac electrophysiology	Animal models, <i>ex vivo</i> and <i>in vivo</i>
ETIS Equipes Traitement de l'Information et Systèmes	Cergy-Pontoise University CNRS UMR 8051	Signal processing, embedded signal	Embedded impedance measurement, modelling

<sup>15</sup> Mission pour les Initiatives Transverses et Interdisciplinaires (Transversal and Interdisciplinary Initiatives Mission)



## CHAPTER II

# STATE OF THE ART

After introducing the societal context and the objectives of this PhD thesis (Chapter I), this chapter aims to draw up the state of knowledge on the cardiac fibrosis development and the state of the art of impedance spectroscopy measurements applied to the biomedical field, especially in cardiology. We will begin with the description of the cellular actors involved in the fibrosis mechanism, the **Cardiac Fibroblast** (CF) and the **MyoFibroblast** (MF). Then we will discuss in detail the development of fibrosis induced by cardiac lead implantation. Finally, an overview of the **Electrical Impedance Spectroscopy (EIS)** used as a characterization technique in the medical field will also be proposed as well as its theoretical background.

## 2.1. Cardiac fibrosis and implants

### 2.1.1. The Cardiac Fibroblast

In this work, we only focus on the CF characteristics and properties. Even though the cardiomyocytes are essential cardiac cells for the heart's electromechanical function, they do not play a major role in the fibrosis development.

#### 2.1.1.1. Generalities

Fibroblasts are cells present in most tissues of the body (except brain and blood for example), with different morphologies and functions depending on their location. In the heart, fibroblasts form the **largest cell population** [29], as shown in the 1980's with the studies of Zak and Nag in the adult rat left ventricle [1], [2]. Other studies extended on the whole rat heart suggested that the heart consists of approximately 70% non-myocyte cells and 30% cardiac myocytes [29], [30].

CFs appear during the embryonic development [31] and they play a **major role** in the cardiac formation defining the cardiac structure and function, and in remodelling as well [30]. They are arranged in sheets and appear as flattened elongated cells which lie along the cardiac myocytes within the collagen network. In Figure 2-1, CFs are stained in green, the cardiomyocytes are stained in red; we can see that the CFs are present in the interstices between the myocytes.

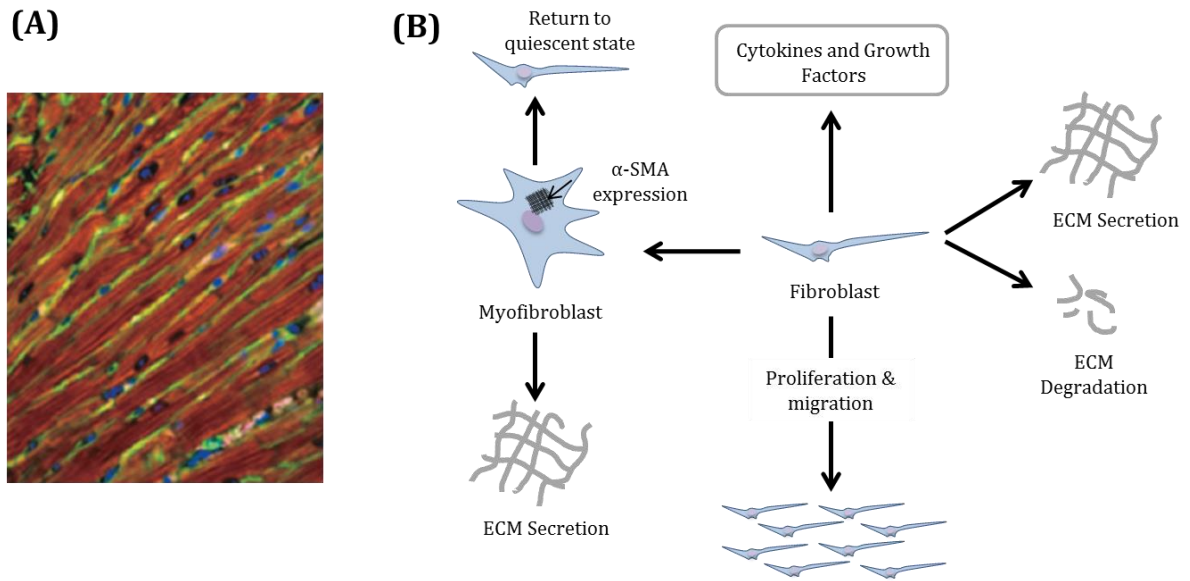


Figure 2-1: (A) from Souders et al, Circulation Research, 2009, Confocal micrograph of adult rat heart stained with phalloidin (red), DAPI (blue), and wheat germ agglutinin (green); (B) Role of cardiac fibroblast (redrawn from Souders et al, 2009)

#### 2.1.1.2. Function

Although the main primary function of CFs is the **synthesis and degradation** of the extracellular matrix (ECM) (Figure 2-1.B), providing structure to the heart, CFs also serve as “**sentinel**” cells that sense changes in their microenvironment (chemical, mechanical, structural and electrical signals) and respond to these changes in an appropriate manner [29], [32], [33].

CFs secrete all ECM constituents including the structural proteins and adhesion proteins generating a connective network (Figure 2-1.B) [34]. This physiological function allows fibroblasts to provide a scaffold for other cardiac cell populations [35]. The rigidity of the cardiac network is mainly insured by collagen type I and fibronectin [36]. On the other hand, they are also responsible for matrix degradation through production of degrading enzyme such as Matrix MetalloProteinases (MMPs) as well as their inhibitors, the Tissue Inhibitors of MetalloProteinases (TIMPs) [36]. This phenomenon allows to maintain the **cardiac homeostasis** [37].

Depending on the type of stimulus, CFs produce and secrete **growth factors, cytokines** and other **signalling molecules** that can regulate the function of nearby cells via autocrine/paracrine<sup>16</sup> signalling networks [29], [31], [38]. CFs also stimulate **angiogenesis**, i.e. the formation of capillaries from existing blood vessels [31] through the secretion of growth factors, contributing to maintain appropriate cardiac vascularization. They regulate the **cardiomyocytes proliferation** during embryonic development and in the adult heart through paracrine signalling [39].

<sup>16</sup> Autocrine signalling is a cell hormone secretion that binds to receptors of the same cell. Paracrine signalling is a cell hormone secretion that binds to neighbouring cells.

CFs can act as sensors and can respond to **mechanical stimuli** by proliferating and releasing growth factors and ECM proteins [40], [41]. They are also sensitive to **chemical signalling** such as pro- or anti-inflammatory stimuli or pro-fibrotic stimuli such as **Transforming Growth Factor- $\beta$**  (TGF- $\beta$ ), by secreting cytokines, and growth factors which can act in a paracrine or autocrine manner [41].

CFs are not electrically excitable but they are able to passively conduct a current if externally stimulated and have been shown to form functional gap junctions with cardiac myocytes [37] [42]. They promote the **synchronization of the contraction** between individual myocytes [43]–[45].

When the cardiac lead is implanted, it induces first a mechanical stress and then a chemical stimulus leading to the differentiation of fibroblasts into the myofibroblasts phenotype [37].

### 2.1.2. The Myofibroblast

The distinction between CFs and myofibroblasts is commonly based on the expression of contractile proteins such as  **$\alpha$ -Smooth Muscle Actin** ( $\alpha$ -SMA) [31], [39], [46].

Following cardiac injury, inflammatory cells and macrophages (cells from the immune system) migrate into the tissue via the vascular system. Upon arrival, they begin to secrete large amounts of both **TGF- $\beta$**  and Interleukin 1 beta **IL-1 $\beta$**  (cytokine produced by macrophages). Receptors for both of these cytokines are present on fibroblasts membranes [37]. The expression of various pro-inflammatory cytokines and pro-fibrotic factors lead to an increased proliferation of CFs [35] and to their differentiation to the **myofibroblasts (MFs) phenotype** [47] by increasing the transcription of the gene encoding the smooth muscle actin [37].

MFs are not part of a healthy cardiac tissue. In a pathological state or after a cardiac injury, one of the consequences is the ECM degradation by MMPs expression, increased activity, and a cell migration to the injured region. Myofibroblasts are more **mobile** than fibroblasts and can contract collagen fibres making them important for the **wound closure** [29]. These functionally and fully developed myofibroblasts generate high amounts of contractile force due to the presence of  $\alpha$ -SMA in **stress fibres**. Expression of  $\alpha$ -SMA is most widely used to identify myofibroblasts and considered as a key distinctive feature that differentiates fibroblasts from myofibroblasts [48]. As fibroblasts, myofibroblasts secrete a number of cytokines helping maintaining the inflammatory response to the injury [37].

### 2.1.3. Foreign body response to cardiac implants

Implanting an external device inside the heart inevitably brings out the question of body defence mechanisms. Even if the lead does not elicit a violent rejection from the heart, certain body reaction is to be expected, therefore the key aspect towards chronic

implantation resides in the pacemaker lead's ability to be well-accepted by cardiac tissues. Because the human heart has negligible regenerative capacity, cardiac injury poses a great challenge for its structural integrity, with the ultimate formation of a scar. The wound healing process is composed of three phases that temporally overlap [28], [49]–[51] represented in Figure 2-2. The Foreign Body Response (FBR) begins with the **necrosis** and **apoptosis** of damaged cardiomyocytes due to the cardiac device implantation. First the **inflammatory response** takes place, responsible for the clearance of dead cells and matrix debris from the damaged region [46], [52], [53], followed by the **proliferative phase** induced by fibroblasts migration to the damaged area and their activation into the myofibroblast phenotype secreting ECM proteins and collagen [46]; it is followed by the **maturation phase** which finally leads to fibrosis [46], [54].

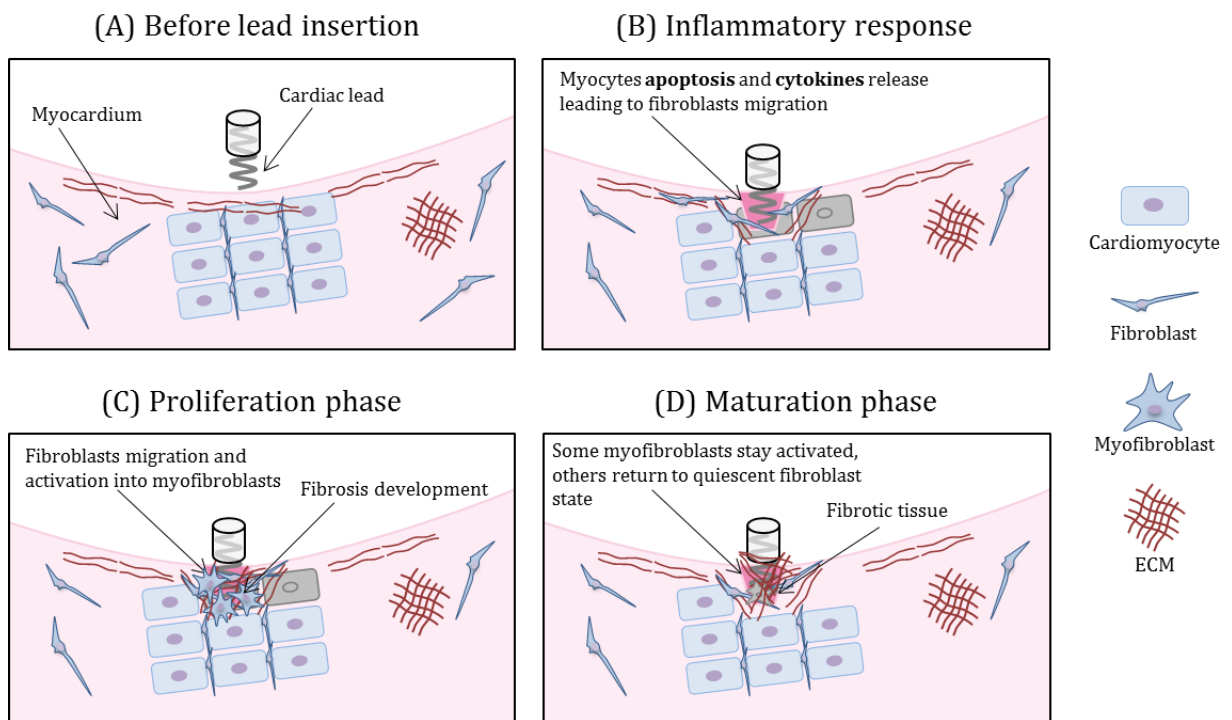


Figure 2-2: Schematic representation of the FBR after cardiac lead implantation into the myocardium (A) before the implantation, the myocardium contains mainly cardiomyocytes, fibroblasts and ECM components; (B) inflammatory response consisting in myocytes apoptosis and cytokines release; (C) proliferative phase with fibroblasts migration and activation into myofibroblasts; (D) maturation phase leading to tissue remodelling.

### 2.1.3.1. The inflammatory response

The first phase of the FBR process is the **inflammatory phase**. In the very first hours to days after the device is implanted (D1-D3), an intense inflammatory reaction is induced, characterized by neighbouring **cardiomyocytes apoptosis** and the diffusion of small molecules called **cytokines** (Figure 2-2.B). The local damages in capillaries will trigger the formation of blood clot made of proteins such as fibrin or **fibronectin**. These molecules locally interfere with the nearby environment by inducing a fibroblasts' proliferation and activation phenomenon.

### 2.1.3.2. The proliferative phase

The second phase or **proliferative phase** consists in the proliferation of cells with repairing capabilities called **myofibroblasts** which are **activated CFs** (Figure 2-2.C). With an increased stress and changes in the ECM metabolism, the release and regulation of cytokines and growth factors by fibroblasts in response to this altered mechanical stretch are observed. An increased production of a particular growth factor, the TGF- $\beta$  [37], is measured. Receptors of TGF- $\beta$  are present on fibroblasts membrane leading to their activation and differentiation into myofibroblast phenotype. The proliferation of myofibroblasts is hence strongly related to the production of extracellular matrix that can be indirectly emphasized by visualization of dedicated proteins: fibronectin and collagenous fibers which form the premature scar tissue. Myofibroblasts express a specific protein called  $\alpha$ -Smooth Muscle Actin ( $\alpha$ -SMA) giving them contractile properties [49]. The proliferative phase ends with the formation of collagen-based scar.

### 2.1.3.3. The maturation phase

The chronic reaction is considered as the sustained response of the tissue and consists mainly in the **maturation phase**. In the natural healing phenomenon, the myofibroblasts have different evolution possibilities, some slowly **vanish** (programmed cellular death), some return to their **quiescent state** [55] once the inflammatory phenomenon stops, and the rest of them stay activated. This last phenomenon enables a progressive **remodelling** of the fibrotic tissue, where the presence of activated cells is maintained over a longer duration implying a continuous **accumulation of ECM**.

Figure 2-3 represents the three phases of wound healing in the case of skin wounds. The last phase tends to be attenuated until the complete healing. This phase has a variable duration in time depending of the nature on the wound. In case of cardiac fibrosis, the maturation phase can last longer (few years) due maintained reaction of the body to the

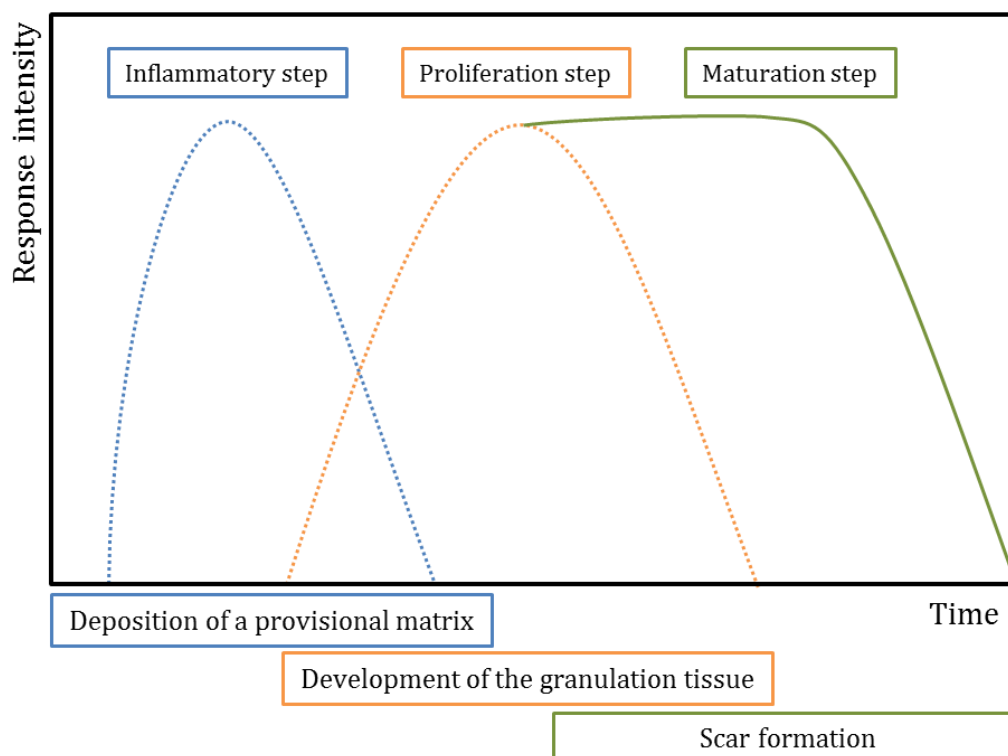


Figure 2-3: The three phases of wound healing process for the skin (redrawn from Darby et al)

lead. Indeed, the fibrotic capsule will first develop around the implantation spot and grow along the lead over the years [56].

## 2.1.4. Fibrosis

A definition of fibrosis has been given by Wolfram *et al* [51] in a review :

*“Fibrosis (from Latin fiber = filament, thread) is defined as an excessive deposition of collagenous and noncollagenous ECM components in organs or tissue as a consequence of proliferation and activation of fibroblasts”.*

It can arise in different parts of the body and involves both the innate and adaptive immune systems. In our work, we are particularly interested in the fibrosis arising from a foreign body implantation. Two types of implants exist:

- Active implants as cochlear implants [57], cardiac pacemakers or Brain Computer Interfaces (BCI);
- Passive implants as stents or subcutaneous implants for diabetes treatment [58].

BCI are a special case because the support tissue of central nervous system consists of glial cells, so the reaction is called gliosis, which is a real challenge for such implants [59]–[61]. For other type of implants, the inflammatory reaction induces fibrosis development.

In few cases, fibrosis can be advantageous like for unwanted foreign objects such as bullet fragment; the fibrotic tissue will act as an insulator avoiding the body contamination by compounds as lead [58].

During the cardiac lead implantation process, cardiac fibrosis modifies locally the cardiac tissue in a radical way. As said in 2.1.3.3, the **fibrotic tissue** is mainly composed of ECM components, and is **stiffer** than a normal cardiac tissue. The lack of some proteins (elastin [49]) and the presence or surplus of modified proteins (collagen type III [49], [62], collagen type I and fibronectin [36]) contribute to the local modification of the tissue. The fibrotic tissue encapsulates the lead so that it can no longer be “seen” by the body. In the case of a chemically stable and not corrupted material, the thickness of the capsule can stabilize after a phase of growth. Nowadays, most of the cardiac leads’ distal electrodes are steroid-eluting [25] that aims to reduce the inflammatory response and the fibrosis development locally; although this technique remains still sub-optimal as the fibrotic tissue grows along the lead.

This local tissue remodelling is such that it should be possible to characterize it and monitor its evolution *in situ* using electrical impedance spectroscopy (EIS), a physical technique already used to evaluate the electrical properties of biological matter, as we will discuss in the next part.

## 2.2. Electrical Impedance Spectroscopy

Biological tissues and liquids, like muscles, bones, blood, etc., possess electrical conductive properties, allowing them to carry electrical currents to varying degrees. These properties reflect their physical, biological and geometrical properties, and are essential for diagnostic approaches based on electrical measurements. The objective of our work is to measure and characterise these properties and their physical links in the case of cardiac fibrosis. We will firstly summarize the physical phenomena implied and characteristic parameters, then introduce the electrical impedance, its modelling and measuring techniques. A short review of application fields will also be presented to provide an idea of the wide scope of the use of this characterization method.

### 2.2.1. Electrical properties of biological tissues

#### 2.2.1.1. *Electrolytes and ionic conductivity*

Ions, proteins and other substances dissolved into a solvent (water for biological tissues) constitute an **electrolyte**. An electrolyte is a solution or a substance with **ionic DC conductivity** [15] (movements of ions), unlike classical conductors as metals which have an electronic conductivity (movements of electrons). Ion current is more complex than the electron current because it induces **chemical reactions, matter transport** and is also influenced by distribution of **polar molecules**. In a quiescent electrolytic solution, ions with an opposite sign will be attracted to each other. **Polar molecules** have a global charge equal to zero, but the distribution of their elementary charges is not centred meaning that they have a part which will be attracted by negative charges and a part attracted by positive charges.

The substances contained in an electrolyte can be transported in 3 different ways: (1) **migration** results from an applied electric field, (2) **diffusion** arises in case of concentration gradients and (3) **convection** is a macroscopic movement of the entire solution. The latter will not be considered, having no place in our applications.

- **Migration**

When an electric field is applied to an electrolyte (via metallic electrodes), it induces charge movement leading to ionic conductivity.

The **conductivity**  $\sigma$  (S/m) was defined by Kohlraush [63] as the separate contributions of the anions (-) and the cations (+). The **current density**  $\vec{j}$  (A/m<sup>2</sup>) of a single anion-cation pair is

$$\vec{j} = (nze\vec{v})_- + (nze\vec{v})_+ = Fcy(\mu_- + \mu_+) \vec{E} \quad (1)$$

where n is the number of ions per volume, z is the valency of an atom (number of electrons available for transfer), e is the charge of an electron (C), v is the velocity of the ion (m/s),

F is the Faraday constant (C/mol), c is the ionic concentration (mol/m<sup>3</sup>),  $\gamma$  is the activity coefficient (generally the value of  $\gamma$  is between 0 and 1 depending on the ion couple),  $\mu$  is the ion mobility (m<sup>2</sup>/Vs), and  $\vec{E}$  is the electric field (V/m). The current density must be summed up with contributions from each negative and positive ion species.

This relation can also be expressed as a function of the conductivity and the electric field and is equivalent to the Ohm's law for volume conductors:

$$\begin{aligned} \vec{j} &= \sigma \vec{E} \\ \sigma &= Fc\gamma(\mu_- + \mu_+) \end{aligned} \quad (2)$$

It is also possible to define the total contribution of the different ionic species to the total conductivity of the volume V (m<sup>3</sup>) of the quiescent solution (without an externally applied electric field) as:

$$V \sum (nze)_- + V \sum (nze)_+ = 0 \quad (3)$$

We can see with the equation (3) that, for a quiescent solution, there is an **electroneutrality**.

Another approach consists in the description of the total contribution using the **molar conductivity**  $\Lambda$  (Sm<sup>2</sup>/mol) which is expressed in terms of the ions' concentration:

$$\Lambda = \frac{\sigma}{c} = \gamma F (\mu_- + \mu_+) \quad (4)$$

The molar conductivity is a parameter directly linked with the mobility and not with the concentration. The unit is (S/m) per (mol/m<sup>3</sup>) or (Sm<sup>2</sup>/mol). We can then define the global conductivity as the sum of the ionic molar conductivities:

$$\sigma = \sum_{i=0}^n c_i \Lambda_i \quad (5)$$

The Table 2-1 [15] gives the molar conductivities in mS.m<sup>2</sup>/mol for the most present ions in biological tissues.

Table 2-1: Molar conductivities (mS.m<sup>2</sup>/mol) of the main ions in biological tissues

Cations	$\Lambda_0$	Anions	$\Lambda_0$
H <sup>+</sup> /H <sub>3</sub> O <sup>+</sup>	34,98	OH <sup>-</sup>	19,86
Na <sup>+</sup>	5,01	Cl <sup>-</sup>	7,63
K <sup>+</sup>	7,35	HCO <sub>3</sub> <sup>-</sup>	4,45
Ca <sub>2</sub> <sup>+</sup>	11,90	CO <sub>3</sub> <sup>-</sup>	13,86

These different equations can be applied only for solutions with low concentration of the ionic species. Ion mobility cannot be considered as a constant for high concentration due to the ions' interactions: ions tend to form a pair of opposite charge to minimize the mobility.

The conductivity of a solution is also influenced by the temperature at which the measurement is performed. Electrolyte conductivity varies of about 2% per degree. The higher the temperature, the lower is the solvent viscosity, increasing the collisions between the ions of the electrolyte. The pressure is also a parameter that can influence the conductivity of an electrolyte but in our case, all the experiments are performed at atmospheric pressure. Biological tissues have ionic conductivities that depend mostly on the nature and quantity of ionic content and mobility [64]–[66].

- **Diffusion**

Molecular diffusion is described by Fick's laws. Consider a simple system in the form of a compartment with unity width and height dimensions and a concentration gradient in the infinite length  $x$  direction. Fick's first law is

$$M = -D \frac{\partial c}{\partial x} \quad (6)$$

where  $M$  is the molar flux density in  $\text{mol}/(\text{s}\cdot\text{m}^2)$  and  $D$  the diffusion coefficient in  $\text{m}^2/\text{s}$ . the minus sign indicates that the transport is toward lower concentration. During stationary diffusion (e.g., in a tube), the Equation 7 shows that a linear concentration will be set up in the diffusion zone out from the electrode surface. Fick's second law is

$$\left(\frac{\partial c}{\partial t}\right) x = D \frac{\partial^2 c}{\partial x^2} \quad (7)$$

### 2.2.1.2. Dielectric properties of a medium

- **Definition**

A **dielectric** is often associated to a volume of insulating material placed between the plates of a capacitor for examination by an applied electric field [15]. Etymologically, a dielectric is a material that the electric field penetrates (Greek *dia* means through). The dielectric properties characterize how this volume allows the "penetration" of the electric field.

Living tissues are **wet biomaterials** and therefore considered as electrolytic conductors with ions free to migrate inducing DC conductivity. However, the environment in which ions move influences the total ion current. Dielectricity is frequency-dependent, providing to the material the ability to store energy capacitively or to dissipate it. If the conductivity  $\sigma$  is the characteristic parameter for pure conductors, the permittivity  $\varepsilon$  is used to characterize the "capacitive" or insulating aptitude of a material. Biological tissues may be regarded either as conductors or dielectrics and finally complex notation accounts for both.

- **Electrostatic forces**

Successive historical developments have been made concerning the dielectric theories of biomaterials. The eldest one, in the XVIII<sup>th</sup> century, was based on the relationship between two static electric charges and the mechanical force between them. **Coulomb's law** used a new physical constant  $\epsilon_0$ , the vacuum permittivity (in F/m), that appears in the expression of the force between two charges  $q_1$  and  $q_2$  at a distance of  $L$ :

$$\vec{F} = \frac{q_1 q_2 \vec{L}}{4\pi L^3 \epsilon_0} \quad (8)$$

If the medium of this interaction is not the vacuum, the permittivity  $\epsilon$  becomes specific to this medium. An often used constant  $\epsilon_r$ , the relative permittivity, is dimensionless, so that  $\epsilon = \epsilon_0 \epsilon_r$ . Let us notice that the electric field concept itself derives from Coulomb's law.

- **Polarization of a dielectric**

The second main development came in the XIX<sup>th</sup> century, with Maxwell equations that describe how an electromagnetic field behaves in a medium.

Another physical phenomenon characteristic of dielectrics is polarization. Polarization in a biomaterial is the electric field-induced disturbance of the charge distribution in that volume [15]. Polarization was already evoked previously about the polar molecules present in an electrolyte, water molecules mainly. The H<sub>2</sub>O molecule has a **permanent dipole moment** due to non-uniform distributions of positive and negative charges on the various atoms. At a macroscopic scale, a material composed of molecules, polar or not, can be described by its **polarization P** (C/m<sup>2</sup>), which is the dipole moment per unit volume. The polarization of a material can be described with the following equation:

$$\vec{P} = (\epsilon_r - 1)\epsilon_0 \vec{E} = \chi_r \epsilon_0 \vec{E} \quad (9)$$

Where  $\chi_r = \epsilon_r - 1$  is the electric susceptibility and dimensionless, it indicates the degree of polarization of a dielectric in response to an applied electric field. "The permittivity is a measure of the amount of dipole moment density created or induced by an electric field" [15].

Equation 9 emphasises the proportionality relation between the polarization and the electric field. We can then say that without an applied electric field, the polarization of the material is equal to zero. When an electric field is applied, different types of polarization can appear at the atomic, molecular and macroscopic scales.

**Electronic polarization:** under an applied electric field the electronic cloud (negative charge) will move with respect to the nucleus (positive charge). Electrons displacement is very fast (picoseconds) and the dispersion is in the gigahertz region. This phenomenon is represented in Figure 2-4.A for a random atom.

**Ionic polarization:** positive and negative ions composing the molecules will go in opposite direction under an applied electric field. This leads to a displacement of the barycentre of the positive and negative charges inducing a polarity into the molecules

initially apolar and an increased polarity for the molecules already polar. This phenomenon is illustrated in Figure 2-4.B and is slower than the electronic polarization (tens to hundreds of picoseconds).

**Orientalional polarization:** polar molecules form permanent dipoles organized randomly and are influenced by an applied electric field leading to an organization in their orientation. This phenomenon is represented in Figure 2-4.C and is slower than the two previous polarizations (nanoseconds). In polar materials, rotational movements will be caused by the torque experienced by permanent dipoles in electric fields.

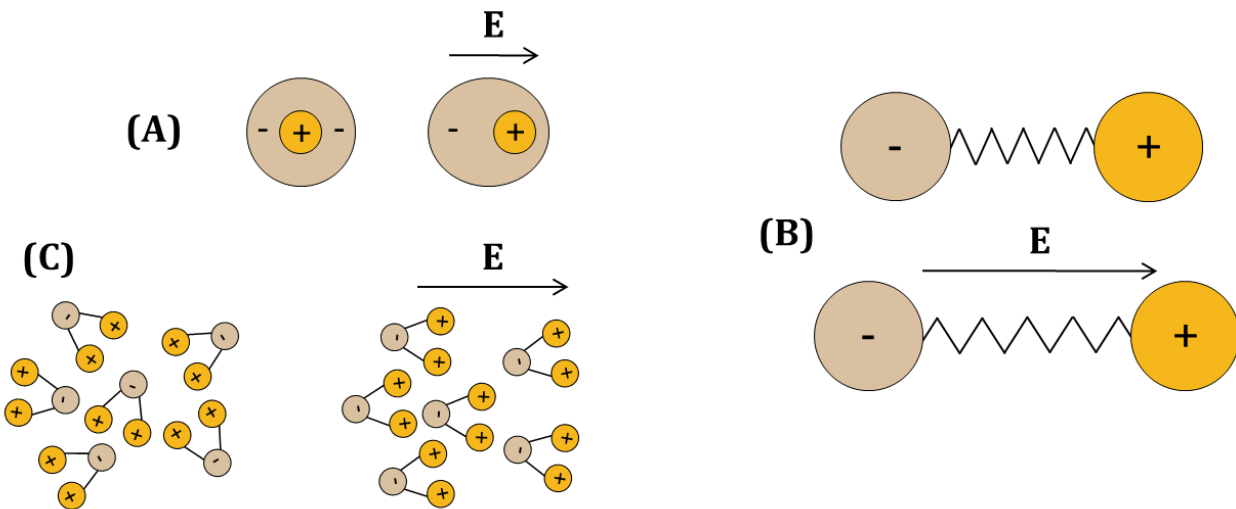


Figure 2-4: Schematic representation of the different type of polarizations induced by an applied electric field, (A) Electronic polarization, (B) Ionic polarization and (C) Orientalional polarization

- **The capacitor model**

Polarization cannot itself be measured but linked to the capacitance of a capacitor build with a volume of dielectric material between two plates. Applying a DC voltage between the plates does not create a DC current. Applying an AC sinusoidal voltage leads to an AC sinusoidal current in quadrature (90° phase shift); it is not a current of electrons passing the plates through the dielectric but a current of electrons charging or discharging the plates. The **capacitance** (F) of such a capacitor depends of the area A (m<sup>2</sup>) and distance d (m) between the plates:

$$C = \epsilon \frac{A}{d} \tag{10}$$

- **Complex variables**

On one hand, in electrolytes, ions free to migrate induce a DC conductivity  $\sigma$ . On the other hand, in dielectrics there is no DC conductance but polarization disturbs the distribution of positive and negative charges, a phenomenon characterized by the permittivity  $\epsilon$ . When an electric field is applied, this leads either to an in-phase current ( $\sigma$ ) or a quadrature current ( $\epsilon$ ). When a material has both properties, it becomes interesting to use the complex variables, able to take into account these two components. Such a material, when

enclosed between two plates or “electrodes”, will be characterized by a **complex admittance**  $\underline{Y}$  defining the current in this “capacitor” with respect to the voltage:

$$\underline{Y} = \frac{A}{d} (\underline{\sigma} + j\omega\underline{\epsilon}) \quad (11)$$

- ***Relaxation and dispersion***

As the last mainstream of this brief history of Physics, appeared in the XX<sup>th</sup> century, the Debye tradition considers biomolecules as polar materials with exponential relaxation.

In an electric field of time varying strength and direction, polarization and charge displacements do not occur instantaneously in the material. Depending on the measuring frequency, charge could not have enough time to adjust their position: at low frequencies, the material polarization is maximal but with an increasing frequency, polarization and permittivity will decrease. This time dependence allows us to introduce the concept of **relaxation**. Debye, in the XX<sup>th</sup> century, used the relaxation concept to describe the time required for dipolar molecules to orient themselves. The relaxation refers to the transient phase that leads the material to a new equilibrium, after the application of a step of E-field strength. The relaxation time is the characteristic parameter. Dispersion is the correspondent frequency domain concept of relaxation.

## 2.2.2. Dispersion in biological tissues

Schwan emphasized the concept of dispersion in the field of dielectric spectroscopic analysis of biomaterials. Dispersion means frequency dependence according to relaxation theory. Biological materials rarely show a single time constant Debye response. Knowing how complex and heterogeneous living tissue is, the concept of a distribution of time constants should not be a surprise, as well as the distribution is also often non-symmetrical. All such models are covered by the dispersion concept.

A biological sample as the heart muscle is a complex combination of concentrated cells with interconnections. Its electrical properties like every biological tissue are frequency dependent and its dielectric parameter reaches enormous values at low frequencies [67]. When impedance measurements are made over a larger frequency range (from Hz to GHz), different mechanisms are observed and reflect the various compartments of the biological tissue under test. These include the cell membrane properties, the biological macromolecules and fluids compartments inside and outside the membrane.

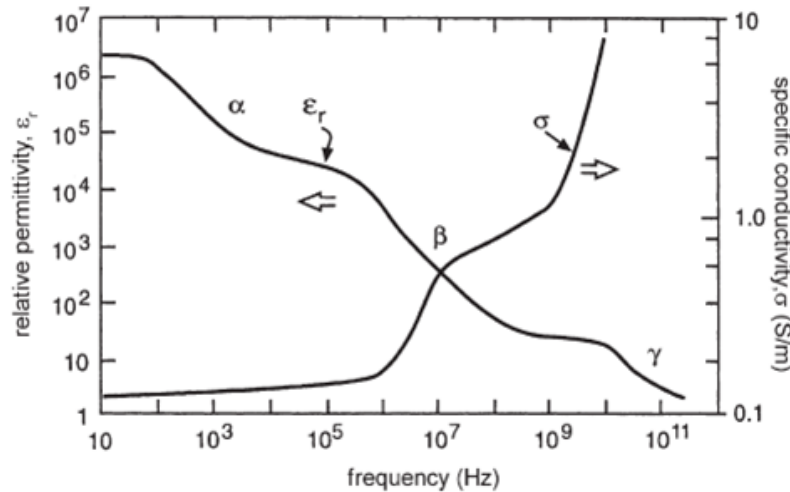


Figure 2-5: Permittivity and conductivity spectra of a biological sample

Global electrical properties of a biological sample can be illustrated in a diagram representing the complex permittivity and conductivity containing different dispersion zones. Three different dispersions are generally identified: **alpha**, **beta**, and **gamma**, which are defined for well-known physical properties [64], [68], [69]. Each dispersion represents the predominance of each effect. For the conductivity representation, the resistive effect of the extracellular medium is predominant at low frequencies and it is replaced by the conductive effect of the intracellular medium with increasing frequencies. For the permittivity representation, the capacitive effects of the membranes happen first until the frequencies are so high that we only measure the permittivity of the water of the sample. A general diagram of the dispersion zones is represented in Figure 2-5 [15], [67].

- **Alpha dispersion** is found from few hertz to few kilohertz, a multitude of mechanisms contribute to this dispersion [70]. It is mainly due to the ionic diffusion phenomenon occurring at the membrane surfaces; and mainly present in denser tissue like muscles. As it occurs at low frequencies it is often hidden by the electrode-electrolyte interface phenomenon (explained in 2.2.4.2).
- **Beta dispersion** occurs in the range 0,1-10 MHz. Its mechanism was first analysed by H. Fricke and K.S. Cole [71]. It is caused by the polarization of cell membranes which act as barriers to ionic flow. It takes time to charge the membranes through the conducting phases in- and outside the cell membranes. It goes with a significant increase in conductivity and decrease in permittivity.
- **Gamma dispersion** occurs in the highest frequency range (few GHz). At this stage, the cell membranes become hidden and the sample just appears as a simple electrolyte. This dispersion is associated with water molecules relaxation [68], [72].

In 1929, Debye showed that a non-interacting population of dipoles experienced an exponential relaxation response, equivalent to a complex permittivity  $\underline{\varepsilon}$  of first order power of  $(j\omega)$ :

$$\underline{\varepsilon} = \varepsilon_{\infty} + \frac{\varepsilon_s - \varepsilon_{\infty}}{1 + j\omega\tau_0} \quad (12)$$

In Equation 12,  $\varepsilon_s$  is the static value of  $\underline{\varepsilon}$ , it represents the low frequency permittivity where polarization is maximal;  $\varepsilon_{\infty}$  is the high frequency permittivity at which polarizable entities are unable to respond [73].

Further findings showed that a description by a **fractional power law relaxation** was more generally experienced by dielectrics. In 1941 [74], Cole arranged the equation of complex permittivity proposed by Debye, introducing a new component, the **Constant Phase Element** (CPE) which will be developed later in this chapter (paragraph 2.2.4.2).

$$\underline{\varepsilon} = \varepsilon_{\infty} + \frac{\varepsilon_s - \varepsilon_{\infty}}{1 + (j\omega\tau_0)^{1-\alpha}} \quad (13)$$

The Cole-Cole representation consists in plotting the real part of the permittivity against the negative of the imaginary part of it on a Wessel diagram, each point being characteristic of one frequency of measurement. In the Cole-Cole representation (Figure 2-6.A), both the axis need to be with the same scale to not distort the curve. The disadvantage of this method is that we lose the frequency dimension of the data

The Bode representation (Figure 2-6.B) consists in plotting the magnitude and the phase of the impedance as function of frequency in two different plots. This representation is convenient because it shows the complete impedance spectrum.

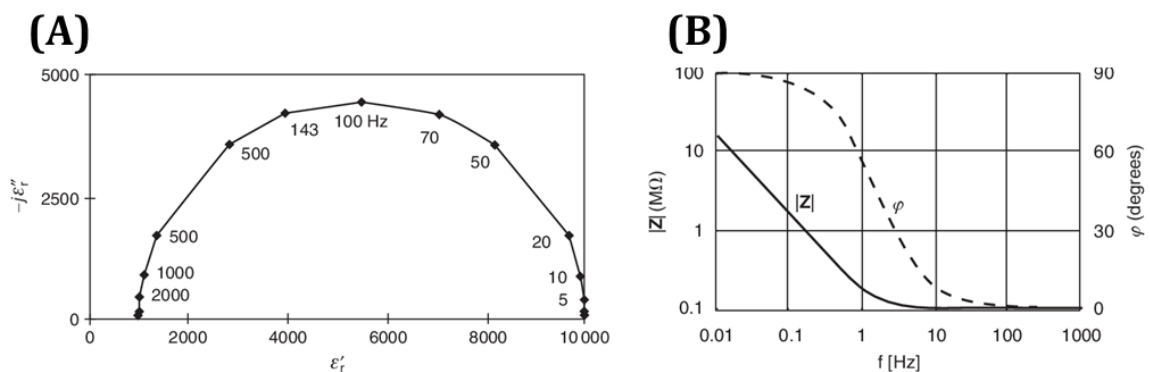


Figure 2-6: (A) relative permittivity in the Cole-Cole representation plotted on a Wessel diagram; (B) Bode representation of the impedance of a RC series circuit (taken from Martinsen *et al*)

### 2.2.3. Electrical impedance of biological tissue

Electrical Impedance Spectroscopy (EIS) is a measurement technique used for the study and characterization of biological systems. This type of measurement can be challenging to interpret but gives much information on the composition of the tissue such as the nature of ionic species in solution, the cellular state; and on the nature of the electrode such as the surface condition and the porosity. Such information varies depending on the frequency range of the applied signal and the tissue temperature. Impedance measurement is used also for characterizing the electrochemical properties of batteries, fuel cell (see part 2.2.6).

The impedance measures the opposition of a system to an applied physical variable. The term comes from the verb “to impede” which means to delay or stop the progress of something<sup>17</sup>. In our case we are interested by the electrical impedance that consists of the measurement of the system’s opposition to the displacement of electric charges with an applied electric field.

The impedance of the system can be calculated using the Ohm’s law:

$$\underline{Z}_e = \frac{\underline{U}}{\underline{I}} \quad (14)$$

where  $\underline{Z}_e$ ,  $\underline{U}$  and  $\underline{I}$  are respectively the complex impedance, voltage and current. It is then possible to introduce the complex representation of the impedance:

$$\underline{Z}_e = \frac{U_0}{I_0} e^{j\varphi} = \frac{U_0}{I_0} (\cos \varphi + j \sin \varphi) \quad (15)$$
$$\underline{Z}_e = R + jX$$

$U_0$  and  $I_0$  represent respectively the modules of  $\underline{U}$  and  $\underline{I}$  and  $\varphi$  represents the phase shift between  $\underline{U}$  and  $\underline{I}$ .  $R$  is the resistance (real part) of the system and  $X$  the reactance (imaginary part). The reactance of a system gives us important information about the system behaviour: if it is positive, the system is inductive; negative the system is capacitive and if it is equal to zero the system is purely resistive.

As said in the precedent part, the impedance of the biological system is frequency dependent and when an electric field is applied to a biological system via two electrodes (basic capacitor experiment [15]) as represented in Figure 2-7, a current will form a movement of ions in the aqueous medium. This can be expressed in terms of tissue conductivity and permittivity. At higher frequencies, membranes let the current go through as shown in Figure 2-7.

---

<sup>17</sup> <https://www.oxfordlearnersdictionaries.com/definition/english/impede?q=impede+>

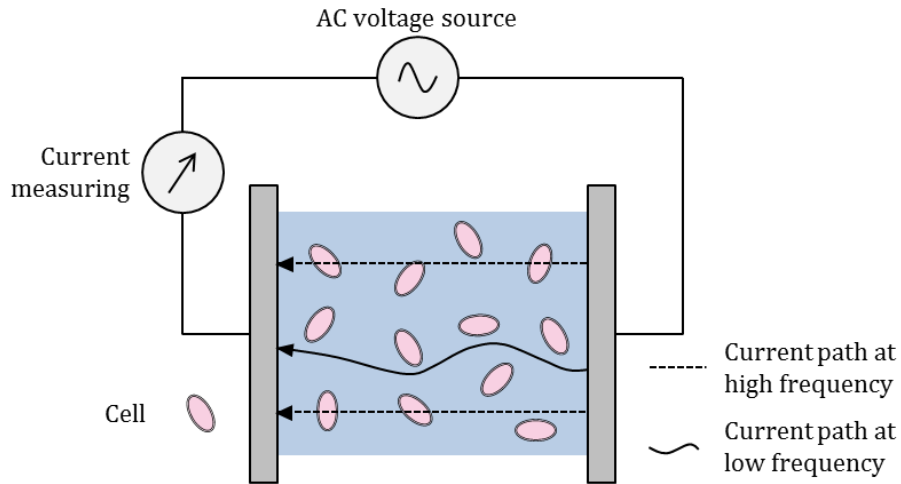


Figure 2-7: Schematic representation of basic capacitor experiment with the current flow in biological tissue at low and high frequencies (redrawn from Martinsen *et al*)

The conduction of electric currents through tissue is strongly dependent on frequency. Furthermore, the relationship between impedance, conductivity and permittivity depends on electrode geometry as explained in the paragraph 2.2.1.2 with Equation 10 and Equation 11. This allows us to express the complex impedance  $\underline{Z}$ , equal to the reciprocal of the complex admittance:

$$\underline{Z}(\omega) = \frac{1}{\underline{Y}(\omega)} \quad (16)$$

With the Equation 16, we deduce that the impedance is inversely proportional to the complex electrical permittivity and conductivity, and proportional to a constant that depends on the electrode geometry (Equation 11). For experimental measurements of frequency dependency of biological tissues, impedance spectroscopy can be used consisting in applying a weak oscillating voltage/current and measuring respectively the resulting current/voltage. Impedance can be fitted with analytical formulas derived from circuit models. Impedance spectroscopy is a validated characterization technique in different medical fields for diagnosis and monitoring purposes.

In 1957, Schwan *et al* [75] have conducted the first study to analyse the frequency-dependent specific resistance of *in situ* living dog tissues and observed different dispersions. By the end of the 1990's, a survey [68] and an extensive database [64] of measurements at different frequencies were published by Gabriel *et al*. The database investigated the dielectric properties of permittivity and conductivity for different human and animal tissues at body temperature for a frequency range from 10 Hz to 20 GHz, using impedance analysers. The human analysed tissues were brain (grey matter), heart muscle, kidney, liver, lung, spleen, muscle (across and along the fibres), uterus, skin, thyroid, testis, ovary and bladder. They concluded that the measurements were in accordance with the values in the literature and that for measurements at low frequencies (below 1 kHz), the electrode polarization phenomenon (explained later in paragraph 2.2.4.2) affected the results.

## 2.2.4. Equivalent electrical models

### 2.2.4.1. Equivalent model for the tissue

- **Fricke's model**

Biological tissues feature two electrically conducting compartments: the extracellular and intracellular spaces, separated by the cellular membrane. This membrane is mainly composed of amphiphilic phospholipids, meaning that they have a hydrophilic head and a hydrophobic tail (Figure 1-2). As the extracellular and intracellular mediums are mainly composed of water, the heads are naturally oriented to the water and the tails tend to form the most stable structure possible. The membrane is a lipid double layer permeable to ionic species or molecules [76]. It possesses capacitive properties due to its small thickness. The classic model that exists to represent the extra-intracellular medium is the Fricke model [77], [78]. It is represented in Figure 2-8.A, with the schematic representation of a cell.

This type of electrical circuit can be modelled using the following equation:

$$Z = R_e \frac{1 + pR_i C_m}{1 + j\omega(R_i + R_e)C_m} \quad (17)$$

where the different elements are the same as in the Figure 2-8.A.

- **Cole model and Constant Phase Element (CPE)**

Unfortunately, the ideal capacitive behaviour contained in  $C_m$  is rarely observed. Instead, in a Nyquist diagram (or Wessel diagram), we generally find “depressed” semi-circular arcs whose centres lie below the real axis and whose high and low frequency intercepts with the real axis are at angles  $\phi \neq 90^\circ$ . Cole (1940) proposed the now much used empirical equation, described with the equivalent electrical circuit shown in Figure 2-8.B describing such “depressed” tissue impedance loci:

$$Z = R_\infty + \frac{R_0 - R_\infty}{1 + (j\omega\tau)^\alpha} \quad (18)$$

$\tau$  is a time constant equal to  $1/2\pi f_c$  and  $\alpha$  is a fractional power dependency related to the depression angle such that  $\phi = \alpha\pi/2$ ,  $\alpha$  is a constant such that  $0 < \alpha < 1$ . A simple interpretation of the above equation is in terms of a circuit where a resistance  $R_\infty$  is in series with the parallel combination of a resistance,  $\Delta R$  equal to  $(R_0 - R_\infty)$ , and a CPE, which resembles a capacitor, sometimes called “Constant Phase Angle” impedance,  $Z_{CPA}$ . In this case one is considering  $Z_{CPE}$  in terms of an impedance, where  $K$  as the measure of the magnitude of this impedance and has units of  $\Omega s^{-\alpha}$  [79], [80]. The  $Z_{CPE}$  can be derived from the Cole equation above and has the form described in the following equation:

$$Z_{CPE} = K(j\omega)^{-\alpha} \quad (19)$$

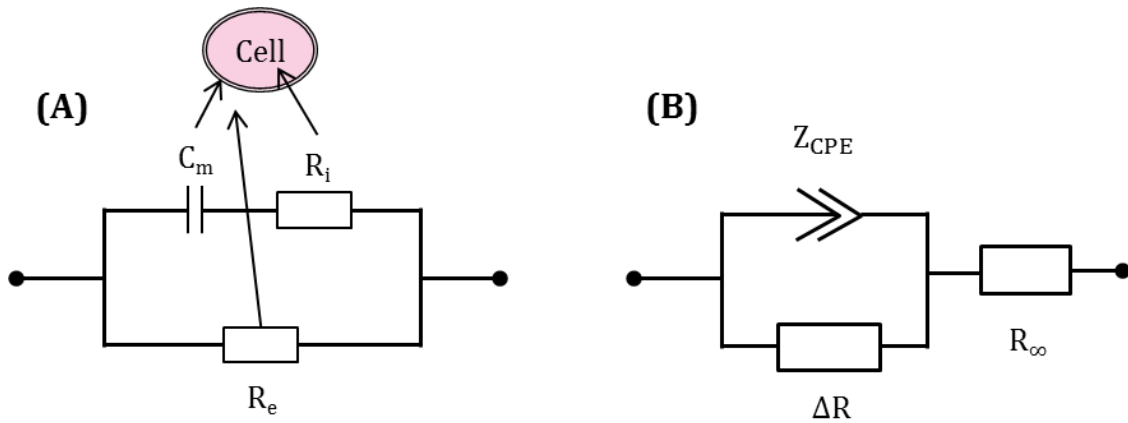


Figure 2-8: (A) Representation of the Fricke's equivalent circuit of a cell with  $C_m$  the surface capacitance,  $R_i$  the intracellular medium resistance and  $R_e$  the extracellular medium resistance; (B) Representation of the CPE model with  $R_\infty$  is the combination of the lead and medium's resistances,  $\Delta R$  is equivalent of  $R_\infty - R_0$  with  $R_0$  the charge transfer resistance

#### 2.2.4.2. Electrode-electrolyte interface

When an electric measurement is performed, it always disrupts the system under characterization. In case of biological systems, perturbations are observed at the electrode- electrolyte interface and we assist at a phenomenon called **electrode polarization** (not to confuse with the polarization of dielectrics developed earlier!). Since the earliest studies on electrical properties of biological tissues, electrode-electrolyte interface exhibited the properties of a capacitance [81].

The metal electrodes contain electrons as charge carriers and the physiological medium possesses ions as charge carriers. The fundamental physical process happening at the interface is the transduction of charge carriers from electrons in the metal electrodes to ions in the electrolyte, in other words, there are charge transfer mechanisms at the interface with non-faradaic (capacitive) charge transfer and faradaic reactions [82]. The non-faradaic charge transfer consists in a charge redistribution inducing a plane of charge at the surface of the metal electrode. Under the influence of the electric field, an excess of negative charges is driven at one of the interfaces, attracting cations in solution towards the electrode and repelling the anions. At the other electrode the opposite occurs. This phenomenon creates an **ionic double layer** [83] in the interfaces. The applied voltage drops rapidly in these layers, implying a huge electrical polarization of the material and a near-absence of the electric field in the bulk sample at low frequencies [84].

As shown in Figure 2-9, electronic charges accumulate in the electrode part; in the electrolyte part, the ionic double layer, also called the Helmholtz layer [84] is composed of: a first layer of water molecules which induces the stronger capacitive effects. This layer is very thin, usually less than  $10\text{\AA}$  (about the width of a water molecule). It is the Inner Helmholtz Plane (IHP); a second layer of solvated ions which is larger than the first layer, hundreds of  $\text{\AA}$  depending of the ionic species in solution. It is the Outer Helmholtz Plane (OHP).

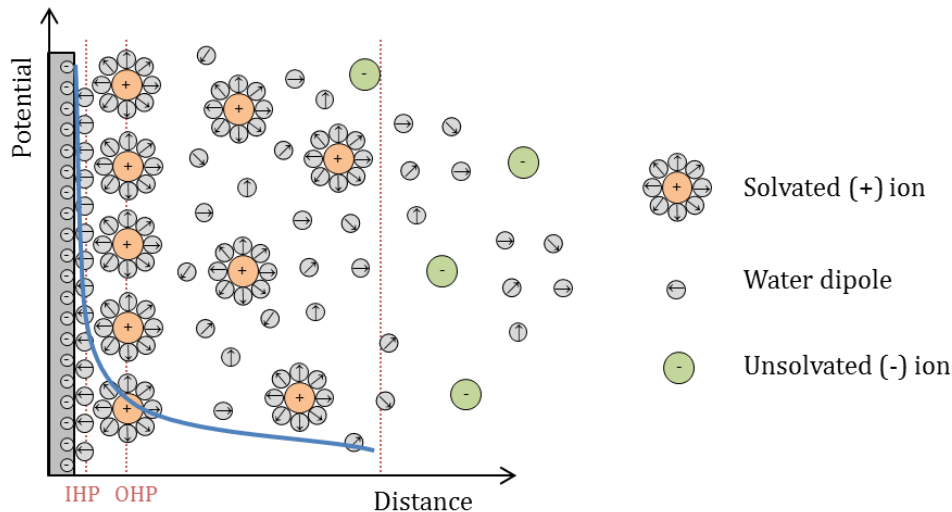


Figure 2-9: Schematic representation of the double layer capacitance at the electrode-electrolyte interface

- **Double Layer (DL) model**

The first model studied here considers the electrode-electrolyte interface as the contribution of a double layer capacitance  $C_{dl}$  and faradaic impedance [85], [86]. This model assumes that charge is redistributed parallel to the electrode surface ( $C_{dl}$ ) and that charge is injected from the electrode to the medium through Faradaic processes ( $Z_{Faradaic}$ ) of reduction/oxidation.

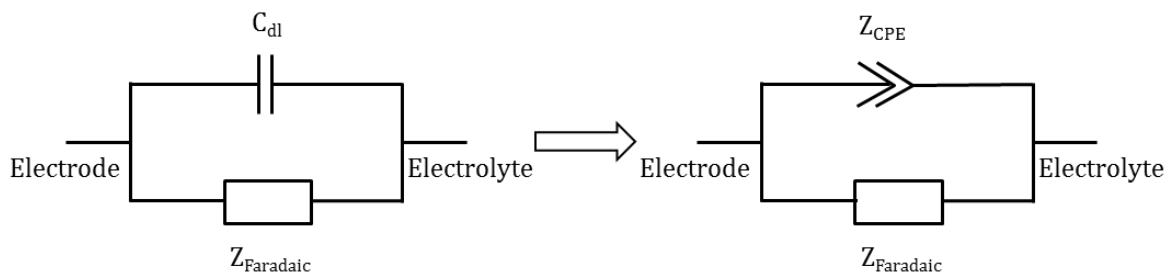


Figure 2-10: Electrical model of the double layer impedance

As for the equivalent model of the tissue itself, electrode-tissue interface impedance gives rise to depressed semi-circular arcs on complex impedance plots, leading to a  $Z_{CPE}$  that replaces simple capacitor  $C_{dl}$  in the above circuit, as represented in Figure 2-10.

The history of electrical equivalences for the physical, electrochemical and chemical processes happening in the electrode-electrolyte interface have been reviewed by MacDonald and Johnson [87]. This phenomenon can be corrected by adapting the measurement signal to the experimental set-up [88], by fitting or modelling in the treatment of the measurements or with some electrode coating [84].

### 2.2.4.3. Global equivalent model

When measuring the impedance of a tissue in contact with an electrode, both previous models come in series. The electrode-tissue interface impedance dominates at low

frequencies and that of the tissues dominates the high frequencies. One can also add a relatively small resistance due to the sum of the leads and connectors.

## 2.2.5. Impedance measurement

### 2.2.5.1. Measurement technique

Usually, an instrument that can be used to measure impedance at a given frequency is schematically represented in Figure 2-11, and consist of an **AC source**, together with a detector that can measure the magnitude and phase angle of the evoked potential at the given frequency. The AC source may be a controlled voltage or a controlled current, but in either case, the current magnitude and phase is measured internally in the instrument. The measured current and potential are the same variables presented in the paragraph 2.2.3. The instrument can then calculate the resulting impedance ( $Z$ ) by using Equation 14.

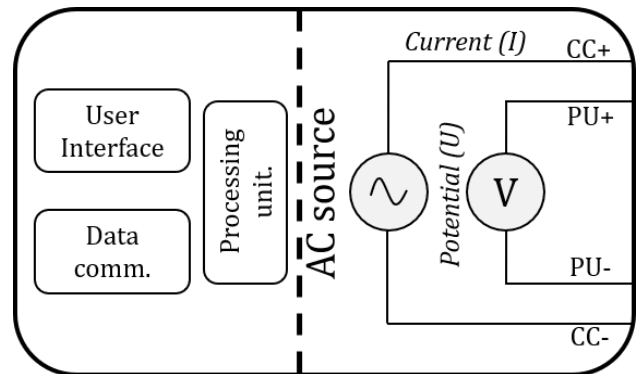


Figure 2-11: Schematic representation of a typical spectrometer using ohm's law to measure impedance. The instrument can have a user interface and/or a data communication unit in order to control the instrument and read out the impedance data.

In Figure 2-11, the two current-carrying (CC) connections are separated from the two used for voltage (or potential) pick-up (PU). This allows the instrument to be connected in several ways, which will be discussed later. The instrument may be programmed to measure one or more frequencies. If an instrument is set up to measure a sequence of frequencies, the result is called an **impedance spectrum**. Different measurement techniques exist to obtain this impedance spectrum. It is either possible to send a signal with a single frequency component at a time or with several frequency components at the same time.

- **Frequency domain**

This type of measurements consists in sending to the system a signal containing a single frequency component at a given time. This technique is called a **swept-sine signal**<sup>18</sup>. Its frequency increases or decreases over time and can be linearly or logarithmically distributed over time. Both examples of these excitation signals are represented in Figure 2-12<sup>18</sup>.

One of the big disadvantages of this measurement technique is that it takes time, depending on the minimal frequency of the signal and the number of periods for each frequency, the measurement can take more than few minutes. It makes this method not so well adapted for certain applications. This issue will be discussed in the last chapter of this thesis. That is why it is necessary to consider the possibility to measure all the

<sup>18</sup> [http://zone.ni.com/reference/en-XX/help/373398C-01/svaconcepts/lvac\\_frequency\\_sweep/](http://zone.ni.com/reference/en-XX/help/373398C-01/svaconcepts/lvac_frequency_sweep/)

frequencies of interest at the same time. We then speak of measurements made in the time domain.

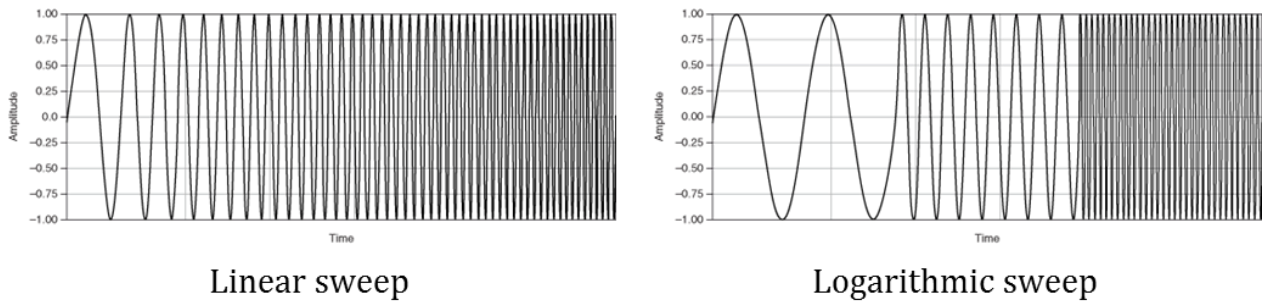


Figure 2-12: Linearly and logarithmically distributed swept-sine signals

For a part of our work, we will use this type of excitation because it allows obtaining the greatest amount of information in the frequency domain.

- **Time domain**

Using an excitation signal in time domain means that this signal contains multiple frequency information at the same time. We obtain a **broadband excitation**. “Broadband” refers to the energy distribution of a signal in the frequency domain. This energy is distributed on a frequency range. The interesting feature of this is that it is possible to do measurements on multiple frequencies simultaneously as opposed to the stepped sine approach. There are numbers of methods for generating a good broadband excitation signal represented in Figure 2-14 such as the sum of two or more sine waves called **multisine** [89], **chirp signals** where a continuous sine wave with time-dependent frequency is used [90], [91], or **binary (digital) signals** (Discrete Interval Binary Sequence)[92]. There are more types available, but the basic idea is the same: create a signal that has short duration with a frequency content that is high.

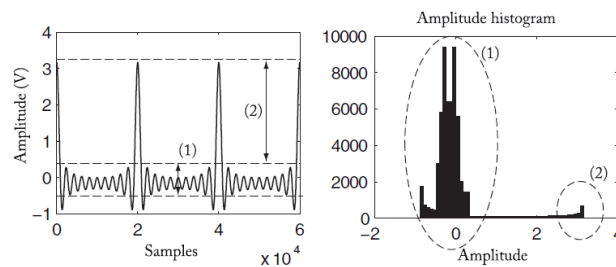


Figure 2-13: Example of a periodic signal with a poor CrF and its amplitude histogram (right). Most signal amplitude values are concentrated in a small y-axis amplitude range (1) compared to the signal overshoot (2), extracted from Sanchez *et al*, 2012

We have to consider two different criteria to generate an adapted broadband signal to our experiment conditions [93]. One temporal criterion: the **Crest Factor** (CrF) which represents the ratio between the maximal value and the effective value as shown in Figure 2-13. The lower is the CrF, the better will be its Signal to Noise Ratio (SNR) representing the level of a desired signal to the level of background noise.

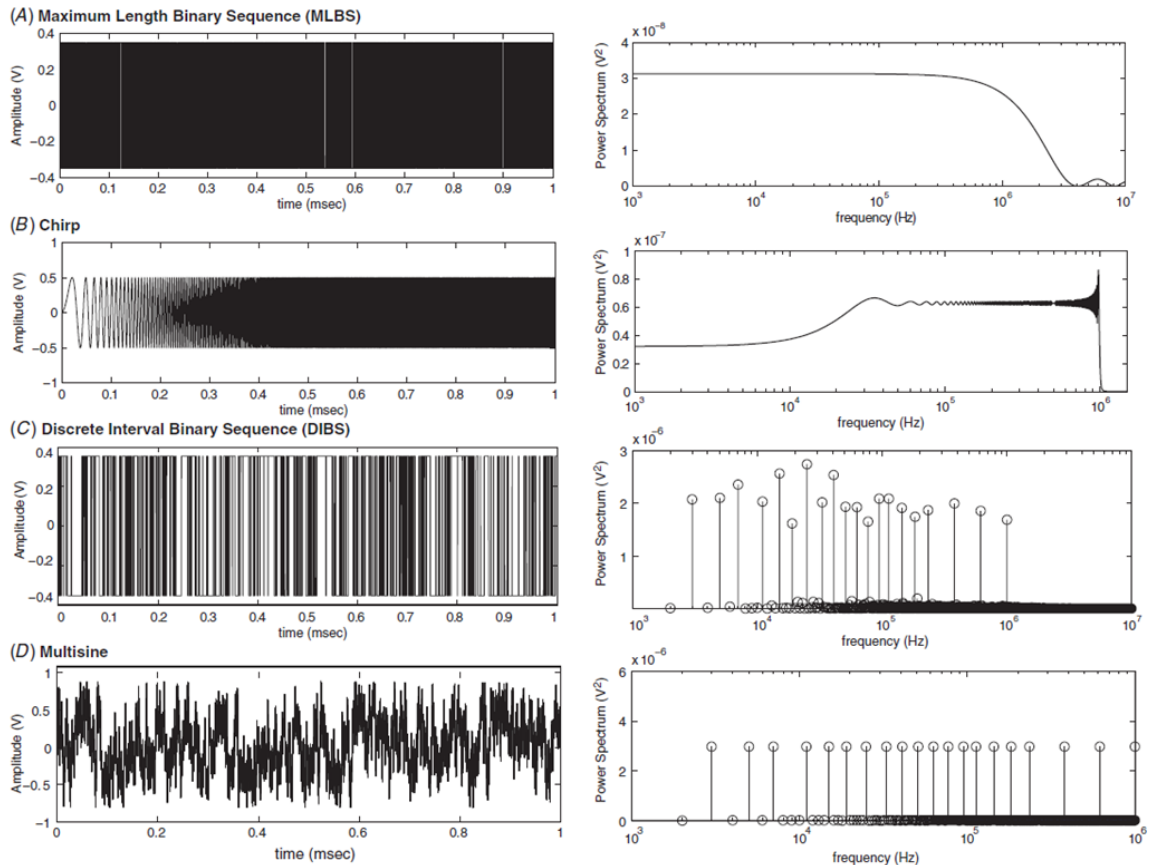


Figure 2-14: Representation of the different broadband excitation signals, extracted from Sanchez *et al*, 2012

The second criterion is a frequency criterion; we have to consider the distribution of the energy within the frequency spectrum. In order to maximize the energy in a broadband signal, it is necessary to generate a signal with an energy contained within the frequency range of interest. To optimize the energy distribution, two types of signals are possible: continuous spectrum signals and discrete spectrum signals. Sanchez *et al* [93] have conducted a comparative study on the different broadband signals:

Table 2-2: Overview table of the comparative study of the possible optimization of the broadband signals

Signal	MLBS	Chirp Pulse	DIBS	Multisine
Crest Factor	1	1,45	1	$> \sqrt{2}$
Spectrum nature	Continuous	Continuous	Discrete	Discrete
Temporal optimization	Optimized	No	Optimized	Yes
Frequency optimization	No	No	Yes	Yes

For a part of our work, we will be interested in the multisine excitation signal because it is the broadband signal with the better conditions that we can embed in a custom stimulation circuit.

- **Electrode configuration**

As explained previously, impedance measurement consists in sending an excitation signal driven in voltage or current and measuring the resulting voltage. This allows different electrode configurations as represented in Figure 2-15.

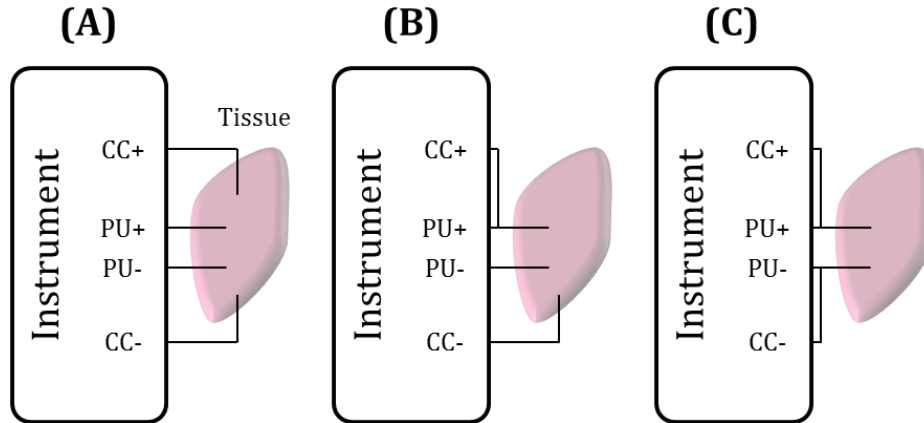


Figure 2-15: Schematic representation of the different electrode configurations for impedance measurements, (A) 4-electrode configuration; (B) 3-electrode configuration; and (C) 2-electrode configuration

The different configurations have properties that make them suitable for different tasks. The most basic is the **two-electrode configuration** shown in Figure 2-15.C. This configuration is simple, nevertheless it suffers from undesired electrode effects as the electrode polarization phenomenon described in the paragraph 2.2.4.2.

The **three-electrode configuration** shown in Figure 2-15.B is typically used to focus the sensitivity in a small volume.

Finally, there is the **four-electrode configuration** in Figure 2-15.A, this configuration allows to get rid of the electrode polarization phenomenon [84] but even this suffers non-ideal effects [94].

In our work, different measurement techniques will be used depending on the application. As we perform preliminary measurements for approving the use of EIS to characterize lead-induced cardiac fibrosis, we will use swept sine signals on cells and tissues to have full impedance spectra and enlighten frequency ranges of interest for the fibrosis detection. As we want to carry out a non-invasive measurement using cardiac leads already installed on a patient, the two-electrode technique will also be privileged for this project.

#### 2.2.5.2. Impedance analyzers

If an instrument is measuring a range of frequencies, either by using stepped sine or by using broadband excitation, the result is called an impedance spectrum, and the instrument is called an impedance spectrometer. Note that measuring the evoked potential at a given frequency may be challenging and may involve quite complex processing of signals in the analogue and/or digital domain. Furthermore, the extraction

of magnitude and phase information from a broadband evoked potential is a requiring a processing of a large amount of data.

For this work we are mainly interested with a robust analyser which enables us to obtain a databank of impedance spectra of the cardiac muscle in different configurations. Several analysers are compared in Annexe A.

We choose the Solartron 1260<sup>19</sup> which is the gold standard for impedance spectroscopy, allowing us to investigate the low frequencies.

## 2.2.6. Fields of application

Different bioelectrical impedance methods are already used for non-invasive health monitoring [95]. The different characterization techniques are

- **Bioelectrical Impedance Analysis (BIA)** [96], is a technique in which the body composition of a biological object is analysed by measuring its bioelectrical impedance [97], [98].
- **EIS** (see paragraph 2.2.3) [87] can be used as a non-destructive evaluation technique for a number of applications in the field of science engineering and technology such as electrochemistry and chemical engineering [99], [100], material engineering [101], biomedical engineering [73], [102], civil engineering [103], wood science [104], plant physiology [105], microfluidics [106], material engineering [107], fuel cell technology [108] and Mems and thin films [109]. This list of applications is non exhaustive [110] showing that EIS is a multi-application characterization technique.
- **Impedance Cardiography (IGC)** is a technique which calculates the changes in blood volume in transthoracic region over time in terms of the changes in transthoracic impedance [111], [112]. It gives several hemodynamic parameters (cardiac volume, stroke volume, left ventricular ejection time, heart rate and so on) and it is possible to have information about the heart health. It is a technique developed since the 1940's.
- **Electrical Impedance Tomography (EIT)** [113], a Computed Tomographic (CT) image reconstruction technique, is a non-linear inverse problem in which the electrical conductivity or resistivity of a conducting domain is reconstructed from the surface potentials developed by an injected current signal. EIT is low cost, portable, fast, non-invasive, and radiation-free technique finding many advantages compared to other computed tomographic methods as X-Ray CT, or Magnetic Resonance Imaging (MRI) [114], [115].

---

<sup>19</sup> <https://www.ameteksi.com/products/frequency-response-analyzers/1260a-impedance-analyzer>

EIS is found more popular in several fields of application compared to BIA and ICG as it provides the impedance variations over frequencies. Also, EIS has been studied for the non-invasive characterization of biological as well as non-biological materials in frequency domain whereas BIA and ICG are used in biological fields only, measuring at particular frequency. They are impedance analysing techniques which provide the impedance values of the tissue sample as a lumped estimation, whereas the bioelectrical EIS calculates and analyses the electrical impedance at different frequencies which enable us to obtain not only the impedance values of the tissue sample as an estimation at a suitable frequency (generally, 50kHz) but also it provides the information to understand several complex bioelectrical phenomena like dielectric relaxation and dielectric dispersions. EIT provides a spatial distribution (2D or 3D) of the impedance profile of a domain under test using a set of boundary voltage-current data. Therefore, EIT has the potential of visualizing the tissue physiology and pathology in terms of tomographic images of the electrical impedance distribution, and hence it has been applied in several medical applications.

## 2.3. Motivation for this work

Even if work has already been done in the combined fields of bioimpedance and cardiology, we think that this work can add more expertise in these fields.

From the bioimpedance side, we know that measured impedance is dependent on several factors such as tissue properties, electrodes geometry and configurations, and excitation signal. Focusing on the cardiac fibrosis, this is a phenomenon that modifies deeply the structure of the tissue compared to the normal cardiac tissue: this modification can show up in a bioimpedance measurement as diseased hearts will have tissue properties that diverge from those of a healthy heart [62], [116].

From the cardiology side, implant-induced cardiac fibrosis is clearly an unwanted complication to cardiac device implantation. Device encapsulation leads to an increase of the stimulation thresholds and thus decreases the battery lifespan, which are some of the deleterious consequences of the development of fibrotic tissue along the lead. These tissue attachments also make lead extraction a risky procedure for the patient.

From the scientific point of view, the mechanism of fibrosis is still an area of research and a method for a systematic characterisation of implant-induced fibrosis is lacking; this is a real obstacle to the development of clinically-applicable diagnostic, preventive and therapeutic measures. A better understanding of this tissue development could help developing anti-fibrotic drugs, myofibroblasts having the capacity to reverse to the fibroblast phenotype [117].

Finally, a characterisation method of the fibrosis that develops at the electrode-tissue interface, chronic and non-invasive as it could be embedded in the implanted circuitry, could not only serve to improve the long-term biocompatibility but also produce a new diagnosis tool helping the medical team to anticipate lead extraction surgery, if needed.

In this thesis, we propose a preliminary investigation of the feasibility of impedance measurements *in situ*, performed on different fibrosis models. We decided to explore two scales of biological models: the microscopic scale, with an *in vitro* model studying the

fibroblasts activation and differentiation; and a macroscopic scale, exploring the possibility to discriminate cardiac tissues of different natures with an *ex vivo* model. In this report, we will first present the *in vitro* model developed and its results of impedance and biological characterization. We will continue with the development of the *ex vivo* model and its resulting impedance spectra. Finally, we will introduce the possibility of performing embedded measurements for *in vivo* characterization.

## CHAPTER III

# ELECTRICAL IMPEDANCE SPECTROSCOPY EXPLORATION AT THE CARDIAC TISSUE LEVEL

This chapter develops the EIS experiments performed on cardiac tissues. We used a **simplified model of cardiac fibrosis *ex vivo***, characterizing cardiac tissues taken from animal hearts. The tissue we used, a ventricular wedge preparation, came from animals that were part of another experimental protocol. The goal was first to obtain a reference database of bioimpedance measurements of such tissues, using human pacing leads. Then we wanted to study the impedance differences between normal and altered tissue, searching for a tissue having some properties of fibrosis. With this model, we wanted to know whether EIS measurement allowed the **discrimination** of a healthy tissue from a “fibrotic” tissue. Thus, we performed measurements in **healthy tissue** regions on the endocardium and in regions with naturally occurring higher degrees of collagen expression near the insertion of the valves, which we termed the **collagenous tissue**.

Both types of tissue are characterized using the Solartron 1260 and a human cardiac lead. The Solartron 1260 allowed us to perform impedance spectroscopy over a wide frequency range. The characterization results were analysed with equivalent electrical models inspired from the literature. These models gave us biophysical parameters that we could analyse to determine the significance of the differences.

The chapter begins with the material and methods regarding the *ex vivo* model and its extraction procedure, then comes the description of the measurement bench, the measurement protocol, and the bench characterization. Then, we will present the results and their modelling, followed by their statistical analysis.

### 3.1. Material and Methods

Two animal models were developed for this work: porcine and ovine. In both cases, the hearts were explanted following a specific surgical protocol that will be described firstly, and then we will present the different cardiac leads that were used to characterize the tissues, as well as the measurement protocol and the statistical analysis methods.

#### 3.1.1. Animal model

This study was carried out in accordance with the recommendations of the Directive 2010/63/EU of the European Parliament on the protection of animals used for scientific purposes and approved by the local ethical committee of Bordeaux CEEA50.

The heart was obtained from the animal, premedicated with ketamine (20 mg/kg) and acepromazine (Calmivet, 1mL/50kg). Anaesthesia was induced with intravenous injection of sodium pentobarbital (10 mg/kg) and maintained under isoflurane, 2%, in 100% O<sub>2</sub>. The animal was euthanized by sodium pentobarbital (40 mL, from 50 mg/mL of stock) and the heart rapidly excised, cannulated by the aorta, and rinsed with cold cardioplegic solution, containing (mM): NaCl, 110; CaCl<sub>2</sub>, 1.2; KCl, 16; MgCl<sub>2</sub>, 16; NaHCO<sub>3</sub>, 10; and glucose, 9.01 at 4°C.

In case of porcine tissue, we used the left ventricles. The left ventricle (LV) wall was dissected and placed in the cardioplegic solution. It was conserved on ice for the whole duration of the experiment. The animals were young swine, Large White, 40±5 kg. In case of ovine tissue (female Charmoise, 40kg), we used the right ventricle (RV). The protocol of isolation of the tissue was the same than for the swine ventricle.

The part of the ventricle which is close to the tricuspid/mitral valve (for RV and LV respectively) is known to contain more structural collagen, giving a stiffer tissue. This type of tissue can be assimilated to a simplified fibrotic tissue. Indeed, collagen is one of the main components of the extracellular matrix which is abundantly produced in the fibrosis development. Both healthy and collagen tissues are pointed on the Figure 3-1, on a swine's left ventricle.

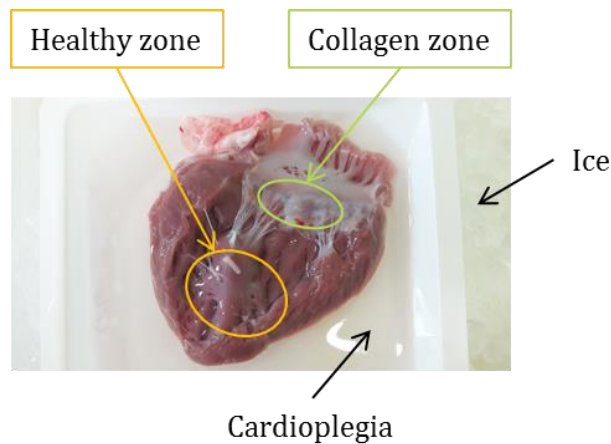


Figure 3-1: Localisation of the healthy zone in orange and the collagen zone in green on a swine left ventricle

Both right and left ventricular tissues were healthy and considered to be similar, although we must keep in mind that cardiac leads are usually implanted in the right ventricle.

In this document, we will present the results of the measurements performed on swine left ventricles, as it is the condition in which we have enough samples. For the other conditions, the number of samples is too low in order to analyse statistically the results.

### 3.1.2. Pacing leads

As said in the first chapter, depending on the arrhythmia, either a pacemaker or an implantable defibrillator will be implanted, with the corresponding lead. A lead can be **bipolar** or **quadripolar** meaning that it has respectively two or four electrodes dedicated

to the stimulation, the defibrillation or the sensing depending on the nature of the implant. For our work, we had different cardiac leads to perform the measurements.

The first type of leads were the bipolar leads. The model we had was the 5054 Capsure Z Novus from Medtronic, described as steroid-eluting, bipolar, implantable, tined, atrial, transvenous lead. It is J-shaped, as we can see on Figure 3-2.A, because it is implanted in the right atrium and its fixing system on the cardiac wall is anchor-shaped. On Figure 3-2.B the tip or proximal electrode, made in platinum and implanted in the atrium, is pointed in orange, and the electrode pointed in red is the ring or distal electrode, made of a polished platinum alloy<sup>20</sup>.

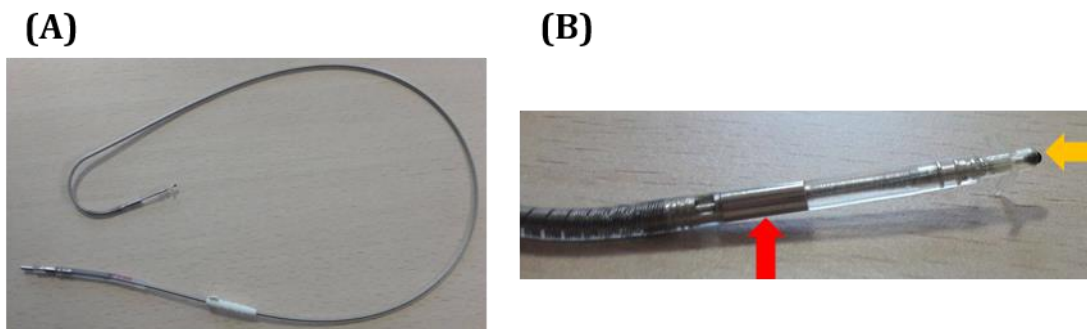


Figure 3-2: (A) 5554 Capsure Z Novus lead; (B) Zoom on the electrodes, the stimulation electrode pointed in orange and the counter electrode pointed in red

As a quadripolar lead, we had the 6947M SprintQuattro Secure, described as steroid-eluting, quadripolar, screw-in ventricular lead with RV/SVC (Superior Vena Cava) defibrillation coil electrodes and composed of four electrodes; 2 coil-electrodes for defibrillating pointed in green on Figure 3-3.A, and 2 electrodes for the pacing and sensing activities (in purple on Figure 3-3.A). The fixing system on the cardiac wall is a helix that is screwed in the ventricular endocardium. Both the proximal (in orange on Figure 3-3.B) and distal (in red on Figure 3-3.B) electrodes are made of platinized platinum alloy<sup>21</sup>.

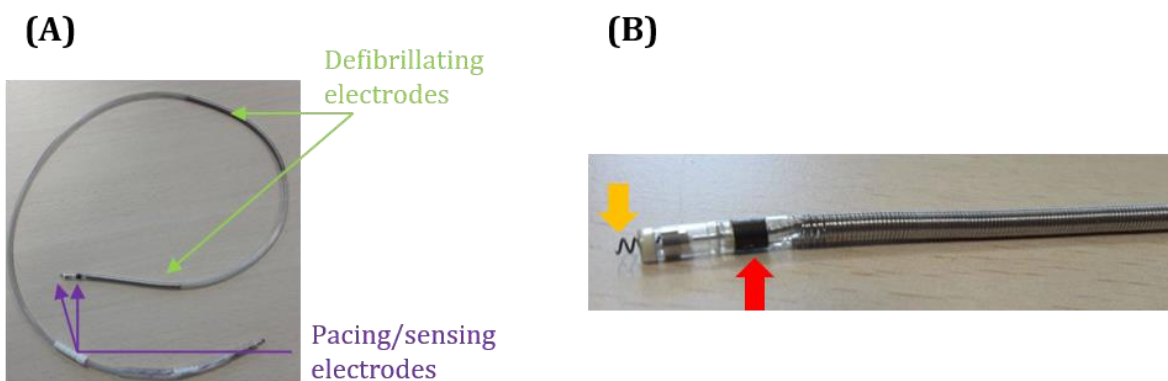


Figure 3-3: (A) 6947M SprintQuattro Secure lead; (B) Zoom on the pacing/sensing electrodes with the proximal electrode pointed in orange and the distal electrode pointed in red

EIS measurements were systematically performed with both leads but for the rest of this chapter, we will only present the results obtained with the SprintQuattro lead, even if the

<sup>20</sup> [http://manuals.medtronic.com/content/dam/emanuals/crdm/A03381001\\_CONT\\_20060222.pdf](http://manuals.medtronic.com/content/dam/emanuals/crdm/A03381001_CONT_20060222.pdf)

<sup>21</sup> [http://manuals.medtronic.com/content/dam/emanuals/crdm/CONTRIB\\_181143.pdf](http://manuals.medtronic.com/content/dam/emanuals/crdm/CONTRIB_181143.pdf)

characterization of both leads will be presented. The SprintQuattro lead enabled a better fixation in the cardiac tissue, especially for the stiffer collagenous tissue, making the use and fixation of an anchor-shaped lead more difficult on these *ex vivo* tissue preparations.

### 3.1.3. Measurement bench

#### 3.1.3.1. Measurement principle

The Solartron 1260A (Ametek, USA) is an impedance analyser considered as one of the most reliable lab instruments for impedance measurements, especially for bioimpedance measurements. With a frequency span from 10  $\mu$ Hz to 32 MHz, this analyser has a wide frequency range allowing to perform measurements at very low frequencies, with a high level of precision.

It performs a frequency sweep on the wanted frequency range and can be driven either by current or by voltage. The frontend of this instrument is quite simple, it has almost not evolved since the Solartron 1260 creation, but it can be controlled using different softwares. In our case we used the software ZPlot (Ametek, USA) to create the measuring signal and the software ZView (Ametek, USA) to plot the results. This last software enables to use different types of representation as Cole plots, or Bode plots. We chose the Bode representation to better highlight the role of frequency.

The Solartron was connected to an in-house fabricated connector, via coaxial cables. This connector has been designed to configure 2-electrode or 4-electrode measurement (paragraph 2.2.5.1) with manual switches. We connected the cardiac lead to the connector with crocodile clips. The measurement bench is schematically represented in Figure 3-4.

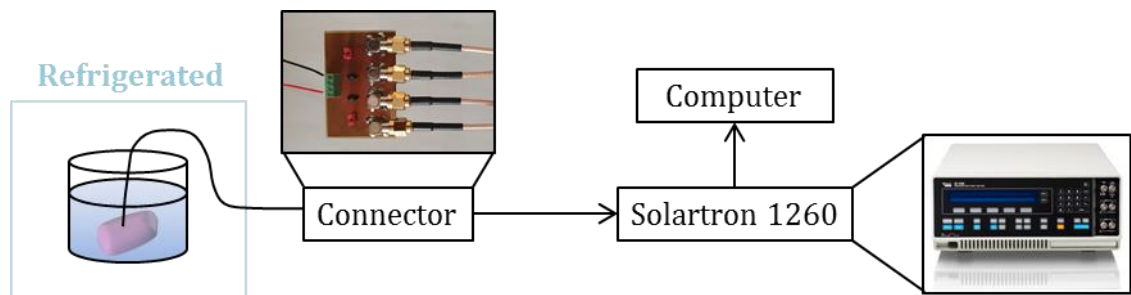


Figure 3-4: Schematic representation of the test bench for *ex vivo* measurements

For our work, we only performed 2-electrode measurements. Indeed, as we used commercial leads, 4-electrode measurements were not possible. 2-electrode impedance measurements were performed between the proximal and distal electrodes.

### 3.1.3.2. Measurement protocol

We performed tissue impedance measurements with the SprintQuattro lead, using the proximal and distal electrodes (Figure 3-3.B). The measuring signal was driven with a voltage level of 100 mV, covering the frequency range from 0,1 Hz to 1 MHz, and we used a logarithmic repartition of the frequencies with 10 measuring frequencies per decade.

### 3.1.3.3. Electrode characterization

We first performed measurements on the lead alone, both the proximal and distal electrodes immersed in cardioplegia (NaCl, 110; CaCl<sub>2</sub>, 1.2; KCl, 16; MgCl<sub>2</sub>, 16; NaHCO<sub>3</sub>, 10; and glucose, 9.01 in mM). The software which drives the Solartron can perform fitting with simple models, we use it to perform a preliminary fitting on the electrode characterization measurement. The results are presented on Figure 3-5.

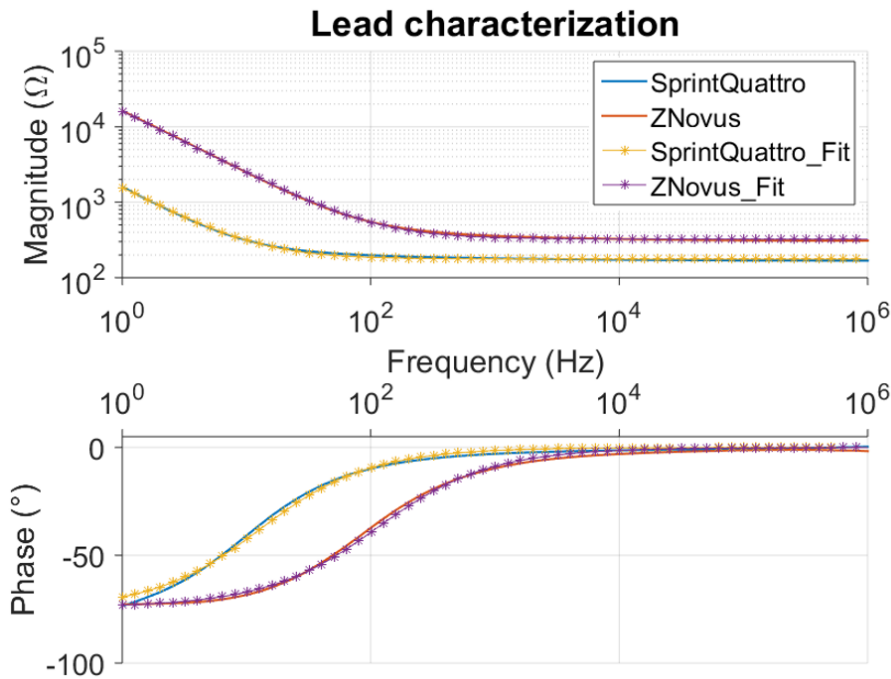


Figure 3-5: SprintQuattro and ZNovus characterization and fitting curves

On the characterization spectra, we can visualise the electrode-medium pseudo-capacitive behaviour under 10<sup>2</sup> Hz. We have fitted the measurements with the ZView software, using a simple model containing a resistance and a CPE in series, as represented on Figure 3-6. The resulting error between the measured and simulated data did not exceed 2.10<sup>6</sup>%. The parameters extracted from this equivalent circuit are the resistance R, and K and  $\alpha$  for the ZCPE (Equation 19 in paragraph 2.2.4.1). These parameters values are presented in Table 3-1.

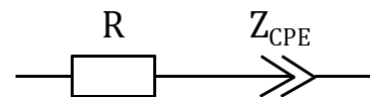


Figure 3-6: Simplified R-Z<sub>CPE</sub> model used to fit the lead characterization

Table 3-1: Solartron fitting parameters for both the SprintQuattro and the ZNovus leads

Parameters	SprintQuattro	Error (%)	ZNovus	Error (%)
R	175.90	1.7E-06	322.90	1.2E-06
K	7087.17	7.1E-06	72780.20	3.5E-06
$\alpha$	0.84	2.3E-06	0.82	9.2E-07

We notice that the R parameter is different between both electrodes, although the cardioplegia conductivity is the same in both measurements (same temperature). This difference is induced by the electrodes' geometry (surface and distance between the proximal and distal electrodes).

#### 3.1.3.4. Bench characterization

In order to complete the characterization of the measurement bench, we measured the impedance of known resistances: 0.1, 1 and 10 k $\Omega$ , over the frequency range of this experiment. The results are presented on Figure 3-7.

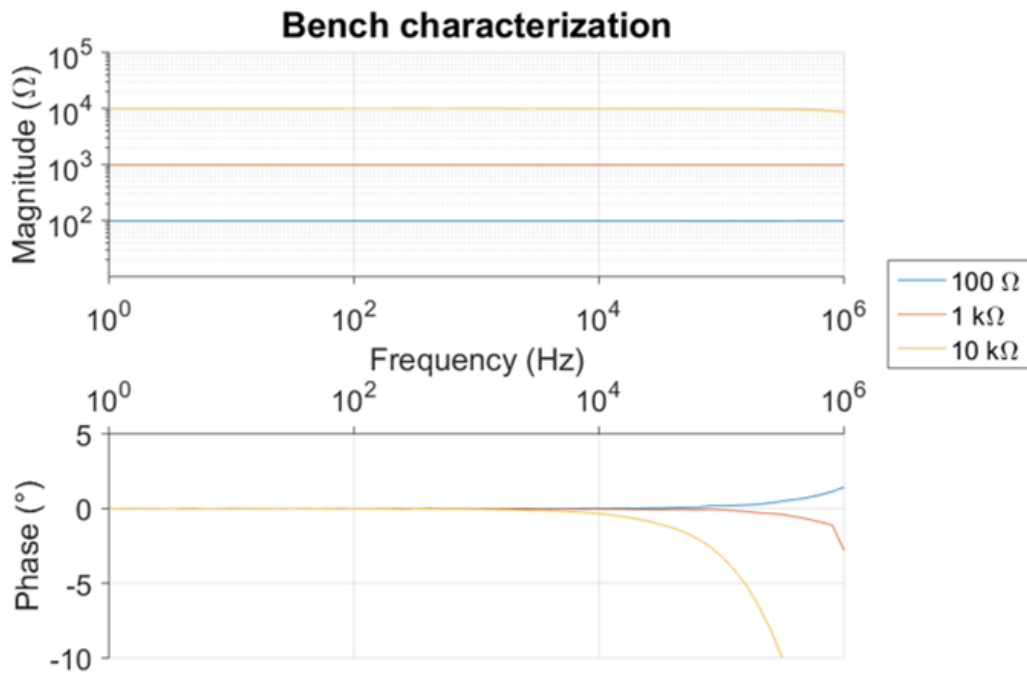


Figure 3-7: Bench calibration with the measurement of three known resistances on the frequency range 1Hz-1MHz

For the magnitude curves, we find the resistance expected values, apparently on the whole frequency range, indicating that the measurement bench induced no band-pass limitation. This observation must be moderated by looking at the phase graph: a deviation from the expected null value appears in high frequencies, especially for the higher resistance value (10 k $\Omega$ ). Fortunately, the magnitude of tissue impedance we measured did not exceed 1 k $\Omega$  in that high frequencies part of the spectrum (see next paragraph). Nevertheless, a precision of few degrees should be kept in mind at 1 MHz.

This result may be related to the Solartron precision characteristic announced in this instrument documentation<sup>22</sup>: at 1MHz, the maximal error of a 1 kΩ impedance measurement is 1%.

Finally, this bench characterization confirms a negligible influence of the in-house fabricated connector.

## 3.2. Results

For this manuscript, we will present the experiments performed with the cardiac lead Sprint Quattro, on swine left ventricles. Then, we will introduce the modelling work done to analyse our measurements.

### 3.2.1. Bode diagram

The impedance magnitude and phase graphs for the ‘healthy’ and the ‘collagen’ conditions are shown on Figure 3-8.

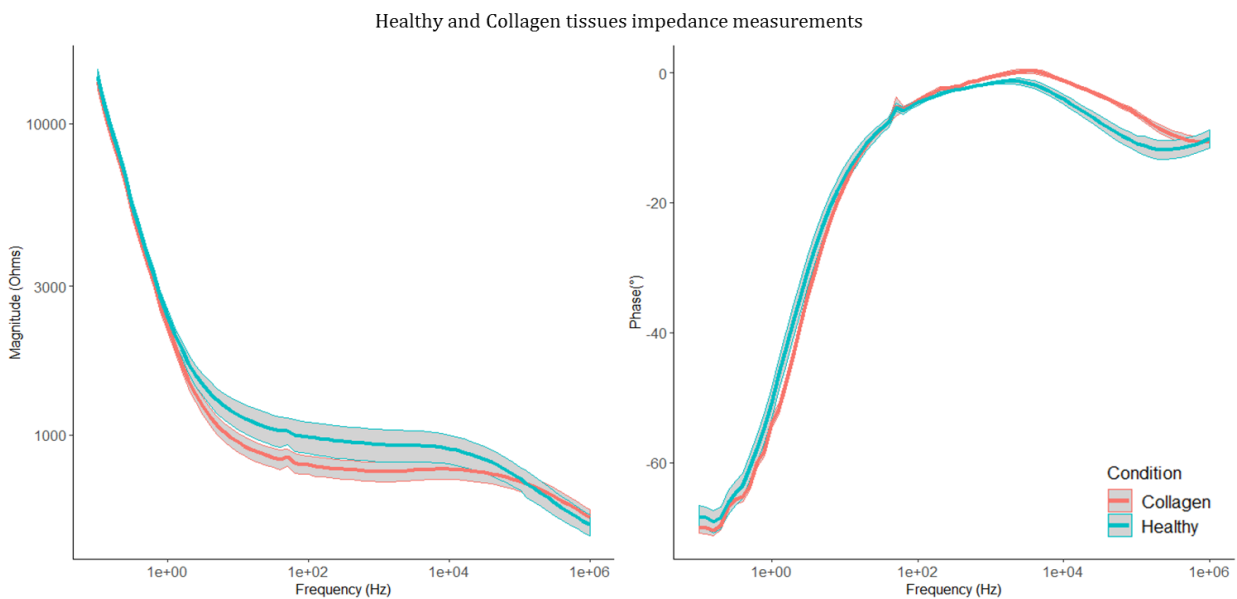


Figure 3-8: Impedance spectra of the mean over the 6 ventricles for both healthy and collagen conditions, the grey ribbon represents the standard deviation over the 6 samples

As we could expect, the curves exhibit the electrode-tissue pseudo-capacitive behaviour of the double-layer effect below 10 Hz, a resistive plateau in the central region [10 Hz-10 kHz], and a second cut-off region around 10 kHz. In the resistive region, a shift in the impedance magnitude is observed, indicating a higher conductivity of the ‘collagen’

<sup>22</sup> [https://mm.ece.ubc.ca/mediawiki/images/8/8b/1260\\_manual.pdf](https://mm.ece.ubc.ca/mediawiki/images/8/8b/1260_manual.pdf)

region, compared with the 'healthy' tissue. Such a difference has already been observed between healthy and ischemic cardiac tissues [116]. The phase presents also a clear difference in the  $10^4$  Hz region.

### 3.2.2. Modelling and analysis

At this step, the impedance spectra may be analyzed in many ways. For these *ex vivo* experiments, we decided to search for an optimal equivalent model. This approach requires to choose one model first, then to run an optimization algorithm that extracts the best values for the model parameters. At the end of this process, each sample is characterized by a set of parameters instead of one Bode diagram, and a statistical analysis may be performed on these parameters.

As developed in the second chapter, the impedance measured in that 2-point configuration is the combination of electrode-tissue interface and tissue impedances. The electrode-tissue interface impedance dominates at low frequencies and that of the tissues dominates the high frequencies.

$$Z_{total} = Z_{interface} + Z_{tissue} \quad (20)$$

Figure 3-9 illustrates this on a typical Bode diagram. Regarding the interface impedance, the Faradaic parallel resistance doesn't appear on the measured frequency range, electrochemical charge transfer is fortunately absent of our experiments. Thus, the interface impedance simply consists in a CPE relative to the interface:  $Z_{CPEi}$ . The tissue part of the diagram is mainly composed of a resistive component and in the high frequency range begins an inflection that we can attribute to the cell membrane capacitive behavior. The measuring frequency range is however not large enough to reach the intra-cellular resistance, this one being too low against the cell membrane capacitance. Thus, the tissue impedance can be represented by a membrane CPE ( $Z_{CPEm}$ ) in parallel to the extracellular resistance  $R_e$ .

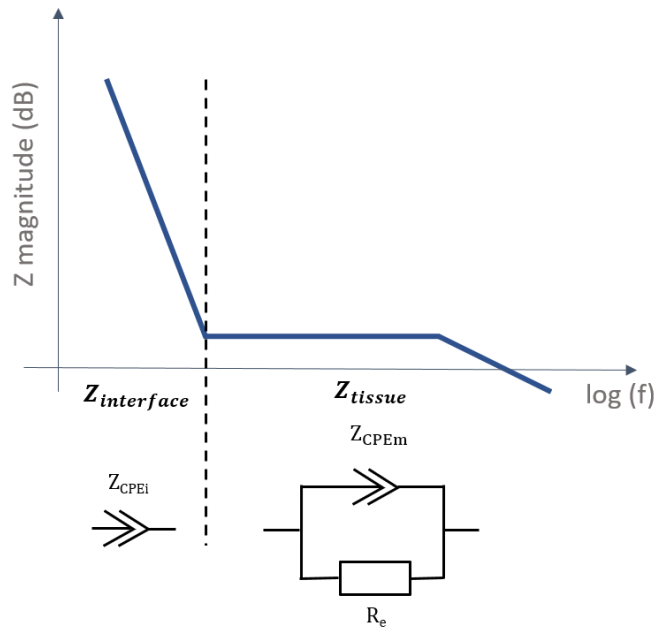


Figure 3-9: Bode diagram of a typical bioimpedance spectrum, accompanied with the equivalent electrical circuit for both the electrode-tissue interface and the extra- and intracellular frontier

$Z_{CPEi}$  and  $Z_{CPEm}$  can be expressed by:

$$Z_{CPEi} = K_i(j\omega)^{-\alpha} \quad (21)$$

$$Z_{CPEm} = K_m(j\omega)^{-\beta} \quad (22)$$

or rather with characteristic frequencies:

$$Z_{CPEi} = \left(\frac{f_\alpha}{jf}\right)^\alpha \quad Z_{CPEm} = \left(\frac{f_\beta}{jf}\right)^\beta \quad (23)$$

$f_\alpha$  and  $f_\beta$  corresponding to the frequencies at which  $Z_{CPEi}$  and  $Z_{CPEm}$  have a magnitude of 1. As explained in paragraph 2.2.4.1, the K parameter in Equation 21 and Equation 22 has units of  $\Omega s^{-\alpha}$ , with Equation 23, we can find that both  $f_\alpha$  and  $f_\beta$  parameters have units of  $(\Omega)^{\frac{1}{\alpha}}$ . Hz.

We must be careful about this notation. The cell membrane contribution ( $Z_{CPEm}$ ) may be related to the  $\beta$  dispersion in the dielectric properties of the tissue but the interface contribution ( $Z_{CPEi}$ ) is not equivalent to the  $\alpha$  dispersion as the “electrode polarization” masks the latter (2.2.4.2).

In the following are exposed two approaches that were carried out; each uses a specific software that implements its own model and algorithm.

### 3.2.2.1. Model 1

This model was directly derived from the former development and gives:

$$Z = \left(\frac{f_\alpha}{jf}\right)^\alpha + R_e // \left(\frac{f_\beta}{jf}\right)^\beta = \left(\frac{f_\alpha}{jf}\right)^\alpha + \frac{R_e}{1 + R_e \left[\frac{jf}{f_\beta}\right]^\beta} \quad (24)$$

The modelling software was developed by Pr. Jocelyn Sabatier of IMS laboratory. It uses a MATLAB internal optimisation function. Initialization of the algorithm is done by a graphical estimation of the parameters  $\alpha$ ,  $f_\alpha$ , R,  $\beta$  and  $f_\beta$ . The model is iteratively optimised until the value of the error criterion does not evolve anymore, the values between two iterations being lower than  $10^{-12}$ . The error criterion is calculated between the measured and the modelled values on both the magnitude and the phase.

We obtain the impedance spectra for each sample fitted with the corresponding model. An example of this graphical fitting is presented on Figure 3-10.

We can see on the graphs that the model fits correctly the measured values even if some divergences are again intensified on the phase graph.

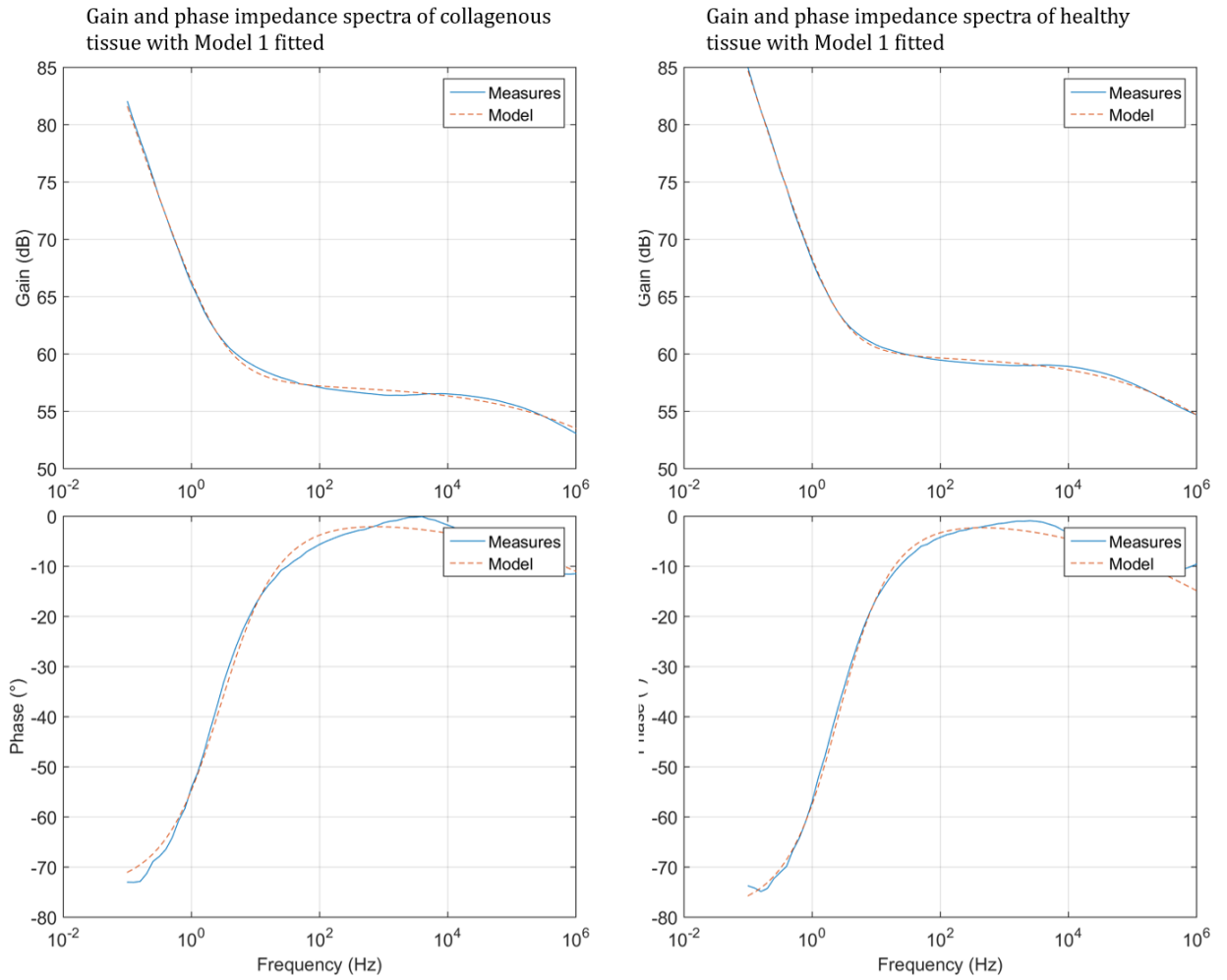


Figure 3-10: Gain and phase impedance spectra of the measured and fitted values of Model 1 for the ventricle n°6

Table 3-2 shows all parameter values found by this software.

Table 3-2: Modelling parameters for the first model for the 6 measured ventricles

Ventricle	Condition	$\alpha$	$f_{\alpha}(\Omega^{1/\alpha}, \text{Hz})$	$R (\Omega)$	$\beta$	$f_{\beta} (\Omega^{1/\beta}, \text{Hz})$
1	collagen	8.57E-01	7.67E+03	8.16E+02	3.07E-01	4.04E+16
	healthy	8.15E-01	1.20E+04	1.04E+03	3.22E-01	5.69E+15
2	collagen	8.38E-01	1.02E+04	1.11E+03	3.20E-01	2.51E+16
	healthy	8.36E-01	8.74E+03	1.34E+03	3.90E-01	3.46E+13
3	collagen	8.24E-01	9.51E+03	8.10E+02	3.26E-01	5.36E+15
	healthy	8.05E-01	1.30E+04	1.33E+03	3.92E-01	3.31E+13
4	collagen	8.43E-01	7.06E+03	7.67E+02	2.87E-01	5.48E+17
	healthy	8.40E-01	7.18E+03	9.04E+02	3.45E-01	7.35E+14
5	collagen	8.30E-01	7.79E+03	6.90E+02	2.75E-01	2.89E+18
	healthy	8.31E-01	7.81E+03	5.49E+02	3.26E-01	1.39E+15
6	collagen	8.26E-01	8.42E+03	7.32E+02	3.29E-01	2.42E+15
	healthy	8.77E-01	6.58E+03	9.80E+02	3.54E-01	4.07E+14

### 3.2.2.2. Model 2

The second model was a more generic one, not based on a specific knowledge as is the case for model 1. It nevertheless considers the fractional law required to fit the interface and cell membrane pseudo-capacitive contributions.

$$Z = R_e \cdot \frac{1 + \left(\frac{jf}{f_1}\right)^\alpha}{\left(\frac{jf}{f_1}\right)^\alpha} \cdot \frac{1}{1 + \left(\frac{jf}{f_2}\right)^\beta} \quad (25)$$

This expression is a product and not a sum of two contributions like in Equation 24. For that reason, the characteristic frequencies  $f_1$  and  $f_2$  cannot be assimilated to  $f_\alpha$  and  $f_\beta$  of model 2. They are nevertheless related by:

$$f_1 = \frac{f_\alpha}{(R_e)^{\frac{1}{\alpha}}}, \quad f_2 = \frac{f_\beta}{(R_e)^{\frac{1}{\beta}}} \quad (26)$$

While  $f_\alpha$  and  $f_\beta$  corresponded to the frequencies at which the  $Z_{CPE}$  magnitude was 1,  $f_1$  and  $f_2$  rather represents the “cut-off frequencies” of the terms  $1 + \left(\frac{jf}{f_1}\right)^\alpha$  and  $1 + \left(\frac{jf}{f_2}\right)^\beta$ .

This second modelling software was developed by Dr. Florian Kölbl of ETIS laboratory, in Python. The model was identified using Non-Linear-Least-Square method on experimental data. In case of no convergence, a second identification using a gradient-descend [118] was used and eventually a third identification using the Powell algorithm [119]. The objective function was set to the Root-Mean-Square Error (RMSE) of the distance between measured and modelled data on the impedance magnitude. The optimisation algorithm is stopped when the Normalised RMSE (NRMSE) of the impedance magnitude does not evolve more than  $10^{-8}$  between two iterations.

As for the Model 1, we obtain the impedance spectra fitted with the optimized model, illustrated on one sample in Figure 3-11.

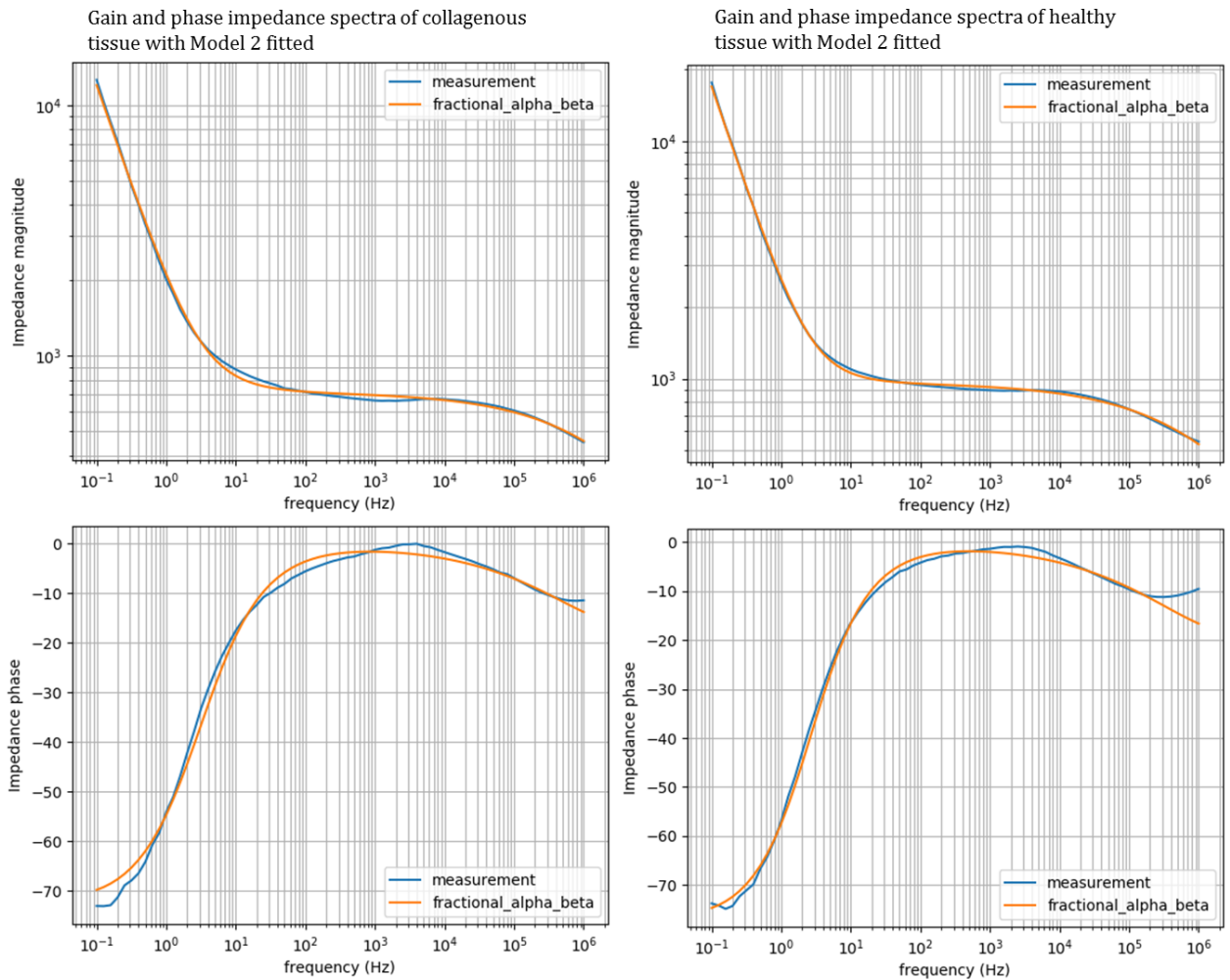


Figure 3-11: Magnitude and phase impedance spectra of the measured and fitted values of Model 2 for the ventricle n°6

The corresponding parameters for the Model 2 are presented in the following Table 3-3.

Table 3-3: Modelling parameters for the second model for the 6 measured ventricles

Ventricle	Condition	$\alpha$	$f_1$ (Hz)	$R_e$	$\beta$	$f_2$ (Hz)	NRMSE
1	collagen	8.48E-01	3.28E+00	7.90E+02	4.49E-01	4.55E+06	3.31E-03
	healthy	7.79E-01	2.84E+00	9.68E+02	1.01E+00	8.52E+04	1.37E-02
2	collagen	8.32E-01	2.55E+00	1.07E+03	5.76E-01	1.69E+06	1.42E-03
	healthy	8.26E-01	1.65E+00	1.32E+03	4.23E-01	3.51E+05	4.81E-03
3	collagen	8.19E-01	2.99E+00	7.84E+02	5.21E-01	1.94E+06	2.60E-03
	healthy	8.01E-01	1.75E+00	1.32E+03	4.12E-01	3.63E+05	3.94E-03
4	collagen	8.39E-01	2.85E+00	7.37E+02	6.14E-01	3.10E+06	3.27E-03
	healthy	8.36E-01	2.27E+00	8.94E+02	3.63E-01	1.95E+06	2.92E-03
5	collagen	8.26E-01	3.04E+00	6.82E+02	6.43E-01	2.87E+06	2.29E-03
	healthy	8.14E-01	4.36E+00	5.30E+02	4.14E-01	3.86E+06	6.53E-03
6	collagen	8.16E-01	3.12E+00	7.12E+02	4.24E-01	2.88E+06	7.89E-03
	healthy	8.70E-01	2.68E+00	9.58E+02	4.17E-01	1.29E+06	5.46E-03

### 3.2.2.3. Comparison between both parameters sets

At this step, we can briefly compare the values of the parameters that we obtained using Model 1 and Model 2 optimization. The values for parameter  $\alpha$  are quite identical. The values for parameter  $R_e$  are similar. Regarding the parameters  $f_\alpha$  of Model 1 and the  $f_1$  of Model 2, let us remember the relation that we could expect between them (Equation 26): indeed, this relation is verified for the extracted values. In contrast, the obtained values for the  $\beta$  parameter are quite divergent between both optimization algorithms, which also has a consequence on the extracted values for parameters  $f_\beta$  of Model 1 and  $f_2$  of Model 2, as they are related in the same way as  $f_\alpha$  and  $f_1$  (Equation 26).

### 3.2.2.4. Statistical analysis and discussion

The extraction of the model parameters allows us to run statistical tests. We used the Wilcoxon-Mann-Whitney to compare the five model parameters of the 'healthy' and 'collagen' conditions. Statistical analysis was performed using R (R Core Team, 2017).

The results are presented in Figure 3-12. The p-values are indicated on the plots for each parameter.

In Model 1, distributions of parameters  $\alpha$  and  $f_\alpha$  are not different for the 'healthy' and 'collagen' conditions, meaning that the  $Z_{CPEi}$  has constant characteristics. This suggests that the structural collagen does not influence the properties of the electrode-tissue interface, at least in that "acute" characterisation. This is logically related to the coincidence of both 'collagen' and 'healthy' impedance in the pseudo-capacitive low frequency region of the spectrum (see Figure 3-8).

Regarding the  $R$  parameter, its distribution is quite large for the 'healthy' condition which makes the difference between both conditions not significant enough ( $p < 0.2$ ). Nevertheless, the tendency in the resistive plateau of the spectrum (Figure 3-8), and in  $R$  value, is a decrease when changing from 'healthy' to 'collagen' conditions. Other published studies give the same tendencies in infracted or fibrotic tissue [62], [116].

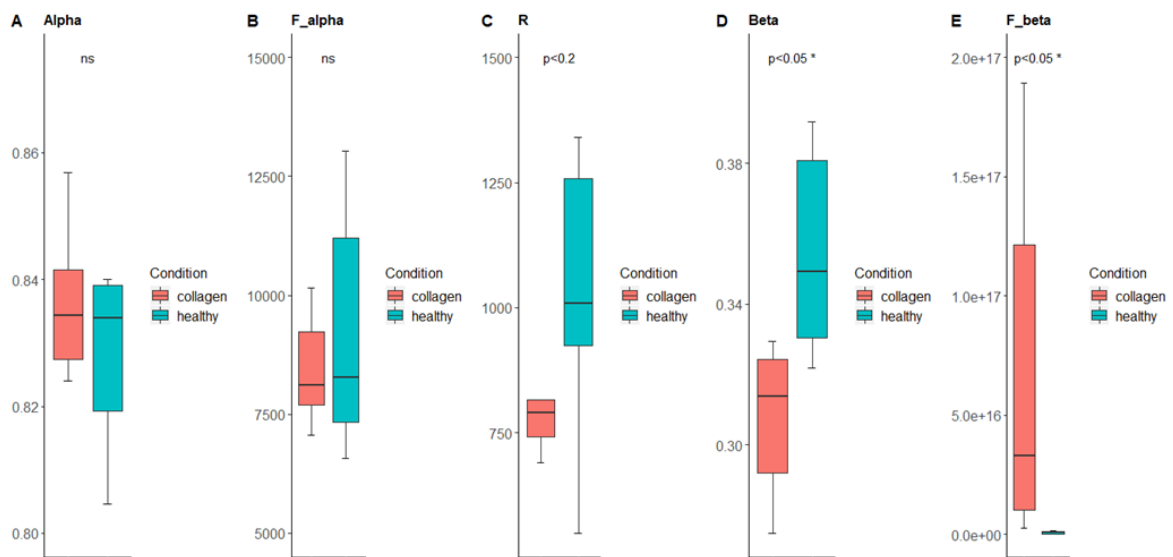
In contrast, the differences between both conditions revealed in parameters  $\beta$  and  $f_\beta$  are significant. Remember that these parameters describe the cellular membrane pseudo-capacitance  $Z_{CPEm}$  or interface between extra- and intra-cellular fluids. These parameters could thus be good candidates to discriminate both tissues by EIS. However, we must take precautions for such an affirmation because the frequency range provides few points in this  $\beta$  dispersion; exploring one more decade in frequency would have allowed a more reliable optimisation of these parameters.

Let us come now to the data of Model 2. In Model 2, distributions of the  $\alpha$  parameter are clearly not different. This parameter is mainly related to the electrode surface roughness [80], a property that does not differ in the both conditions. For  $f_1$ , the distributions for 'healthy' and 'collagen' conditions are not so similar but not significantly different. Interpretation of this is more delicate as  $f_1$  depends not only on the electrode interface behaviour but also on  $R$  value. For  $R$  parameter, we find the same results as for Model 1, as one would expect, this parameter representing the same thing (resistive plateau).

Contrary to Model 1, the parameters responsible for the high frequency behaviour,  $\beta$  and  $f_2$ , are not significantly different.

Finally, Model 2 seems to present less interest than Model 1 to discriminate both tissues. Furthermore, Model 1 was biophysically inspired with the different data of the literature, which provides a more direct access to the physical meaning of its parameters.

### I. Statistical analysis on the parameters of the Model 1



### II. Statistical analysis on the parameters of the Model 2

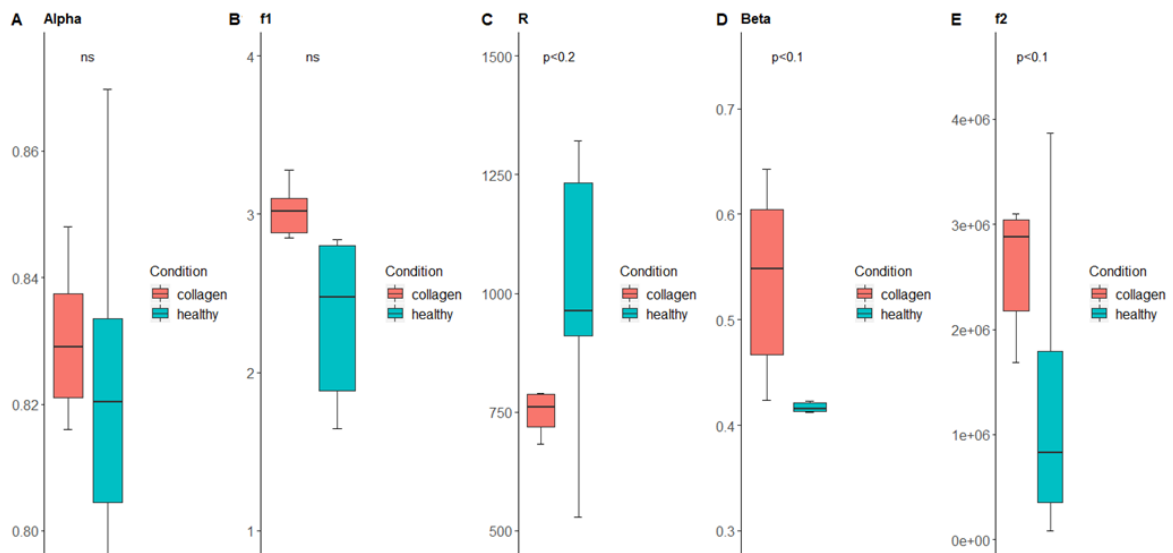


Figure 3-12: Box-and-whiskers plots for the parameters difference of both the healthy and collagen (ns = not significant,  $p>0.5$ )

### 3.3. Conclusion

In this chapter, we adapted an impedance measurement bench based on the classical Solartron instrument, to obtain a reference database of bioimpedance measurements of cardiac tissues, using human pacing leads. We have presented the results for the swine's LV; this preliminary database was completed with many other measurements, using other cardiac leads as the Z Novus Capsure and on sheep's right ventricles. The extra-data are available in Appendix C.

Then we studied the impedance differences between normal and altered tissue, searching for a tissue having fibrotic properties. We wanted to know whether EIS measurement allowed the discrimination of a healthy tissue from a "fibrotic" tissue. Access to real cardiac fibrotic tissue was not possible as the tissue under test was a "healthy" cardiac tissue. Thus, the altered tissue investigated in that differential study was chosen in a zone rich of structural collagen, knowing that the collagen is one of the main components of fibrotic tissue: this is a clear limitation of our study. Its main interests, however, are to have implemented a method of electrical characterization and modelling of cardiac tissues using human stimulation probes.

We can say that the spectra of both kind of tissues are different, on the [10 Hz ; 1 MHz] frequency band. Modelling is a method allowing us to quantitatively study these differences. The results showed that a "biophysical" model enabled more direct interpretation regarding tissue or interface properties, even if  $Z_{CPE}$  are empirical modelling components. The parameters describing the  $\beta$  dispersion ([10 kHz; 1 MHz]) seem to be good "markers" to discriminate the normal and altered tissues. However, extending the measurement from 1 MHz to 10 MHz would be useful to verify this point.

Finally, observing the phase graphs, we noticed that phase values at 100 kHz seemed to be significantly different between both conditions. A simple mono-frequency measure of impedance phase around this frequency could be adequate to discriminate normal and fibrotic tissue.

Despite the encouraging results of this approach, the biological model stays a simplified model of fibrosis and cannot be representative of all the mechanisms occurring during leads implantation. Furthermore the measured tissues were non-contractile, another aspect that is far from *in vivo* conditions.



## CHAPTER IV

# ELECTRICAL IMPEDANCE SPECTROSCOPY MONITORING OF *IN VITRO* CARDIAC FIBROSIS

The previous chapter has presented an investigation of EIS performed on cardiac tissues of different natures. The present one exposes the *in vitro* experiments, where we can focus on one cellular actor of fibrosis: the fibroblast. Thus, we have developed a **simplified model** of cardiac fibrosis *in vitro*, culturing **human cardiac fibroblasts** for their electrical and biological characterization over time. Their differentiation into myofibroblasts can be spontaneous or accelerated using a growth factor. The cultures were developed in wells containing golden electrodes in order to obtain the electrical signature and on glass coverslips to study the phenotype modifications. Electrical characterization is based on impedance spectroscopy and biological characterization relies on classical immunocytochemistry.

First, the electrical cellular impedance was monitored with an industrial instrument, the xCELLigence Real-Time Cell Analyser-Dual Purpose (RTCA-DP). This equipment provides a unique cellular index (Cell Index) combining impedance measurements at three different frequency points. The Cell Index (CI) measurement was performed along 6 days *in vitro*, in parallel to the immunocytochemical characterization, in order to search for potential correlation between the electrical measurements and phenotype modifications. Although xCELLigence is a well-known label-free assay platform used to monitor cellular cultures evolution, our experiment exhibits unreported results on an *in vitro* cardiac fibrosis model.

As the xCELLigence EIS measurement is relatively locked in terms of frequency exploration, giving a unique index, we performed also impedance measurements over a wide frequency range using the Solartron 1260, that provides impedance magnitude and phase on each frequency point. The underlying question was whether we can increase the sensitivity of the xCELLigence electrical signature or have additional information.

This chapter begins with the material and methods of the *in vitro* model, including the description of the cell line, of the culture protocol for each type of characterization, and the protocols of both monitoring techniques, biological and electrical. The results of both characterization techniques are then presented and discussed. Then we will broaden the discussion on xCELLigence characterization results with measurements of impedance spectra highlighting the results at individual frequencies.

## 4.1. Material and Methods

For the development of the cellular model, we used Human Cardiac Fibroblasts (HCF). This part presents the cell culture conditions in order to obtain both electrical and biological characterizations. The immunocytochemical characterization principle will be detailed as well as the protocol of staining. This part only presents the protocol for the xCelligence impedance measurements and not for the complete impedance spectroscopy measurement which will be presented later in this chapter.

### 4.1.1. Cell culture protocol

The cell line we used is Human Cardiac Fibroblast (HCF, Cell Applications, Inc., USA), primary cells extracted from healthy adult human heart tissue.

For an ideal multiplication, fibroblasts were cultured in T75 cell culture flasks (ThermoFisher, USA) in the dedicated Fibroblast Growth Medium (FGM, Cell Applications, Inc., USA). Cultures were maintained at 37°C in a CO<sub>2</sub> incubator (5% CO<sub>2</sub>, 95% humidity). Growth medium is replaced every three days. When the cells arrive at confluence, meaning that they cover the totality of the flask's bottom, they are splitted in different flasks, this step is called passage. For a passage, cells were rinsed with DPBS (w/o Ca, w/o Mg, Sigma-Aldrich, USA) and treated with trypsin-EDTA (Gibco, France), which detach the cells. This cell line is considered stable until the 8<sup>th</sup> passage by the supplier. At each passage, cell samples (at a density of 1.10<sup>6</sup> per tube) were frozen at -80°C in FGM, 10% DiMethyl SulfOxide (DMSO, ≥ 99,5%, Sigma-Aldrich) in order to repeat the experiments.

### 4.1.2. Cell cultures for xCELLigence experiments

To measure the cellular impedance, the cells were cultured on xCELLigence 16-well plates (ACEA Bio, USA) composed of 16 culture wells represented in Figure 4-1.A, bottom-covered with golden electrodes. The electrodes cover approximately 80% of the bottom and are interleaved as represented in Figure 4-1.B. The well diameter is about 5 mm ± 0.075 mm, and the global volume of a well is of 270 µl ± 10 µl.

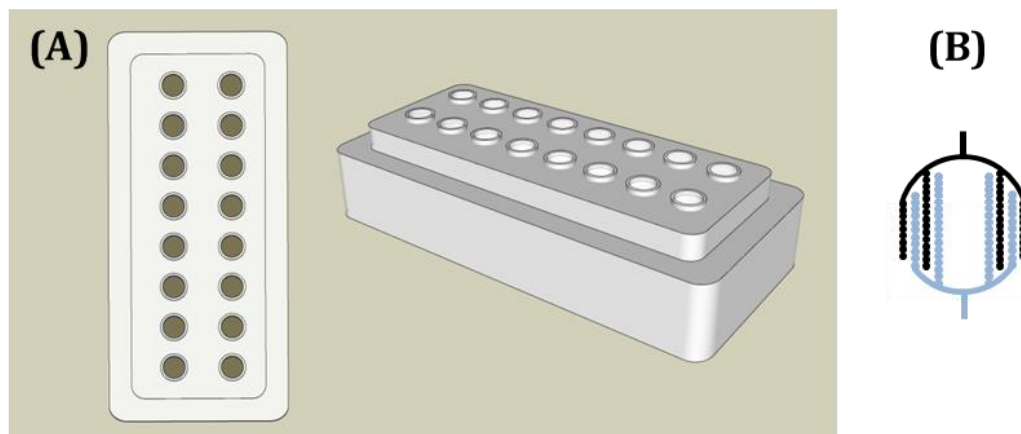


Figure 4-1: (A) 3D representation of the xCELLigence plate used for the measurements; (B) Schematic representation of the electrodes' repartition at the bottom of the culture wells

Four sets of measurements were conducted: one at the third passage (**P3**), two at the fourth passage (**P4<sub>1</sub>** and **P4<sub>2</sub>**), and one at the fifth passage (**P5**).

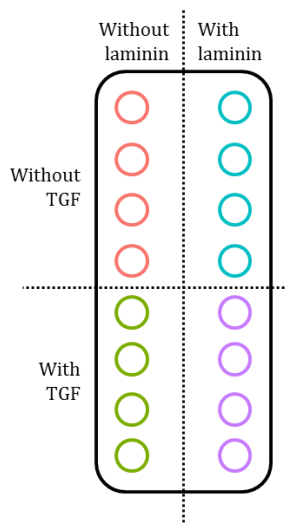


Figure 4-2: Representation of the conditions repartition in the xCELLigence plate

For each set, half of the wells were coated with 50  $\mu$ L laminin (8 wells) (Laminin from Engelbreth-Hom-Swarm murine sarcoma basement membrane, Sigma-Aldrich, France), during 3 hours before the seeding. The other 8 wells did not receive any coating. CFs were seeded at a density of  $1 \times 10^4$  cells per well, in 200  $\mu$ L FGM. In each group (coated and non-coated), two conditions were studied: with or without TGF- $\beta$ 1 (Sigma-Aldrich, USA). Thus, half of the wells (4 with laminin and 4 without) were supplemented with 0,05% TGF- $\beta$ 1. In this study, the condition without laminin and without TGF- $\beta$ 1 will be called **sham**, the one without laminin but with TGF- $\beta$ 1 will be called **tgf**, and the conditions with laminin and without/with TGF- $\beta$ 1 will be respectively called **lam** and **lam\_tgf**. You can see on Figure 4-2 an example of the repartition of the culturing conditions; for each set the repartition was changed, conserving four neighbouring wells for the same condition. With four wells per condition for each of the four sets, we obtain a total of 16 wells for each culturing

condition.

The medium was changed every 3 days. These changes can induce fluctuation in the impedance measurement of variable amplitude.

### 4.1.3. Cell growth characterization

HCFs were cultured into 6-well plates, in the same four conditions (without/with laminin, without/with TGF- $\beta$ 1) at a density of  $2 \cdot 10^5$  cells per well. Every 24 hours we detached the cells after a DPBS (w/o Ca, w/o Mg, Sigma-Aldrich, USA) rinse and a trypsin-EDTA (Gibco, France) treatment. Trypan Blue Stain (0,4%) (ThermoFisher Scientific, France) was added with a 50% proportion to the measured volume of cells and colored the dead cells blue. Cells were then counted using the Countess™ (ThermoFisher Scientific, France) automated cell counter provided with disposable Countess™ cell counting chamber slides that contained two enclosed chambers to hold 10  $\mu$ L of the measured sample. The Countess™ measures a ratio of dead cells into the chamber. It gives the number of living cells per mL with a percentage of viability. This counting allowed us to characterize the proliferation of the CFs depending of their culture conditions. The growth condition, mirrored by the **doubling time**, is obtained using the following formula:

$$T = \frac{t \cdot \ln(2)}{\ln(C_t) - \ln(C_0)} \quad (27)$$

where  $C_0$  is the cell concentration at  $t = 0$ ,  $C_t$  is the cell concentration at the end of the experiment,  $t$  is the total duration of the experiment.  $T$  is the duration representing the

cellular division (the time needed for one cell to divide itself into two cells). This formula is applicable during the exponential phase growth.

## 4.1.4. Immunocytochemistry

### 4.1.4.1. Principle of fluorescent staining

Cell staining is a labelling principle, represented in Figure 4-3, that can be specific to cell type or morphology. It is based on the use of antibodies allowing the visualization of cell and/or cell components under a microscope. The **first antibody** recognizes a unique molecule called **antigen** and is detected by a **second antibody** coupled, in our case, with a green fluorescent molecule.

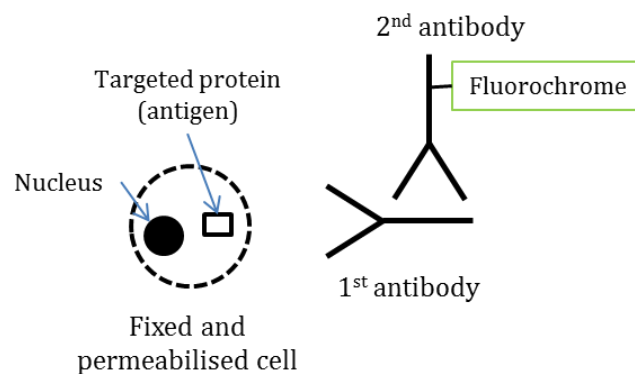


Figure 4-3: Representation of the cell staining principle on a cytoplasmic protein

In order to perform the immunocytochemistry steps, cells must be fixed on their culture substrate (glass coverslips) using paraformaldehyde. The fixation allows us to obtain the cell in the same configuration as they are during culture.

In our case, we want to label the myofibroblasts which express a specific protein called  $\alpha$ -Smooth Muscle Actin ( $\alpha$ -SMA). After cell fixation and a step of cell permeabilization using PBS-Triton X100, the first antibody can access this particular protein. In our case the revelation mechanism is a second fluorescent antibody (FITC) that we will be able to observe with fluorescence microscopy.

### 4.1.4.2. Protocol

In parallel to the EIS-well culturing, the fibroblasts were also cultured on glass coverslip at a density of  $4 \cdot 10^4$  cells per well. Cells were fixed with 4 % paraformaldehyde (Sigma-Aldrich, France) during 30 min and then rinsed and kept at 4°C in PBS until immunocytochemistry. Cells were permeabilised with PBS-5% BSA- 0,5% Triton for one hour at room temperature (RT) under agitation (70 rpm). CFs and MFs were characterized using  $\alpha$ SMA (Invitrogen, France) diluted at 1/500 in PBS- 5% BSA-0,5% Triton antibodies respectively at 4°C overnight. Second fluorescent antibody anti-mouse IgG (whole molecule)-FITC (Sigma-Aldrich, France) was used at 1/200 in PBS (1h under agitation (70 rpm) at RT). The coverslips were mounted on slides using Mowiol and observed with the Nikon Ci-L fluorescence microscope (Nikon, France), magnification 200. The images were captured using the camera Nikon DS-Fi3.

## 4.1.5. xCELLigence measurements technique

### 4.1.5.1. Measurement principle

The xCELLigence Real Time Cell Analyser-Dual Purpose (RTCA-DP) (ACEA Bio, USA) has three cradles enabling 3 separate 16-well plates called E-plates that can be controlled and monitored simultaneously yet independently of one another [120]. The instrument measures the electrical impedance across interdigitated electrodes (two measuring poles) applying an alternative excitation signal with voltage control at three different frequencies (10, 25 and 50 kHz) through the microelectrodes while monitoring the voltage drop across the electrode.

It was previously proven that the measurement does not affect the cells viability [121]. The RTCA-DP analyser was located in a CO<sub>2</sub> incubator at 37°C (5% CO<sub>2</sub>, 95% humidity) and connected to a control unit made of a computer containing the RTCA Software 2.0 which controls the unit and receives, analyses and displays the data obtained from the measurements. The schematic representation of the xCELLigence measurement bench is shown in Figure 4-4

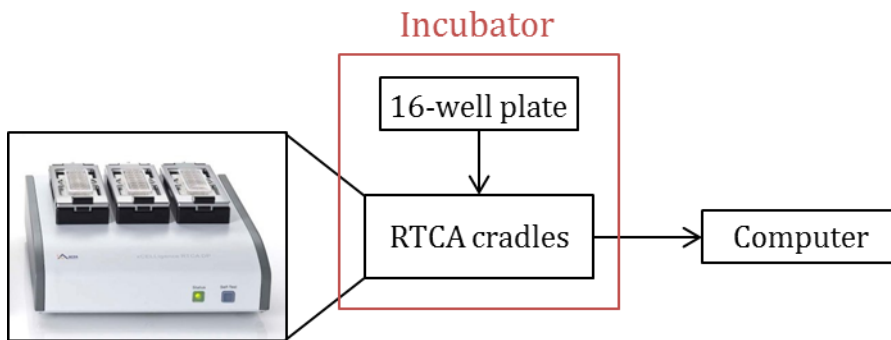


Figure 4-4: Schematic representation of the xCELLigence measurement bench

The software displays the measured impedance which is normalized by a frequency factor  $Z_n$ . This measured impedance is expressed in terms of Cell Index (CI), for each point in time, which is a dimensionless value monitoring among others cell proliferation kinetics, strength of cellular adherence and cell morphology over time [17]. The CI is calculated as follow:

$$CI(t) = \frac{R(f_n, t) - R(f_n, t_0)}{Z_n} \quad (28)$$

where  $f_n$  is the frequency at which the impedance measurement is carried out,  $R(f_n, t)$  is the measured impedance at the frequency  $f_n$  at time-point  $t$ ,  $R(f_n, t_0)$  is the measured impedance at the frequency  $f_n$  at  $t_0$  (time of the background measurement), and  $Z_n$  is the corresponding frequency factor of  $f_n$  [122]. The xCELLigence system measures the impedance at three discrete frequencies:  $f_1 = 10$  kHz,  $f_2 = 25$  kHz and  $f_3 = 50$  kHz, the

corresponding frequency factors are:  $Z_1 = 15 \Omega$ ,  $Z_2 = 12 \Omega$  and  $Z_3 = 10 \Omega$  respectively. The CI is a mean of the signals measured at all these three frequencies.

When there are no cells on the microelectrodes, the measured impedance depends on the electrodes geometry and the electrical properties of the ionic solution in the well. When cells are attached to the microelectrodes, they act like insulators and therefore lead to an impedance value increase.

#### 4.1.5.2. *Measurement protocol*

Cell impedance was recorded every minute for the first three hours, in order to monitor cell adhesion which is a quick phenomenon, compared to cell proliferation and differentiation. After the first three hours, cell impedance was recorded every 15 minutes (until 148 hours) in order to monitor cell proliferation and differentiation. These two phenomena are slower than the adhesion; one measurement every 15 minutes is enough for our experiments to observe significant evolution.

### 4.1.6. Data analysis and visualization

All statistical analyses and plottings were performed using R[stats-1] the PMCMRplus [stats-2], ggplot2[stats-3] and cowplot [stats-4] libraries. Statistical significance was calculated using Kruskal-Wallis and Conover post-hoc tests ( $p < 0.05$ ). Since during the first 3 hours, the impedance was recorded every minute, the recordings of this initial period were subsampled to produce homogeneous time series along the whole experiment

## 4.2. Results

### 4.2.1. Bench characterization

We performed measurement on wells containing the culture medium alone (no cells). To do that, we filled a 16-well plate with the four culturing conditions. We measured the corresponding CI over 90 hours, in the same temperature and humidity conditions (37°C, 5% CO<sub>2</sub>, 95% humidity) than those of cell culturing. The results are presented in Figure 4-5.

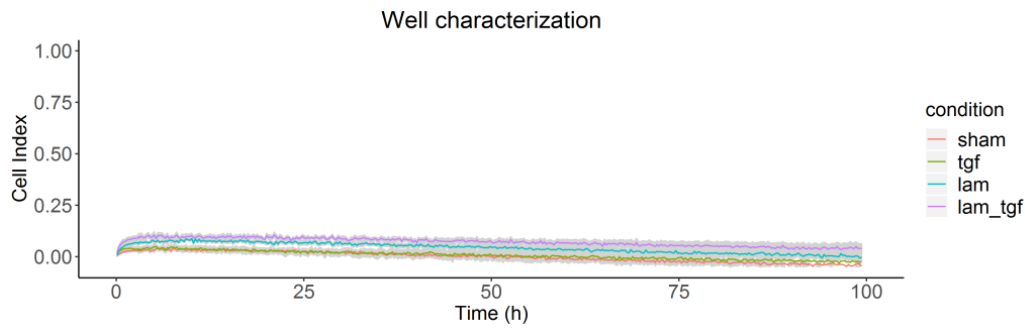


Figure 4-5: CI measurements of well containing the culture medium without cells

We can see that the CI stays around 0 over the whole duration of these measurements, while that of the cellular cultures evolves between 1 and 3, as we will see hereafter. Hence the observed dynamics of CI will be due to the presence and evolution of cells in culture into the wells.

#### 4.2.2. Cell counting

For the P3 and P4<sub>1</sub> sets, we counted the cells every 24 hours during 96 hours of experiment. This allows us monitoring the cellular proliferation over time, depending of the different culturing conditions. Figure 4-6 shows the course of the cell number in each culturing condition.

The cell growth depicted in Figure 4-6 follows an exponential behaviour with little dispersion for culture containing laminin and larger dispersion for the two other culturing conditions (sham and tgf). However, we can estimate the doubling time of the cells based on the exponential interpolation represented by the lines on the different graphs. The values of the doubling time are calculated using the Equation 27. They are introduced in Table 4-1.

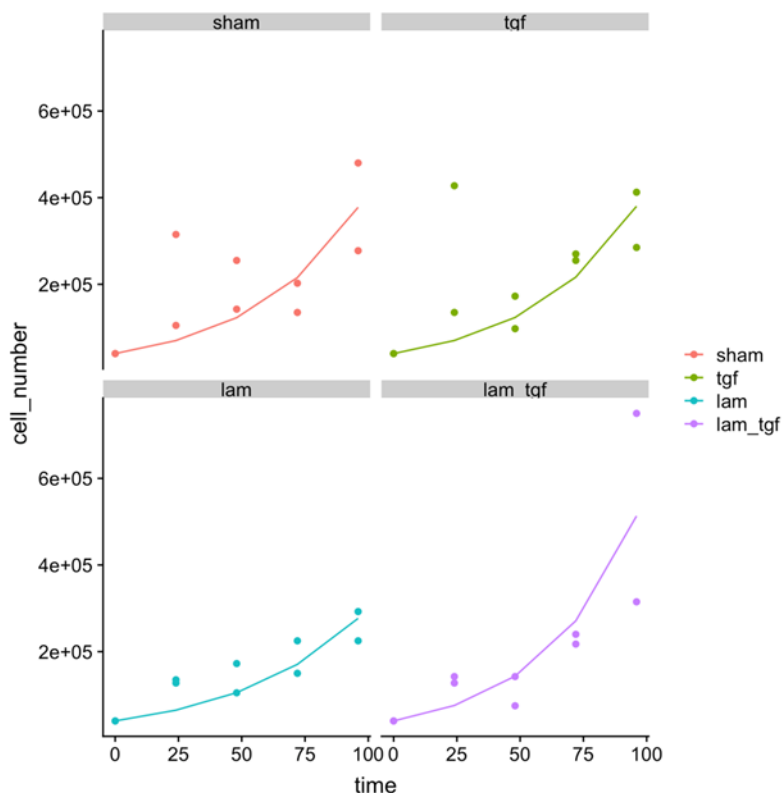


Figure 4-6: Time course of the cell counting every 24 hours during 96h, the represented values are the mean of the counting for P3 and P41 ; the solid line corresponds to an exponential fitting with regression coefficients of  $R_{sham} = 0.7$ ,  $R_{tgf} = 0.61$ ,  $R_{lam} = 0.88$ ,

Table 4-1: Calculated doubling times for each culturing conditions

Culturing condition	sham	tgf	lam	lam_tgf
Doubling time (h)	29.65	29.56	34.4	26.08

These estimated doubling times depicts tendencies of the cellular growth: sham and tgf conditions seem equivalent while in the two laminin conditions; the culture growth seems accelerated by the presence of TGF- $\beta$ 1. Nevertheless, these data are to be taken in account carefully due to the great dispersion among the counting measurements and the little number of passages considered.

### 4.2.3. Cell staining

P3 experiment was used for immunocytochemistry that brings a qualitative visual characterization of the cultures behaviour along the time. The staining was performed at times 24h, 48h, 72h and 96h. Figure 4-7 shows the resulting micro-photographs for the

different conditions. The last column on the right is a zoomed image (x3) on typical cell phenotypes present for each culturing conditions after 96 hours of culture.

At 24h, we can recognize the characteristic elongated shape of fibroblasts and observe cultures with a density seeming higher with TGF- $\beta$ 1, either with or without laminin. At this early stage of the analysis, the presence of TGF- $\beta$ 1 seems to have an accentuating effect on cellular proliferation.

At 48h, the situation has slightly evolved and first cells having the myofibroblasts phenotype appear, with a more branched cytoplasm. The *tgf* condition presents more cells with the MF phenotype in comparison with the sham condition. This comparison is more difficult for laminin cultures because of an immunofluorescent image of lesser quality (*lam* - 48h).

At 72h, we can observe a light accentuation of the population with MF phenotype, except for the sham condition. This leads to clear differential fluorescence intensity between sham and *tgf* conditions. This differential aspect doesn't appear so clearly for the two conditions with laminin.

At 96h, the sham and *tgf* conditions present similar images to those at time 72h. On the extreme right of the figure, a zoom on one typical cell exhibits the difference between the CFs (sham condition) and the MF (*tgf* condition). At the same time, cultures with laminin appear generally denser and with a high proportion of MFs; furthermore, the *lam\_tgf* condition presents a fibrous organization of the whole culture, and this same organization begins to appear in the *lam* condition.

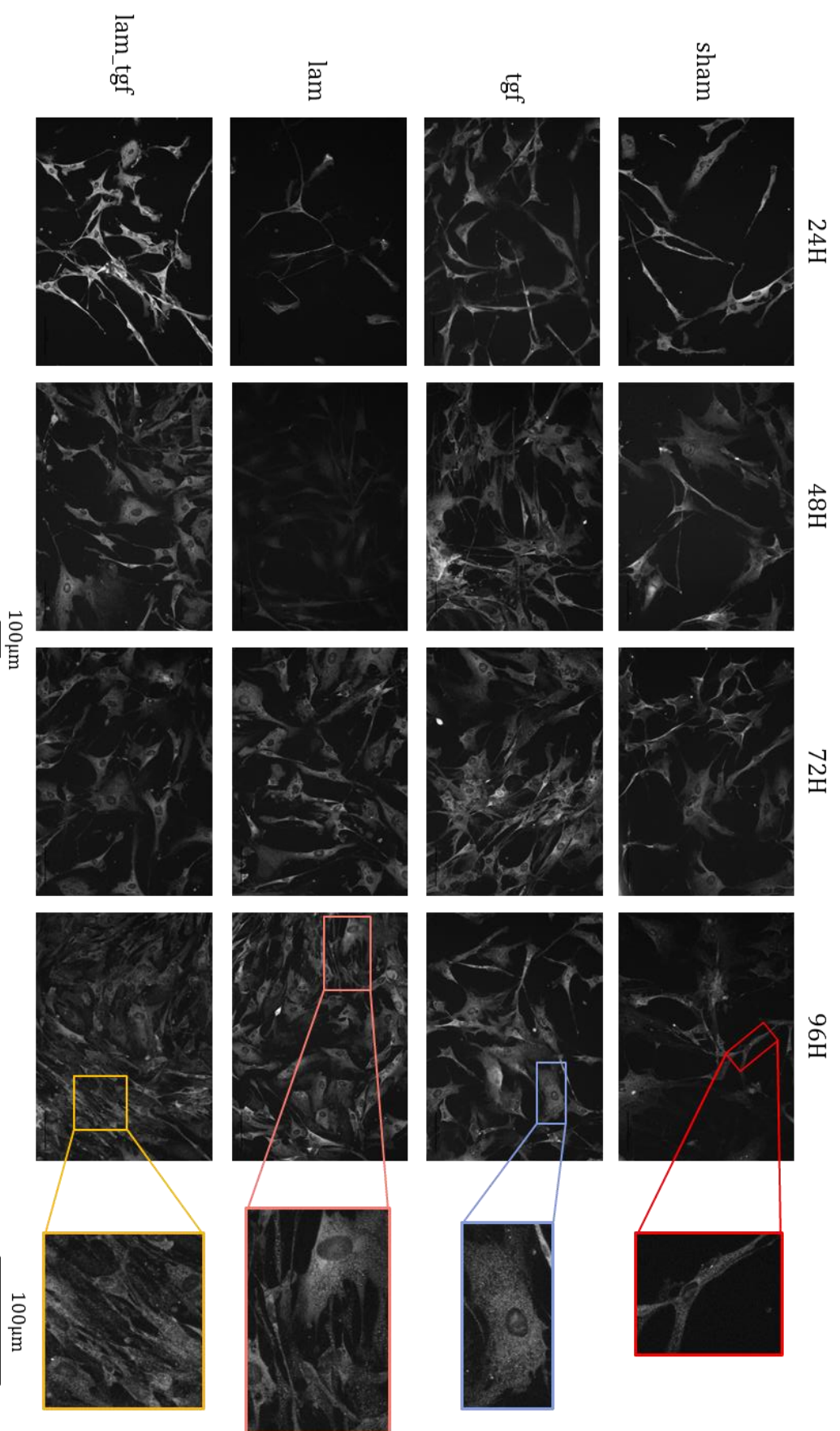


Figure 4-7: Fluorescent staining of myofibroblasts for each condition represented in grey scale; the last column on the right represents a zoomed in-selection (x3) of the main cell phenotype after 96 hours of culture for each condition

#### 4.2.4. Cell Index time course

The results of the 4 sets of CI measurements are presented in Figure 4-8. A global observation indicates that the CI of the lam and lam\_tgf conditions is generally lower than the CI of the sham and tgf conditions. Around times 50 h and 100 h, we can see artefacts of variable amplitude on the CI curves corresponding to medium changes. For the P3 graph, the hours of staining have been reported in order to facilitate the observation between the staining images and the impedance measurements.

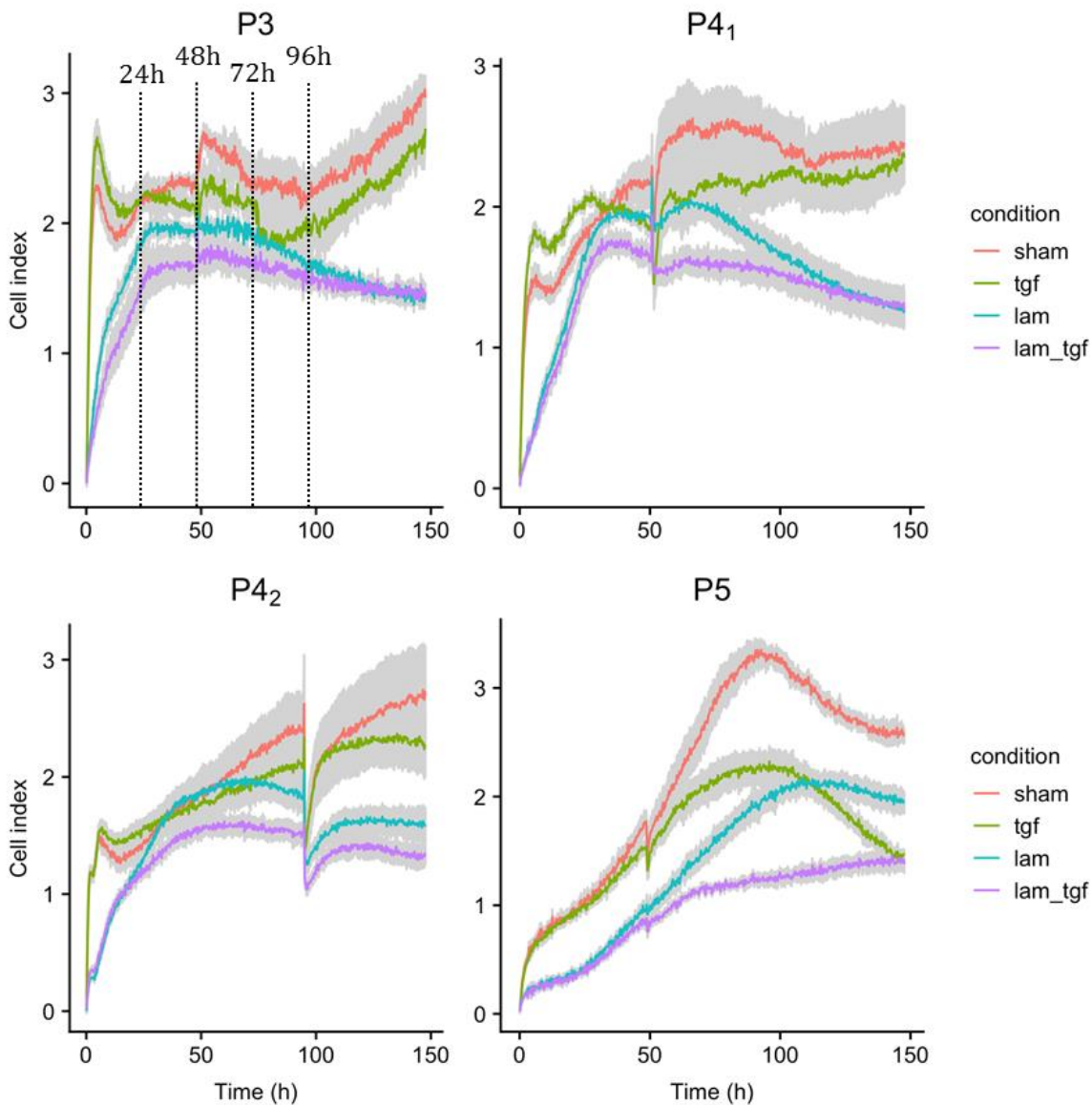


Figure 4-8: Cell impedance recordings. HCFs were cultured with the four conditions described in part 2.3. For each set of measurement, the data are presented as following: the colour plot is the average value and the mean standard error is filled in grey.

A focus on the initial dynamics of the CI reveals a quick increase from 0 to over 1 for the sham and tgf curves, in the first hours of the experiment. On the contrary, for the lam and lam\_tgf conditions, it takes between 10 to 20 hours for the CI to reach 1. For P5, the CI initial dynamics is smoothed for all conditions.

Comparing the sham and tgf curves, we can note that the sham wells have a CI higher than the CI of the tgf wells. With a more detailed observation, we see that for the first hours of

the experiments the sham CI is on average lower than the *tgf* CI, until the two curves cross allowing the sham CI value to go over the *tgf* CI at about 30 hours of experiment. More precisely, this crossing time depends on the set of measurements: the older the passage gets, the more delayed is the crossing time.

Comparing in the same way the *lam* and *lam\_tgf* conditions confirms the tendency of the CI to take lower values in the presence of TGF- $\beta$ 1. This difference is maintained during all the experiment. Differently to the conditions *sham* and *tgf*, a general tendency of the *lam* and *lam\_tgf* curves to a final convergence of CI values is observed, at least for passages P3, P4<sub>2</sub> and P5.

Finally, the CI time course for P3 can be compared to the qualitative imaging results described previously for this passage. For the preparations with laminin, the presence of TGF- $\beta$ 1 induces a difference in CI observable at 24h and 48h, tending to disappear afterwards until being null at the end of the experiment. This behaviour is consistent to the immune-labelling observation. For the preparation without laminin, the MF phenotype begins to be observable at 48h and increases more in the cellular preparation of *tgf* condition; a similar chronologic difference can be seen on the CI *sham* and *tgf* curves.

Nevertheless, it is difficult to see if the differences between all the CI curves are significant or not since the standard errors of the different conditions overlap in some cases. In order to have more quantitative information of the fibroblast's differentiation, we statistically analysed the data as explained in the paragraph 4.1.6.

For a better understanding of the results, we split the duration of the experiments in 3 time intervals: from 0 to 48 hours (Figure 4-9.A), before the expected action of the TGF- $\beta$ 1 on the cells as described in papers [123], from 52 to 100 hours just after the action of the TGF- $\beta$ 1 (Figure 4-9.B) and from 104 to 148 hours (Figure 4-9.C). This division allowed also removing the short interval of medium change artefacts as described in the paragraph 4.1.2. For each part, we calculated the mean CI for all conditions over the 4 sets of measurements, leading to a number of samples  $N = 16$  for each condition.

For the first time-interval, we can see that there is a difference in CI values between the *sham* and *tgf* conditions versus the *lam* and *lam\_tgf* conditions, but no differential effect of the presence of TGF- $\beta$ 1. These results are consistent with Figure 4-8 where the dynamics of the *sham* and *tgf* curves are equivalent between 0 h and 48 h. The trend is the same for the two laminin conditions in the first couple of days. After 50 hours of experiment, all the conditions show significant CI differences.

Focusing on the conditions with TGF- $\beta$ 1 exposure (*tgf* and *lam\_tgf*), expected to accelerate the differentiation of fibroblasts into myofibroblasts, a clear decrease of CI is observed against conditions without TGF- $\beta$ 1 (respectively *sham* and *lam*). The same scheme is visible after 104 h of cultures. With a laminin coating, a significant decrease of the CI is noticeable from 50 h, while the CI appears more stable or decreasing much slower in the absence of laminin.

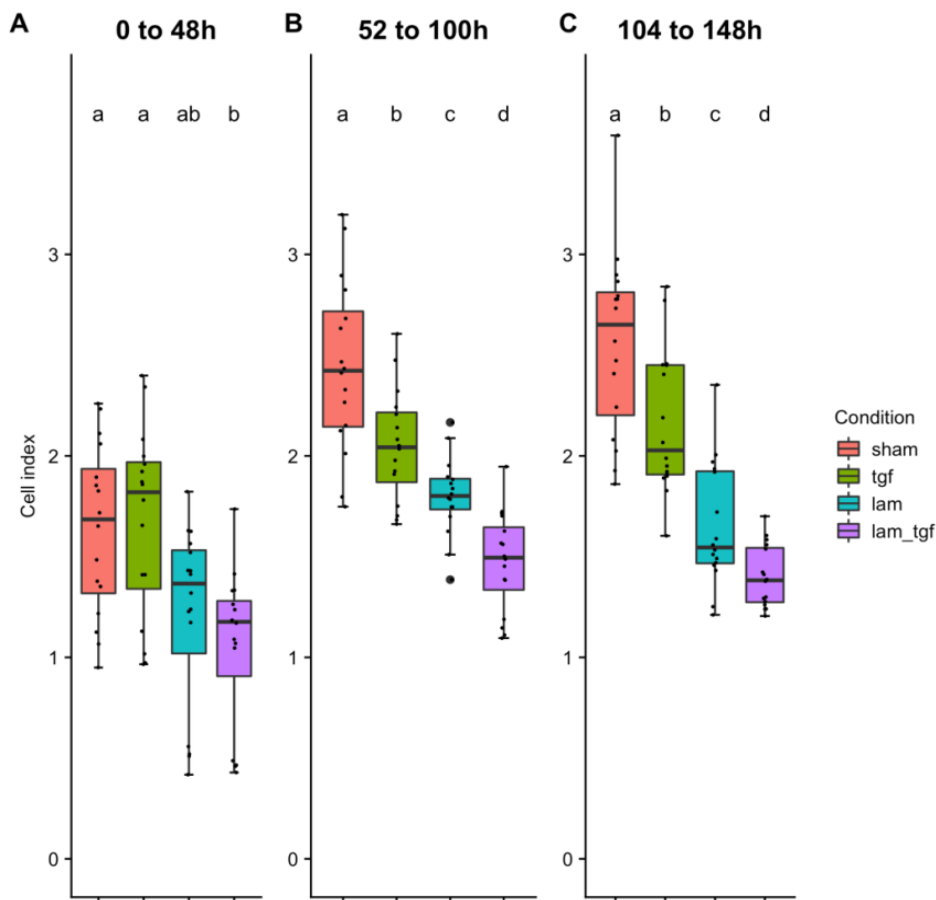


Figure 4-9: Box-and-whiskers plots of mean CI values for the four culturing conditions, along the three time intervals: (A) 0 to 48h, (B) 52 to 100h and (C) 104h to 148h. The significance is expressed with the letters a, b, c and d, when the letter is different, the conditions are significantly different ( $p < 0,05$ )

## 4.3. Discussion

### 4.3.1. Assessment of our characterization method

Our study addresses an unreported impedance-based method for real-time monitoring of the fibrogenic state of a CFs culture. The objective was to study whether the differentiation of CFs in MCFs had a specific signature on the Cell Index, an impedance-based feature measured by the XCelligence system. The xCELLigence is a label-free cellular assay platform that had already been used in different experiments to monitor cell adhesion, proliferation and morphological changes [124]. Primary HCFs were cultured along 6 days, with or without laminin coating, to study the role of this adhesion protein in cultures long-term maintenance. The cultures were characterized in the presence or absence of TGF- $\beta$ 1, a growth factor used to accelerate the differentiation of CFs in MFs.

First of all, the analysis of immunofluorescence imaging shows a noticeable action of TGF- $\beta$ 1 from 48h, as it could be expected [125]. All conditions reveal the presence of MFs at 96h, with their specific phenotype as described in the literature [30], [37], [126]. Their number is increased in images of wells containing TGF- $\beta$ 1, compared to the sham condition. At 96h, cultures with laminin appear denser and the presence of TGF- $\beta$ 1 favours a fibrous organization of cells in the culture well.

- **Adhesion**

The sedimentation of the cells at the bottom of the culture well on the golden electrodes induces two CI behaviours depending on the coating condition. The laminin coating softens this sedimentation what is reflected in smooth initial dynamics of CI, drastically different from the initial peak of CI without laminin, as it was often observed in the literature [124].

- **Proliferation**

After this specific initiation, CI generally continues increasing but slower, reflecting the cellular division, until other events occur as medium changes inducing peak-shaped artefacts; cellular death either by apoptosis, or necrosis; and detachment due to confluency inducing a CI slow decrease.

- **Differentiation**

The quantitative analysis of CI is correlated in several points to the qualitative image analysis. At 48 h, the apparition of the MF phenotype in the images with TGF- $\beta$ 1 is correlated to a noticeable behaviour of the CI: a lower CI is always associated to the conditions with TGF- $\beta$ 1, compared to the respective sham condition ( $CI_{\text{tgf}} < CI_{\text{sham}}$  and  $CI_{\text{lam\_tgf}} < CI_{\text{lam}}$ ). This difference in CI is maintained over time in cultures without laminin, at least until 148 h, while the staining images performed at 96 h confirm a higher population of MFs. This result, associated to the similar cellular growth observed for sham and tgf conditions, argues for a CI signature specific of CFs differentiation in MFs. For cultures containing laminin, the lower CI value of the lam\_tgf condition is generally not conserved over the 6 days and CI traces mostly becomes coincident at the end of the experience; a behaviour that fluorescence images confirm. Lam\_tgf condition is in favour of high-speed growth as seen with the doubling time (paragraph 4.2.2) and fibrous appearance of the culture as observed with fluorescence. It is the condition with the lowest CI value so we can argue that these observations reflect impedance signature of both cell proliferation and a fibrogenic state of the culture.

Besides this qualitative comparison between the CI time course and the fluorescence images (P3 experience), a statistic study was performed on the CI recordings of 4 experiences (cultures of passages 3, 4 and 5). Between 50 h and 148 h, all the conditions show significant CI differences: in this time interval, the CI is a parameter that can be used to discriminate cultures from each other, and interestingly, to identify cultures exposed to TGF- $\beta$ 1 and presenting an increased number of MFs. For all tested conditions, we

obtained a CI signature and interestingly the trend is always the same  $CI_{sham} > CI_{tgf} > CI_{lam} > CI_{lam\_tgf}$  confirming that we can discriminate four culture behaviors using XCELLigence.

*In vivo* studies have reported an impedance decrease of infarcted cardiac tissue compared to healthy tissue. [62], [116]. Myocardial infarction results from coronary occlusion leading to ischemia, cell death, and increased collagen production and scar formation [116], similar to the fibrosis development described in previous chapter. Thus, this can be related to our present result indicating a decrease of the CI in presence of TGF- $\beta$ 1. TGF- $\beta$ 1 induces fibroblasts activation and differentiation, as well as an overproduction of collagen, which is an acellular component of the extracellular matrix. If the cells act as insulators for the current, the extracellular space will carry the current and so the measured impedance will decrease [62], [116].

### 4.3.2. Confrontation of our characterization method

Real-time monitoring using impedance measurements was assessed previously in different cells models. The work of Spörl *et al.* [127] provides new insights into the regulation of human epidermal keratinocyte proliferation and differentiation by membrane cholesterol. Real-time impedance analysis confirms that TGF- $\beta$ 1 treatment induces proliferation, survival, and differentiation of human skin derived precursors in serum-free conditions [128] and that retinoic acid treatment is the most reliable method to differentiate bone marrow human mesenchymal stem cells into neural cells [129]. XCELLigence measurements also allow to choose for the best culture media and coating conditions following multipotent mesenchymal stromal cell proliferation [130] and for the best cocktail to differentiate murine 3T3-L1 preadipocytes into adipocytes [131].

In the context of interstitial cardiac fibrosis, a recent study was conducted on fibroblasts isolated from donors with Heart Failures (HFs) [132].  $\alpha$ -SMA was used, as in our case, to examine the degree of differentiation of MFs, in combination with Ki-67 to follow their proliferative capacity. Analysis of cellular phenotypes indicate that in fibroblasts isolated from HF hearts, MFs are the predominant cell type, and a substantial fraction of these MFs retains the capacity for proliferation (55%), attesting MF involvement in fibrosis. Furthermore, the expression of fibrosis-related gene such as TGF- $\beta$ 1 signaling pathways was activated in HF MFs, compared to non-HF fibroblasts, supporting an important role of this signaling pathway in fibroblast differentiation and fibrosis development.

### 4.3.3. Potential of our characterization

There are currently no therapies that can prevent or reverse fibrosis. As suggested by Zhao *et al.* [133], metabolic alterations are increasingly recognized as an important pathogenic process that underlies fibrosis across many organ types. As a result, metabolically targeted therapies could become important strategies for fibrosis reduction [132]. As reviewed in Yan *et al.* [134], the real-time impedance monitoring can screen drug activity and toxicology. Our *in vitro* fibrosis signature is a good candidate to test pharmacological compounds targeting fibrotic metabolic endpoints. Our method will complement the classic 2D-monolayer cultures or 3D-organoid models of primary or cell

line-derived fibroblasts and *in vitro* high-throughput assays developed to screen for drugs that target RNA or protein for example.

We saw that impedance measurement allows us to correlate biological changes with electrical characterization in an effective and repeatable way. Even if this type of characterization is convenient due to the standardization of the CI value, it can yet be broadened using impedance spectroscopy, exploring the complete impedance spectrum. This can help us finding a frequency range with bigger sensitivity to monitor the fibroblasts differentiation.

## 4.4. Impedance spectroscopy characterization

The xCELLigence system allowed us a preliminary investigation about cultured cardiac fibroblasts evolution over time when exposed to TGF- $\beta$ 1. We will now study the evolution of the complete spectrum. First a quick description of the measurement bench with the Solartron will be detailed, followed by its characterization. We will then discuss the results and conclude about the biological and electrical characterizations of cultured human CFs.

### 4.4.1. Solartron 1260

#### 4.4.1.1. *Measurement principle*

The Solartron 1260A (Ametek, USA) is an impedance analyser considered as one of the most reliable lab instruments for impedance measurements, especially for bioimpedance measurements. With a frequency span from 10  $\mu$ Hz to 32 MHz, this analyser has a wide frequency range allowing to perform measurements at very low frequencies, with a high level of precision.

It performs a frequency sweep on the wanted frequency range and can be driven either by current or by voltage. The frontend of this instrument is quite simple, it has almost not evolved since the Solartron 1260 creation, but it can be controlled using different softwares. In our case we used the software ZPlot (Ametek, USA) to create the measuring signal and the software ZView (Ametek, USA) to plot the results. This latter software enables to use different types of representations as Cole plots, or Bode plots. We chose the Bode representation to better highlight the role of frequency.

#### 4.4.1.2. *Measurement protocol*

Cells were cultured in the same 16-well plates than for the xCELLigence experiments. Same culturing conditions were used. As the Solartron 1260 performs frequency sweep and as our bench allows measurement on one well at a time, cell impedance was only recorded twice a day, during 5 days *in vitro*. The measuring signal was driven with a

voltage level of 100 mV, covering the frequency range from 1 Hz to 1 MHz, and we used a logarithmic repartition of the frequencies with 10 measuring frequencies per decade.

During the whole experiment, the plate is placed in an incubator, so the culture is maintained at 37°C with 5% CO<sub>2</sub>, 95% humidity.

#### 4.4.2. Bench description and characterization

For this measurement bench, two different characterizations are necessary. The characterization bench is shown in Figure 4-10. The 16-well plate is placed and locked on an in-house fabricated connector that hosts a specific printed circuit board at its bottom face. This board wires the IN/OUT pins of the wells plate to coaxial connectors and to a bus intended to control the on-circuit switches. This “front-end” stays in the incubator during the whole duration of the experiment and is linked to an Arduino-based console. This in-house designed console enables to select the well under test. This specific bench allowed to perform the impedance spectrum measurement, and to switch wells without opening the incubator. The coaxial connectors are wired up directly to the Solartron 1260, itself controlled with a computer.

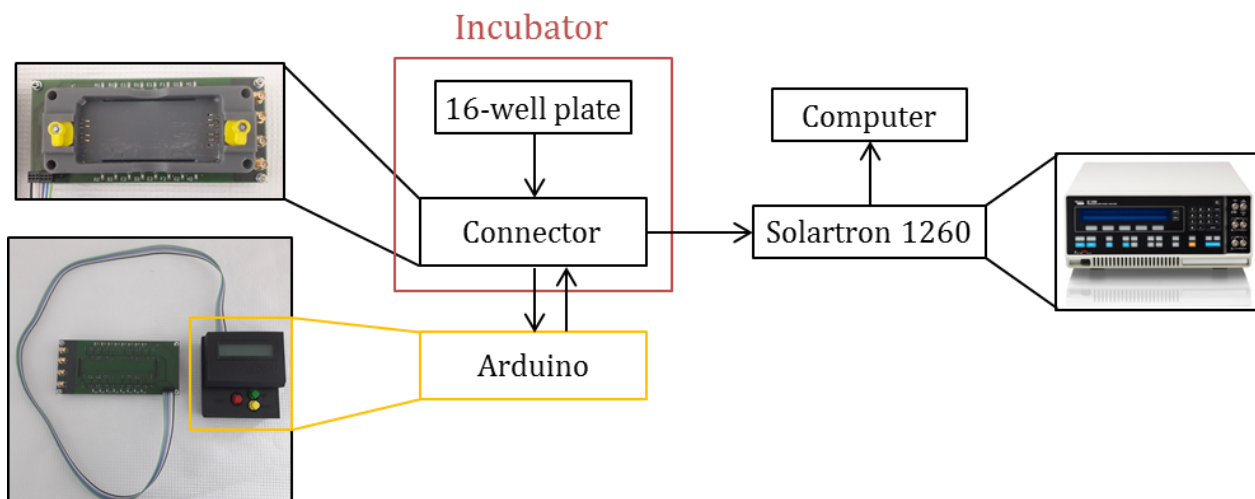


Figure 4-10: Schematic representation of the Solartron measurement bench

Unlike the xCELLigence bench, which is an industrial and calibrated one, this test bench has several components developed by us to adapt it to the 16-well plates. The first characterization of the bench consists in its electrical calibration.

#### 4.4.2.1. Electrical characterization

For the electrical calibration of this bench, we performed impedance measurements with a saline solution (DPBS w/o Ca, w/o Mg, Sigma-Aldrich, USA) in the same conditions of heat and humidity than our experiment. Each well was characterized, with a sensing signal of 100 mV, on a frequency range from 1Hz to 1MHz.

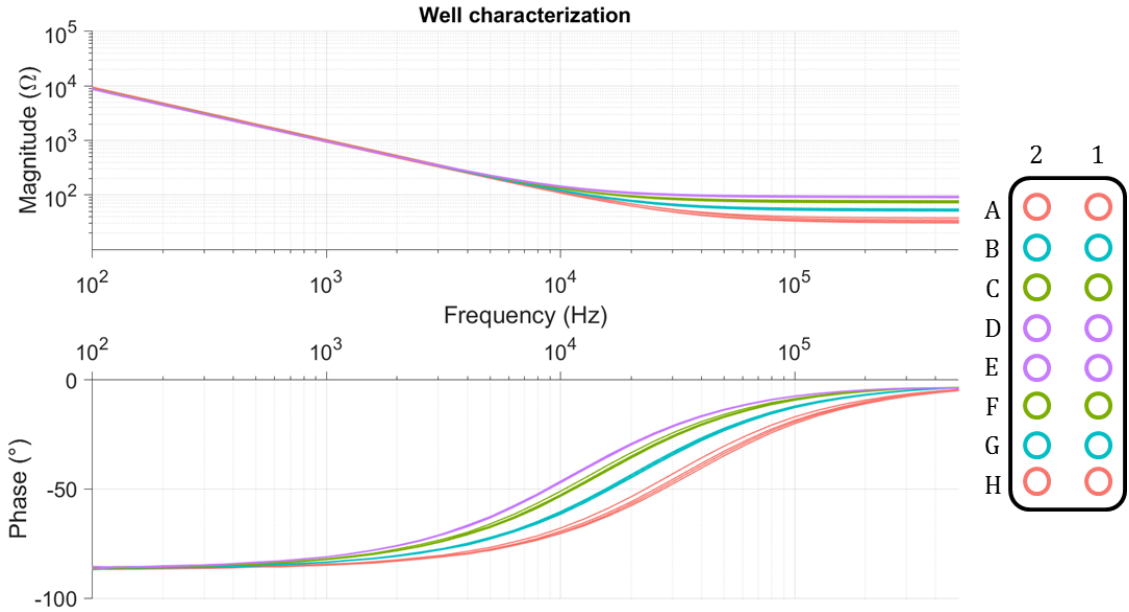


Figure 4-11: Impedance spectra of the 16 wells filled with DPBS, the frequency range of the graphs is reduced to improve the readability of the measurements

The first thing we noticed is that depending on its position on the plate, a well does not have the same level of impedance. A shift in the resistive plateau was noticeable and correlated to the position of the well on the plate, as shown in Figure 4-11. This shift is equivalent to a small resistance that comes in series with the impedance under measurement.

In order to cancel this shift, we applied a correction on the real part of the impedance measurement. We took the wells A and H as a reference and we simply calculated the difference of the real part for the wells B-G, C-F and D-E respectively as followed:

$$R_{corr1,2,3} = \text{Re}(Z_{B-G,C-F,D-E}) - \text{Re}(Z_{A-H}) \quad (29)$$

$R_{corr1,2,3}$  is a correction coefficient that has been automatically applied for further impedance measurements.

Observing Figure 4-12, we see that with the correction coefficient, the impedance spectrum becomes independent of the well position on the plate. The three xCELLigence measuring frequencies are also indicated on the graphs; these frequencies are placed just on the curved portion of the spectrum, at the transition between the capacitive and resistive regions. According to theoretical developments of chapter II, the 10 kHz point is in the interface medium-electrodes region and the 50 kHz point is closer to the medium resistivity region.

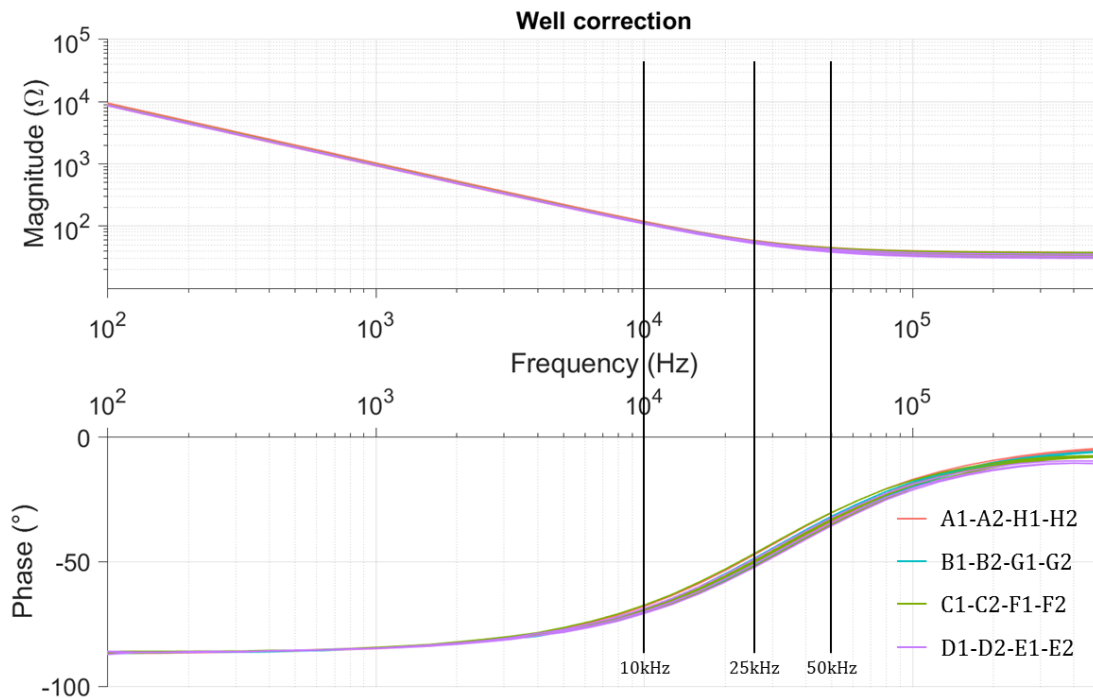


Figure 4-12: Impedance spectra of the 16 wells after the application of  $R_{corr}$  correction coefficient, the three xCELLigence measuring frequencies are represented; the frequency range of the graphs is reduced to improve the readability of the measurements

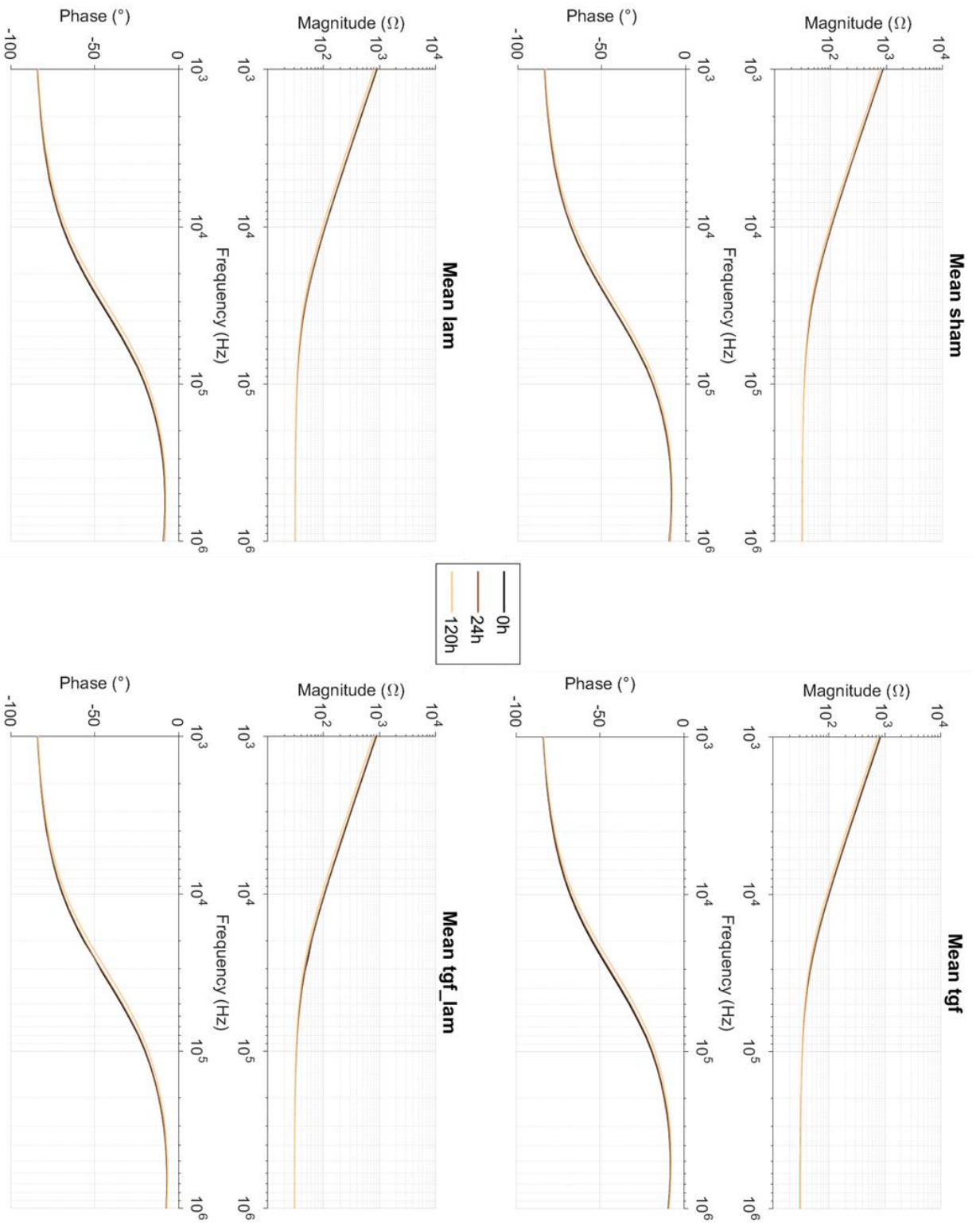


Figure 4-13: Magnitude and phase impedance spectra for each condition over 120 hours; each curve is the mean of 4 wells with the application of the correction coefficient; the frequency range of the graphs is reduced to improve the readability of the measurements

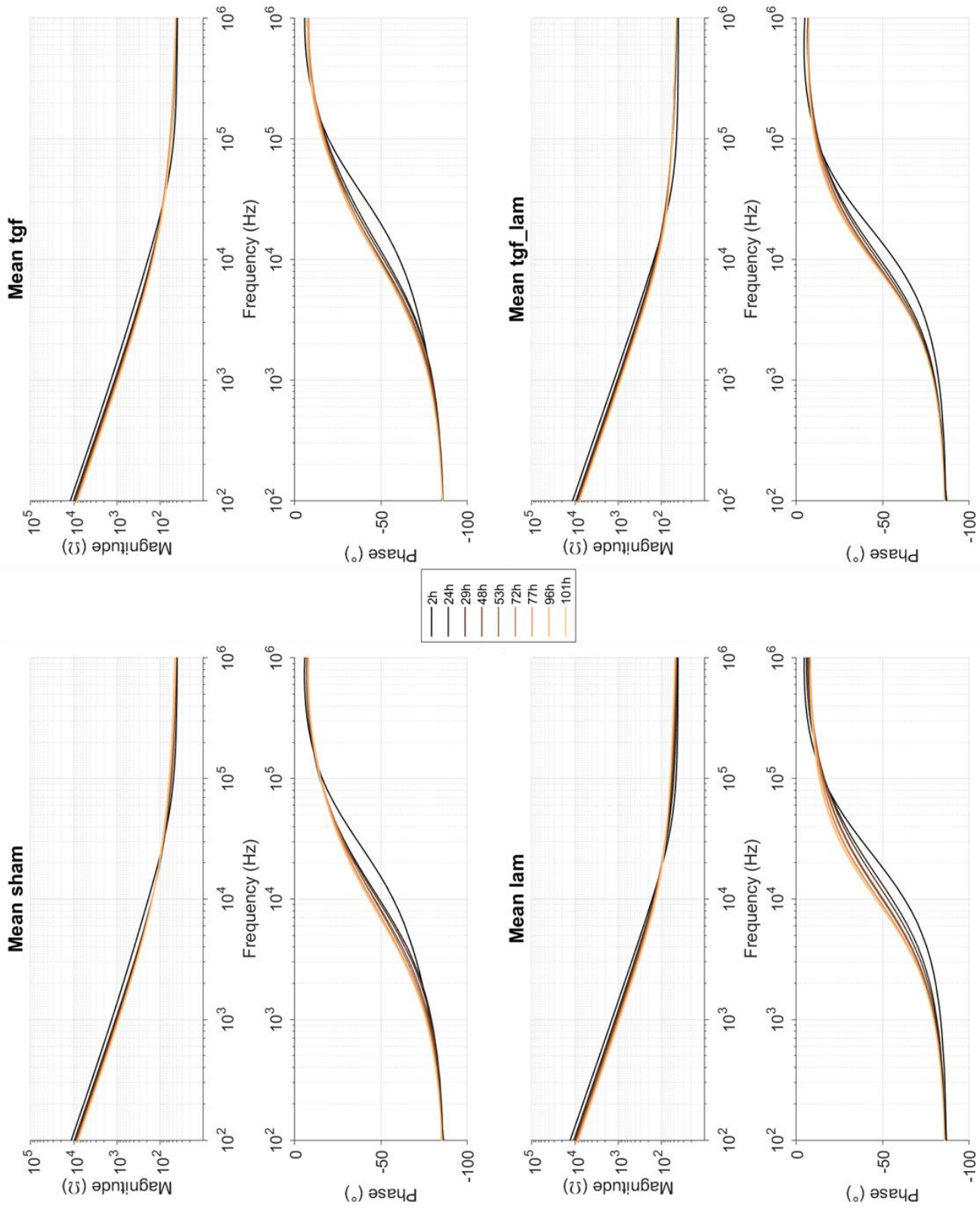


Figure 4-14: Magnitude and phase impedance spectra of each culturing condition for the different measuring times, the frequency range of the graphs is reduced to improve the readability of the measurements

#### 4.4.2.2. Characterization of the culture medium influence

As well as for the xCELLigence measurements in the paragraph 4.2.1, we wanted to know whether the different culturing conditions influenced the impedance measurements. To do that, we filled the wells with the four culturing mediums (sham, tgf, lam and lam\_tgf) without cells and measured the impedance three times over 120 hours. The results are presented on Figure 4-13.

We did not observe significant influence of the culture medium on the impedance spectra, as it was the case for the xCELLigence characterization. Having fully characterized the Solartron measurement bench, we now will present the results for the P3 experiment.

### 4.4.3. Results

Figure 4-14 represents the complete spectra and their evolution over the time. Four wells correspond to each condition and the presented plots result from the average magnitude and phase of these four samples. This global observation reveals modifications in the EIS spectrum along the time, for each culturing condition. There are many ways of highlighting these modifications; we could search for an optimal equivalent model for example or calculate relative differences at chosen frequencies. In this *in vitro* exploration, we chose to imitate the xCelligence approach but examining separately the contributions of the frequencies 10, 25 and 50 kHz.

In a first step, Figure 4-15 presents the evolution of the impedance magnitude for the three frequencies 10, 25 and 50 kHz over time.

First, we see that the trends are quite different depending on the frequency point: the impedance at 10 kHz decreases quasi-monotonously, the impedance at 50 kHz rather increases while the impedance at 25 kHz has an inflection between 25 h and 50 h. As we already observed in the CI curves presented in Figure 4-8, the sham and tgf conditions present a crossing around 40 h and such behaviour is absent from the lam and lam\_tgf impedance magnitudes. After 40 h, we notice that the sham and lam conditions have magnitude values higher than the tgf and lam\_tgf conditions respectively.

At 25 and 50 kHz, the magnitude values seems to have differences lower compared to the values at 10 kHz but we have to take care as their absolute values are quite different.

Thus, in a second step, we decided to compute, for each time point, the difference between the current value and the initial value (at  $t = 0$ ), as it is made for xCelligence CI evaluation (Equation 28). Furthermore this difference was also divided by the reference impedance respectively defined for 10 kHz, 25 kHz and 50 kHz. Doing like that, we calculated an impedance index specific to one frequency, that we call mono-frequency CI hereafter. The results are presented in Figure 4-16.

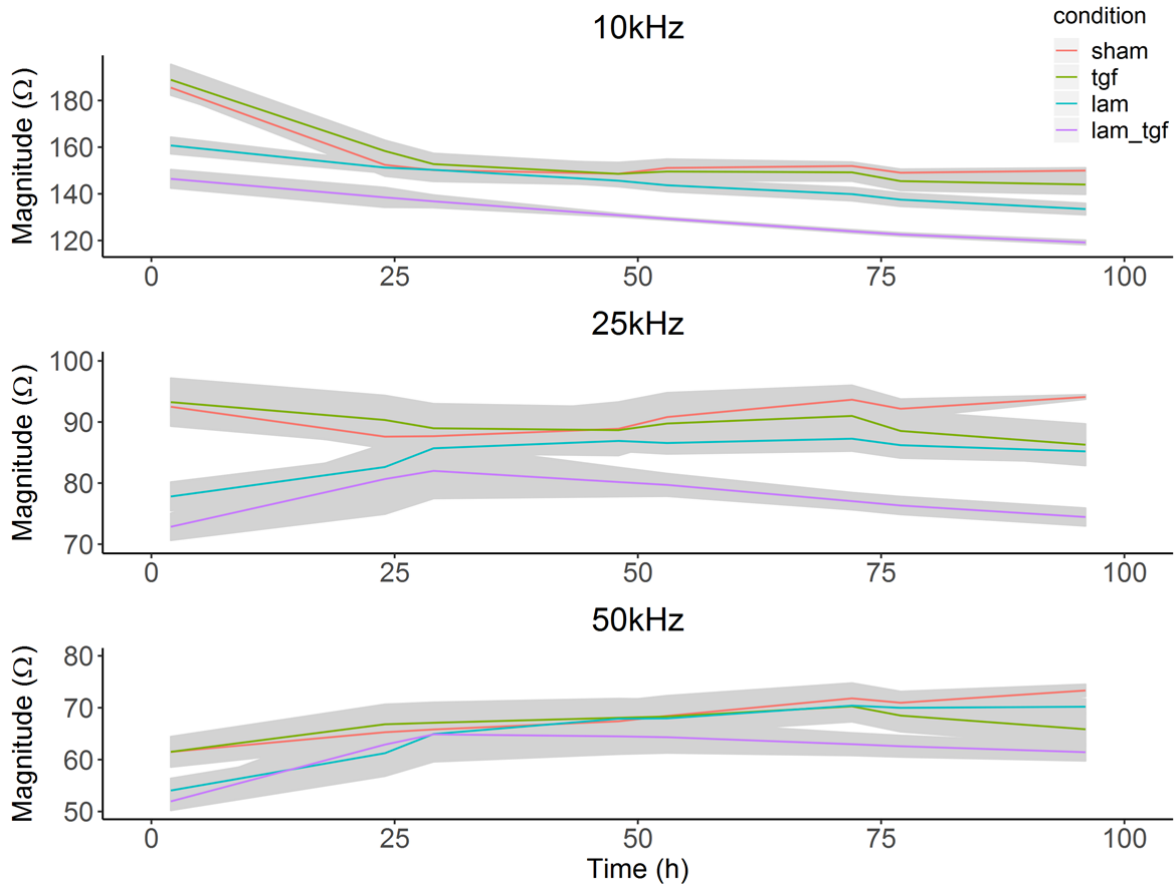


Figure 4-15: Impedance magnitude values (mean over 4 wells) at 10kHz, 25 kHz, and 50 kHz over time, the colour plot is the average value and the mean standard error is filled in grey.

As expected, the mono-frequency CI is negative for 10 kHz, due to the monotonous decrease of the impedance at this frequency; CI is positive at 25 and 50 kHz. The crossing for the sham and tgf conditions appears around 25 hours at 10 kHz, 35 hours at 25 kHz and 40 hours at 50 kHz.

At 10 kHz, the CI for sham and tgf conditions does not evolve a lot around 0, giving to this frequency point a poor interest to discriminate those conditions. At the contrary, the CI of wells containing laminin decrease a lot, to reach -1 for the lam condition and -2 for the lam\_tgf one. The laminin being an adhesion protein, its role in this interface region of the spectrum (10 kHz) is not surprising. Furthermore, for these laminin conditions, a net difference exists between wells with or without TGF- $\beta$ 1, suggesting that this growth factor also plays a role in the behaviour of the culture at the interface, from the first hours of the experiment.

Following our focus on wells containing laminin, at 25 kHz and 50 kHz, if the CI dynamics is globally different, at the end of the experiment, the presence or absence of TGF- $\beta$ 1 induces a difference in the CI of around 1, as for the CI at 10 kHz.

If we now focus on the conditions sham and tgf, frequencies 25 kHz and 50 kHz have a better potential to discriminate the culture evolution with or without TGF- $\beta$ 1. The 50 kHz frequency being almost in the resistive part of the spectrum, the observed difference can

certainly be attributed to a difference of conductivity between the *tgf* culture and the *sham* culture.

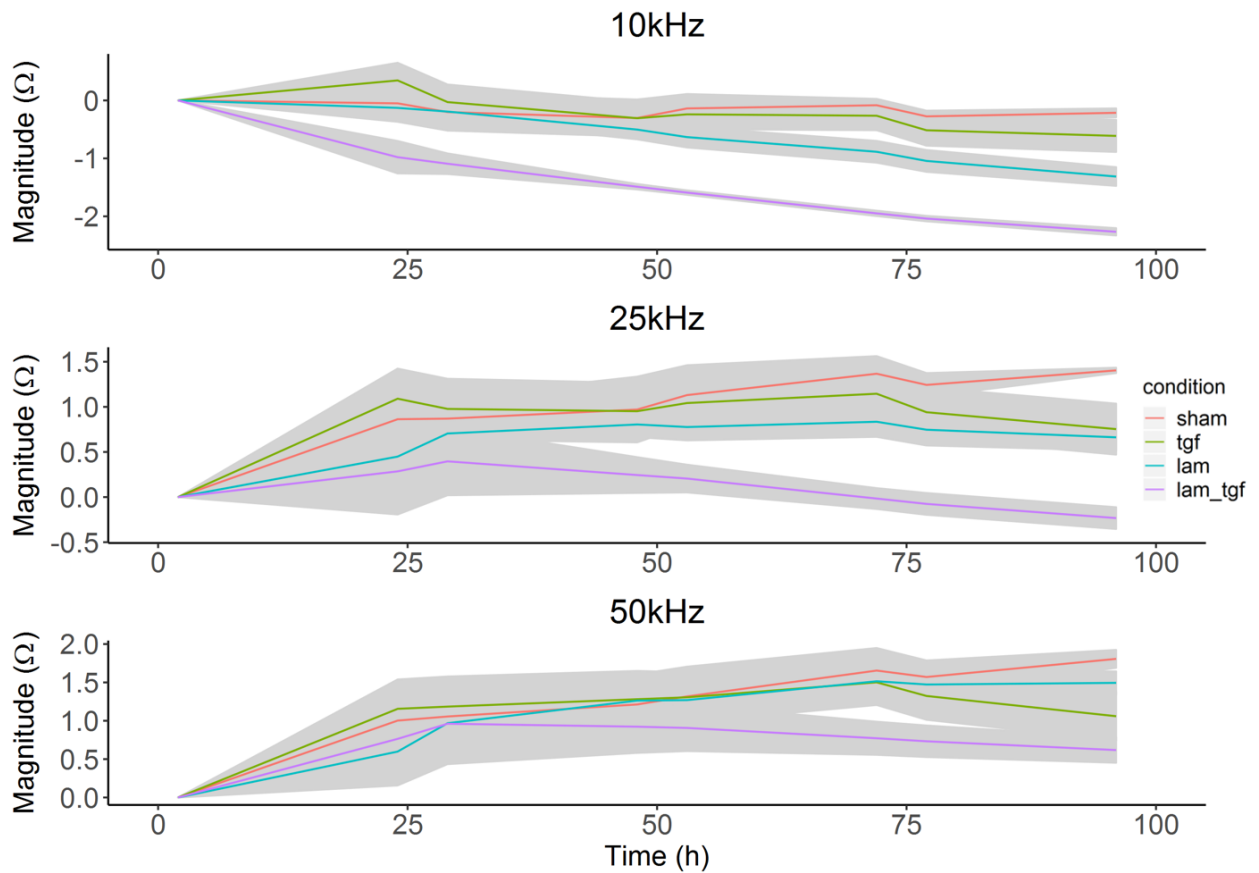


Figure 4-16: CI equivalence with the Solartron measurements for the measuring frequencies 10, 25 and 50 kHz

#### 4.4.4. Discussion

Separating the measuring frequencies and extracting a “mono-frequency” cell index allow to have more information about the culture. The modifications at the cells-electrodes interface can notably be separated from the modifications of the culture resistivity. Looking at this mono-frequency CI curves allows also to understand how they are combined in the xCelligence CI calculation: it is simply the sum of the 3 mono-frequency CIs, for each time point. At a consequence, the differences observed here between *lam* and *lam\_tgf* conditions are cancelled or those between *sham* and *tgf* conditions are emphasized in the xCelligence CI calculation. The xCelligence also CI favours the highest measuring frequency over the three combined frequencies because the coefficient  $Z$  by which we divide the difference of impedance magnitude is lower at higher frequencies (see Equation 28, where CI is maximised for higher frequencies).

Nevertheless, it is yet difficult to conclude as the analyzed data came only from P3 experiment. A complete analysis, including data from other sets of experiments (P4<sub>1</sub>, P4<sub>2</sub> and P5), would be necessary to perform a statistical analysis.

Once again, we can notice that these methods pay attention to the magnitude of the impedance only, whereas the behavior of the phase could bring a better sensitivity to our measurement, particularly in the transition region between the pseudo-capacitive part and the resistive part, precisely between 10 kHz and 50 kHz.

## 4.5. Conclusion

Our study addresses an unreported impedance-based method for real-time monitoring of the fibrogenic state of a CFs culture. Our simple biological model is based on the culture of human CFs, that were exposed or not to TGF- $\beta$ 1, used to accelerate their differentiation in MFs. We used the xCELLigence system, a commercial cellular assay platform used to monitor cell adhesion, proliferation and morphological changes, providing an impedimetric index, the so-called Cell Index (CI). A comparative analysis of the CI evolution along 6 days was performed in parallel to  $\alpha$ -SMA immunolabelling. The *in vitro* differentiation of fibroblasts into MFs was traceable by the CI over time, as well as the different events occurring in the culture wells. The CI of cultures exposed to TGF- $\beta$ 1 is always lower than the CI of the sham and lam cultures. These results are supported by a statistical analysis: the CI provides a significative signature of CFs differentiation in MFs. In the context of the research on anti-fibrotic therapies, our *in vitro* electrical signature could be a good candidate to test pharmacological agents.

To better understand the role of the frequency in cellular impedance measurements, we completed this *in vitro* exploration by EIS measurement on a wide frequency range with the Solartron 1260. Our preliminary analysis of the numerous spectral data led us to the definition of a mono-frequency CI that could be used to emphasize either the behaviour of the culture at the electrodes interface or modifications of the culture resistivity. For example, examination of the 10 kHz CI reveals a specific behaviour of the cultures containing laminin, a phenomenon that was masked in the xCelligence CI that sums contributions of three frequencies. In addition, the 25 kHz CI measurement could be enough to measure the degree of differentiation of the CFs in the cultures. These assertions must be confirmed by statistical analysis conducted on the whole characterization data that were collected in this PhD thesis, adding the spectroscopy data to passages P4<sub>1</sub>, P4<sub>2</sub> and P5. Nevertheless, the impedance spectra of cultures with TGF- $\beta$ 1 have always lower magnitude values than the impedance of the sham and lam cultures. These results are in accordance with our *ex vivo* results that presented lower impedance magnitudes for the collagenous tissues.

Finally, this cellular model itself has limits to represent the true process of fibrosis induced by implants. Exploration co-cultures of cardiac fibroblasts and cardiomyocytes could be a next step. Improving the *in vitro* approach is a way to better understand the fibrosis mechanism, identifying the roles of cellular or extracellular matrix components. Beside this, collecting data measured *in vivo* is an unavoidable step that requires the adaptation of the impedance measurement method: this is what we will discuss in the next chapter.



## CHAPTER V

# PRELIMINARY RESULTS TOWARDS *IN VIVO* EMBEDDED MEASUREMENTS

This chapter presents preliminary experiments that were carried out with the idea to address some constraints of chronic *in vivo* measurements. As studied in the previous chapters of this manuscript, the cardiac fibrosis evolution is a complex phenomenon and its modelling at the cellular level or static tissue level have both important limitations. These simplified models, however, made it possible to better understand the specifications of the impedance measurement and to evaluate its relevance for the characterization of fibrotic tissues. With the experiments exposed in this chapter, we explore two different axes of improvement: (1) the ability to implement the EIS in embedded electronic systems, first prototypes that could help in testing future implanted algorithms, and (2) the ability to conduct experiments on beating cardiac tissues.

- We will first present the adaptation of a custom integrated neuro-stimulator to perform impedance characterization using the multisine technique. As active implants naturally include a circuit that generates electrical excitation, we asked ourselves how this excitation source could be adapted to “broadband” impedance spectroscopy and what should be the sensing and post-processing strategy that allows accurate and low-consumption impedance measurement. The proof of concept of this method was performed with the monitoring of rat cardiac fibroblasts adhesion, in comparison with Solartron measurements.
- We will then present measurement results that were carried out with a custom FPGA-board developed by our collaborators of ETIS laboratory, implementing a technique based on the Orthogonal Frequency Division Multiplexing (OFDM) method. These measurements have been performed on cardiac tissues, both in cardioplegia as in the third chapter, and on reperfused tissues which represents another step towards *in vivo* measurements.

## 5.1. Multisine EIS evaluation on in vitro measurements

### 5.1.1. EIS measurement bench

#### 5.1.1.1. *Optimal excitation source*

An extensive study on broadband impedance spectroscopy using periodic excitations reported that the multisine signal was an optimal candidate [135]. In the time-domain, it has a minimal crest factor (CF), maximizing the signal to noise ratio (SNR) [136]. In the spectral domain, the frequency distribution can be optimized by using a bilateral quasi-logarithmic set (BQL), centred on the cut-off frequencies of the expected impedance

spectrum [136]. The previous *in vitro* experiments indeed pointed out the interest of the transition between pseudo-capacitive and resistive regions of the spectrum.

#### 5.1.1.2. *Material constraints*

- *Two-point electrode*

Our long-term objective being to add a monitoring functionality to *in vivo* cardiac pacing technologies, we are constrained to use a two-point impedance measurement technique, as human pacing/sensing leads are bipolar, with one proximal and one distal electrode, separated by few millimetres.

- *A neurostimulator as excitation source*

Typical excitation signal in neural electrical stimulation is a balanced biphasic current impulse, with a pulse width of tens of  $\mu\text{s}$  to tens of ms, with a repetition frequency reaching few hundreds of Hz at maximum [137]. In a previous PhD thesis, Jonathan Castelli developed a stimulation system, centered on a custom integrated circuit (IC) and controlled by a dedicated digital architecture implemented on an FPGA (Field Programmable Gate Array). It provides 8 stimulation channels with high-voltage compliance, to adapt to a wide range of experiments. Its real-time, open-loop and closed-loop capabilities have proven their efficacy in respiratory muscles stimulation experiments [138]. In the present study, we developed a second version of the digital architecture, in order to explore arbitrary stimulation waveforms, including adequate excitation for impedance measurement. Arbitrary waveforms are stored in binary format in a 32 bit-RAM and the FPGA architecture triggers the stimulation sequence of the 8 output channels, through an 8-bit, 1MSa/s DAC (Digital to Analog Converter). Each channel is a current source delivering 1 mA at maximum, with a 4  $\mu\text{A}$  resolution. Its measured static output resistance is of the  $\text{M}\Omega$  order. The characterization of the excitation source has been extended in a frequency domain ranging from few Hz up to 250 kHz, an interval exceeding largely the usual neurostimulation bandpass. We observed the proper operation of the current generation up to 100 kHz but a decrease in the output impedance at high frequencies, resulting in a 10% current error at 100 kHz for load impedance reaching 1 k $\Omega$ . This obliged us to add an interface circuit measuring the real current.

In the current version of the system, the minimal sampling period is 1  $\mu\text{s}$  and each channel can generate a unique tone, with a chosen amplitude and frequency. It limited the multi-tone exploration to 8 frequencies but allowed to conduct a feasibility study.

#### 5.1.1.3. *Sensing method and triggers management*

With a current-mode excitation source, the voltage drop across the electrode must be acquired. For this study, we used the Keysight MS0X2024A oscilloscope (200MHz, 2GSa/s, 8 bits). Despite this poor ADC resolution, the embedded post-processing uses oversampling and dithering methods that greatly improve the SNR (10 Effective Number of Bits). Oscilloscope time base is chosen to acquire five periods of the minimal frequency tone. Sampling frequency and vertical time scale are automatically adjusted. Triggering of stimulation and acquisition are controlled by a microcontroller (Atmel SAM3X8E, 32bits ARM-Cortex M3, on Arduino Due card), with a constant delay of 10 ns between the stimulation source and the acquisition. The microcontroller also controls the stimulus

duration and repetition. A MATLAB script drives every device and retrieves the current and voltage data, from a single interface.

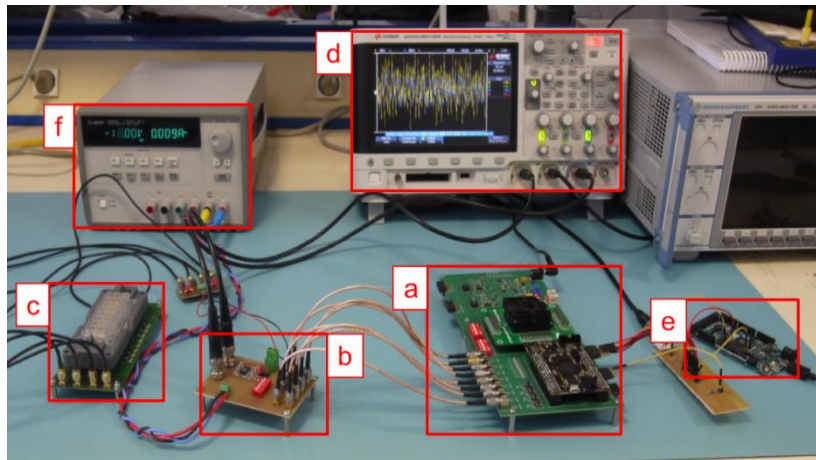


Figure 5-1: Photograph of the measurement bench. (a) Stimulation system, (b) Interface circuit for current sensing, (c) 16-well culture plate, (d) Oscilloscope, (e) Microcontroller, (f) Stimulator power supply

#### 5.1.1.4. Post-processing for impedance spectrum

Each acquisition set is post-processed following these steps: 7-term Blackman-Harris windowing, Discrete-Time Fourier Transform based on the known frequencies of the excitation signal, impedance spectrum computation. Furthermore, the variance of the results is calculated on a sequence of 5 successive acquisitions. Based on this statistical calculation, we estimate the SNR<sub>z</sub> of the impedance measurement [135], to evaluate the repeatability of measurement.

### 5.1.2. Proof of concept on in vitro impedance measurement

Cardiac fibroblasts were isolated from neonatal Sprague-Dawley rats (Charles River, France) and cultured in xCELLigence E-Plate 16 (Ozyme, France) at 75000 cells per well. These plates contained 16 culture wells with golden electrodes at the bottom which interdigitated electrodes allowing 2-point impedance measurements. Cells were maintained at 37°C, 5% CO<sub>2</sub> and 95% humidity during the measurements. First, a reference measurement was made with Solartron 1260 (Ametek, USA), at 100 mV, on the 1Hz-1MHz frequency range, which was used to generate the proper BQL distribution of the frequency points, from 5 kHz to 100 kHz. The duration of the multisine signal is 5 ms, corresponding to 5 periods of the minimal sinus frequency. The results are presented in Figure 5-2.

In Figure 5-2 the frequency components of the multisine signal are represented by stars (\*) and we can observe their distribution around the transition region of the spectrum. First, the multisine measure is highly repeatable as SNR<sub>z</sub> is always higher than 72 dB. For each of the 16 wells, the custom multisine spectrum reproduces the Solartron reference spectrum with a maximal relative error of 3% for the magnitude and 5% for the phase.

The cellular preparation has been submitted to the excitation signal during only 5 ms, as the post-processing were performed off-line after the immediate acquisition of the voltage. This technique of rapid broadband spectroscopy is compliant with the conditions of *in vivo* beating tissues as 5 ms correspond to a quasi-instantaneous measurement compared to the heartbeat period. This measurement could even be synchronized to a given point of the cardiac cycle.

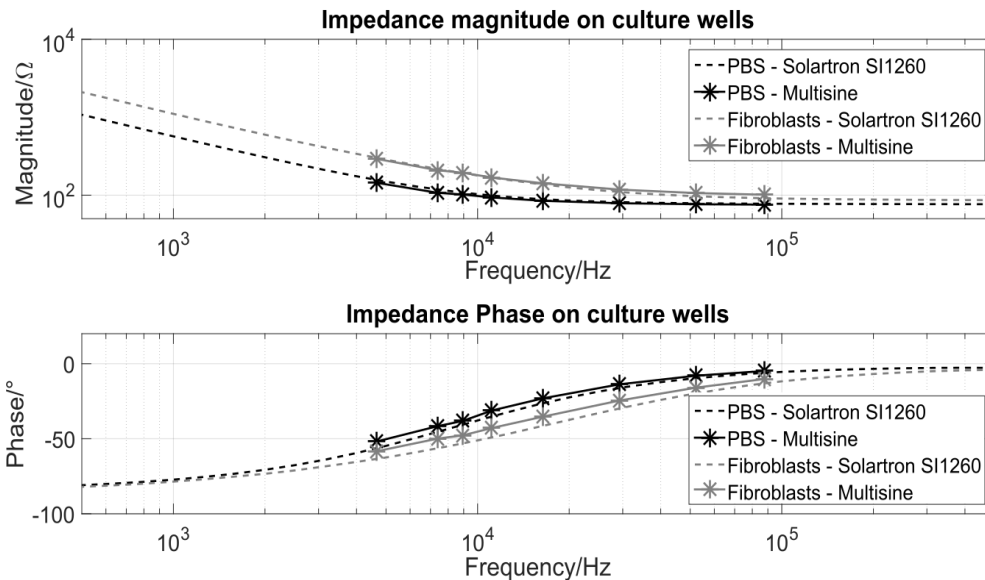


Figure 5-2: Impedance magnitude and phase graphs for one well at day 7 of fibroblasts culture

## 5.2. Orthogonal Multitone EIS (OMEIS) applied to cardiac tissues

### 5.2.1. EIS measurement bench

This part was operated in collaboration with Dr. Edwin De Roux and Pr. Olivier Romain, from the ETIS lab at Cergy-Pontoise.

The OFDM (Orthogonal Frequency Division Multiplexing) is a technique well-known and successfully used in the field of digital communications. This technique has been adapted here to embedded EIS for rapid impedance estimation in the frequency bandwidth of interest. The generation of a multi-tone signal is one of the primary tasks in implementing an OFDM transceiver system [139]. This method allows controlling the

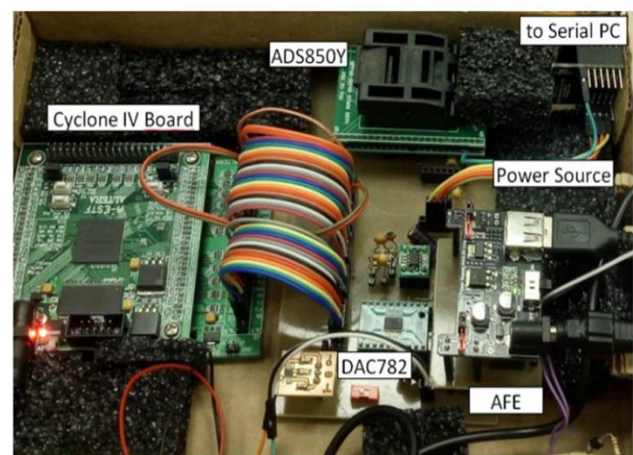


Figure 5-3: The OMEIS system board, extracted from De Roux *et al.*, 2019

spectrum of the multitone signal with great flexibility by defining the values of the OFDM symbols, the use of an appropriate modulation scheme and/or the manipulation of the system parameters, such as the sampling frequency. Compared to the simple multisine technique, the OFDM method requires less memory for the implementation of the signal generator. This new approach is called hereafter the Orthogonal Multitone Electrical Impedance Spectroscopy (OMEIS).

A photography of the OMEIS system board is presented in Figure 5-3. It has a parallel input 12 bits DAC converter (DAC7821), a parallel output 14 bits ADC (ADS850Y) and an Analog Front End (AFE) board, as depicted in Figure 5-3. This AFE board has maximum stimulation voltage amplitude of 200 mV. The AFE also filters non-desired DC and 50/60 Hz components from the multi-tone signal. The stimulation signal is in voltage mode and the resulted current is captured and converted into voltage via a Transimpedance Amplifier (TIA) in which the values of a feedback resistor is set during calibration. Both emitter and receiver blocks are implemented in a Cyclone IV FPGA device programmed in VHDL language. Both the calibration and the measured data are stored in a 256 Mb SDRAM (W9825G6EH). Then they are sent via SPI to a PC. The PC runs a Human-Machine Interface (HMI), coded in Matlab, for the control of the system as well as for the analysis of the data.

The OMEIS flexibility and reliability during impedance measurements had already been proven for *in vitro* experiments [140]. The objective in this part is the evaluation of the OMEIS ability for *in vivo* conditions.

### 5.2.2. Proof of concept on cardiac tissues impedance measurements

The following experiments were conducted on *ex vivo* cardiac tissues as in the third chapter, using the same commercial electrode SprintQuattro and on reperfused cardiac tissues that mimic *in vivo* conditions. This study was carried out in accordance with the recommendations of the Directive 2010/63/EU of the European Parliament on the protection of animals used for scientific purposes and approved by the local ethical committee of Bordeaux CEEA50. The heart was obtained from young swine, (Large White, 40±5 kg), premedicated with ketamine (20 mg/kg) and acepromazine (Calmivet, 1mL/50kg). Anaesthesia was induced with intravenous injection of sodium pentobarbital (10 mg/kg) and maintained under isoflurane, 2%, in 100% O<sub>2</sub>. The swine was euthanized by sodium pentobarbital (40 mL, from 50 mg/mL of stock) and the heart rapidly excised, cannulated by the aorta, and rinsed with cold cardioplegic solution, containing (mM): NaCl, 110; CaCl<sub>2</sub>, 1.2; KCl, 16; MgCl<sub>2</sub>, 16; NaHCO<sub>3</sub>, 10; and glucose, 9.01 at 4°C.

### 5.2.2.1. Static tissues in cardioplegia

As already described in paragraph 3.1.1, the left ventricle (LV) wall was dissected and placed in the cardioplegic solution. It was conserved on ice for the whole duration of the experiment. The measured zones were also the same, noted as '**Muscle**' for the healthy region and '**Collagen**' for the collagenous one (see Figure 3-1).

The OMEIS system was configured with an IFFT/FFT (Inverse Fast Fourier Transform/Fast Fourier Transform) of size  $N = 1024$ , 32 symbols and a sampling frequency  $F_s$  of 1 MHz [140]. We used the Solartron 1260 impedance-meter to have reference measurements. With the Solartron, the measurements were done at a 100 mV peak voltage (similar to the OMEIS system), with a logarithmic frequency sweep from 1 Hz to 1 MHz with 10 points per decade. For OMEIS, each measurement was carried out once, for the Solartron, they were repeated five times and the mean of these measurements is calculated. The results are presented in Figure 5-4 (extracted from [140]).

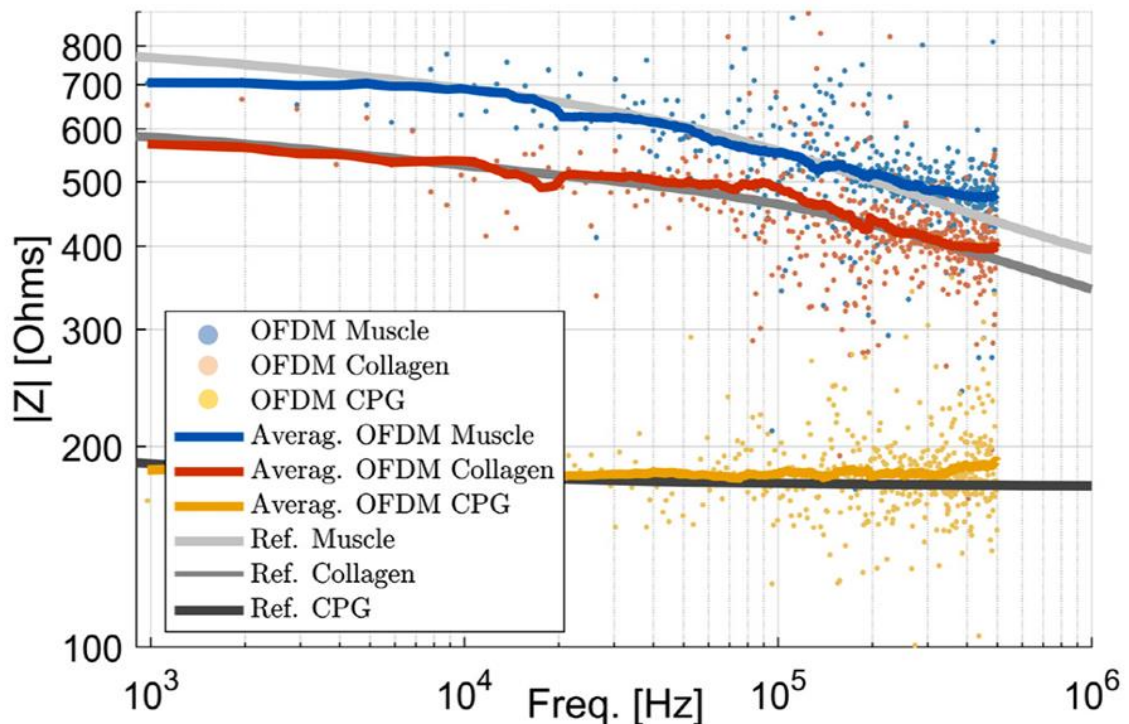


Figure 5-4: Impedance magnitude measurements for 3 conditions: 'Muscle', 'Collagen' and 'CPG' the reference condition in cardioplegia. OFDM is performed at  $F_s = 1\text{MHz}$ . Colored curves represent OMEIS measurements, grey ones represent Solartron measurements.

The Figure 5-4 illustrates the comparison between Solartron and OMEIS impedance measurements. It can be noticed that 'Muscle' condition has the greatest impedance magnitude, followed by the 'Collagen' condition and lastly the 'CPG' solution that has much lower impedance magnitude of around  $190\ \Omega$ . These results are in accordance with those we presented in paragraph 3.2.1. The values of the OMEIS system were noisy since a reduced number of symbols ( $M = 32$ ) was used, in order to increase measurement speed. However, the averaged version follows very closely the values of the reference instrument

with a mean error of about 8% and a standard deviation of 5.8%. The duration of the excitation was of few ms.

#### 5.2.2.2. Perfused tissues

The LV was dissected and cannulated by the left anterior descending artery. Then the LV was mounted on to a frame where it is submerged and perfused (20ml/min) with a warm (37°C) saline solution containing (in mM): NaCl,130; NaHCO<sub>3</sub>, 24; NH<sub>2</sub>PO<sub>4</sub>, 1.2; MgCl<sub>2</sub>, 1; glucose, 5.6; KCl, 4; CaCl<sub>2</sub>, 1.8; gassed with 95% O<sub>2</sub>/5% CO<sub>2</sub> (pH 7.4). A volume-conducted ECG was measured in the bath to monitor the electrical activity of the tissue preparation. The perfusion system is called the Langendorff system and is showed on Figure 5-5.

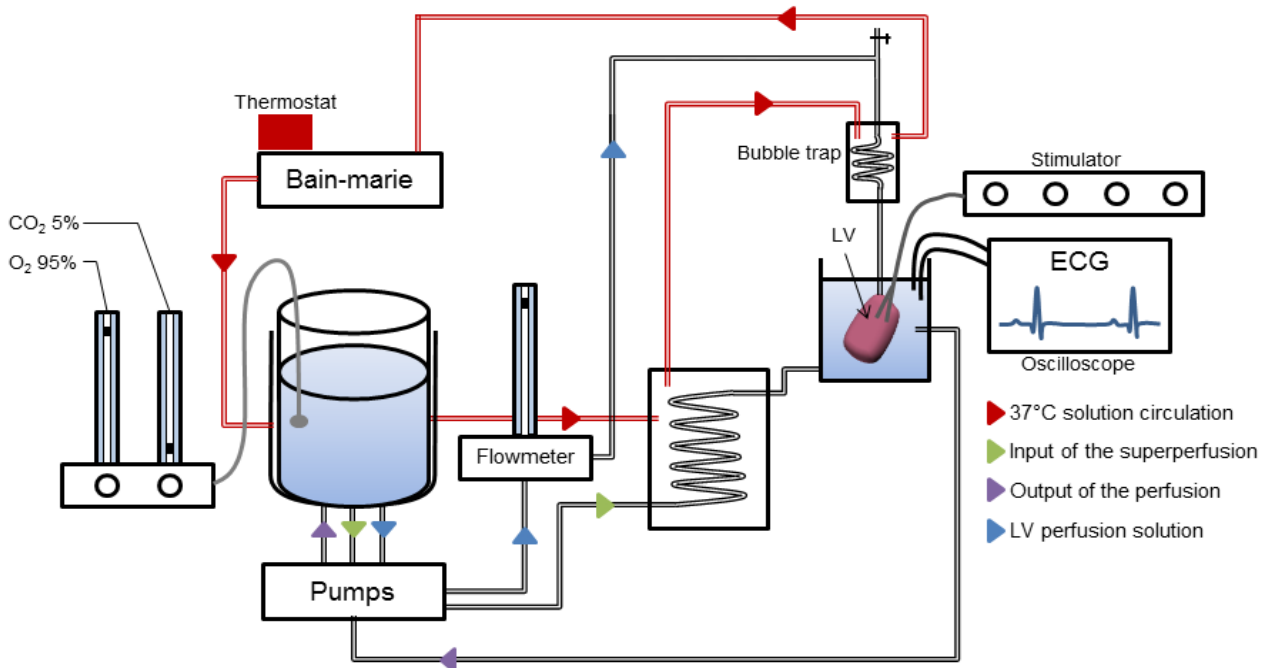


Figure 5-5: Langendorff system maintaining the ventricle in *in vivo* conditions. A picture of the ventricle in the perfusion chamber is shown on the right.

In these experimental conditions, the LV is capable of regular contractions mimicking the *in vivo* heart beating. During this experimentation, only the OMEIS system was used for the impedance measurements. The Solartron uses a frequency sweep EIS method which results in measurements of several minutes and makes it incompatible with these experimental conditions.

Figure 5-6 (extracted from [140]) shows the impedance values received from the OMEIS for the perfused LV, for 'Muscle' and 'Collagen' conditions. It can be noticed that again the 'Muscle' condition has a greater impedance than the 'Collagen' condition, although both have lower values than those obtained in the cardioplegia experience presented in the previous paragraph 5.2.2.1. Experimental conditions differ indeed largely, especially in temperature and also in the fact that both the ventricle and the electrode were completely submerged in the saline solution.

Furthermore, in the first experiment, the ventricle was immobilized and the measuring poles of the SprintQuattro lead were both in contact with the tissue, where in the second experiment, the distal electrode is no more in contact with the tissue as it is immersed and exhibits regular contractions. However, with the impedance measurement, the differentiation between both tissues impossible, even with the dynamic of the heart imposed by the perfusion system.

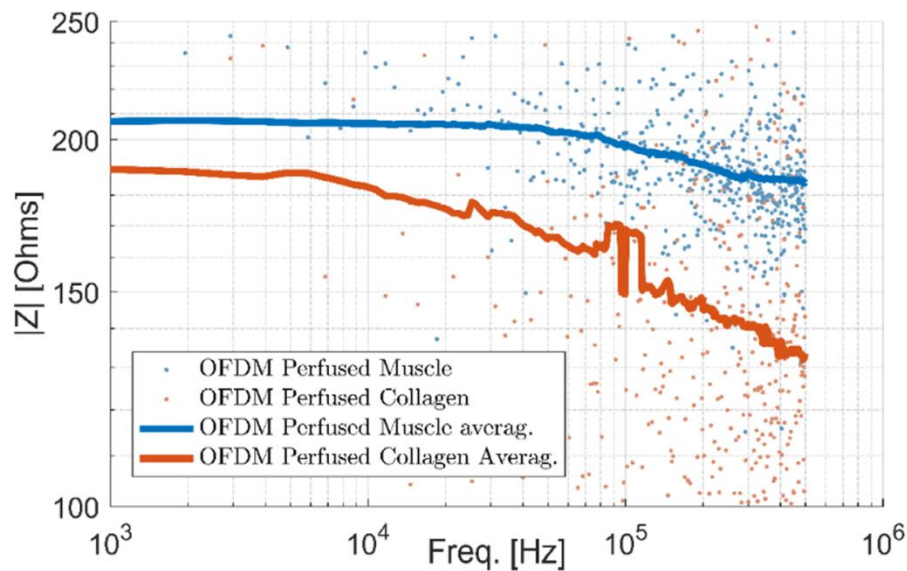


Figure 5-6: Impedance magnitude of 'Muscle' and 'Collagen' conditions for the ventricle reperfused, measured by the OMEIS system at  $F_s = 1\text{MHz}$ .

### 5.3. Conclusion

This last chapter has presented preliminary EIS experiments conducted on cardiac cells or tissues using fast broadband algorithms. These algorithms have been implemented on custom electronic systems that were developed at IMS or ETIS laboratories; they are based on the generation of multi-tone excitation signals with two different methods. The technical aspects of the embedded signal processing were not in the focus of this thesis, that is why they were briefly developed here. The main motivation of this chapter was to confront the EIS cardiac tissue characterization to severe experimental conditions, close to the *in vivo* ones, as the implant-induced fibrosis is a complex and long-term phenomenon. Finally, the results prove that it is feasible to distinguish both tissue natures using EIS and highlight the key specifications of a broadband algorithm.

# CONCLUSION

This manuscript summarizes three years of research on an innovative study of the implant-induced cardiac fibrosis. With this work, we wanted to answer the following question: does the fibrosis developing around the cardiac leads have an electrical signature? We fulfilled this exploration along three research axes. We first used electrical impedance spectroscopy to discriminate a healthy from a collagenous cardiac tissue, and modelled the results using two approaches, to have a better understanding of the mechanisms that influence the tissue or interface conductivity, from a macroscopic to a microscopic scale. Then we developed an *in vitro* fibrosis model culturing cardiac fibroblasts and monitoring their controlled differentiation into myofibroblasts both electrically and biologically. A third axis was briefly described, considering embedded measurements using broadband signals with custom stimulators.

## Synthesis

**Chapter I:** This first chapter introduced the societal, medical and scientific context of this thesis. It presented the function of the cardiac muscle and how the different cardiac arrhythmias originated. It also reminded the historical development of the electrical therapies used to treat these different arrhythmias and presented the current implants used in the patients. It finally pointed out the biocompatibility challenge for the cardiac leads and electrodes and introduced the issue of fibrotic tissue developing around them. This issue could be exacerbated in case of the most recent leadless nano-pacemakers or multi-electrode resynchronisation devices. With this chapter, we emphasized this work's multidisciplinary that requires the understanding of the biological mechanisms of fibrosis, as well as the impedance characterization technique applied in the cardiac field.

**Chapter II:** The second chapter sets up the state of the art of both the cardiac fibrosis development and the bioimpedance characterization. It began with an overview of cardiac fibroblasts and myofibroblasts, cellular components playing a major role in fibrosis development. Then it introduced the different steps of the foreign body response happening at the implantation of a cardiac lead, emphasizing the tissue remodelling and its consequences. In a second part, it synthesized the theory of electrical impedance of biological material, presenting the different physical phenomena that characterize the charges movement mechanisms involved in impedance measurements. It discussed the electrical modelling of the electrode-tissue interface and of the tissue impedances, leading us to understand that a global biophysical model could help to understand our impedance measurements. Finally, it addressed the different measurement techniques and the application fields of bioimpedance characterization. It ended with our motivation for this work, highlighting that the cardiac fibrosis should have a signature on the impedance spectrum and describing our experimental approach that implements biological models of different scales.

**Chapter III:** This chapter presented the results of the experiments performed *ex vivo*. We characterized two tissue conditions, 'Healthy' and 'Collagen', on a wide frequency range, searching a difference between the healthy and the collagenous tissues on the impedance spectra. This simplified fibrosis model allowed us to implement a method of impedance

characterization using human cardiac probes. A difference on the measurements appeared between 10 Hz and 1 MHz depending on the tissue condition. The modelling allowed us to quantitatively study these differences. We noticed that the 'Collagen' region had a lower impedance value than the 'Healthy' one. Two models were tested; a biophysical one and a mathematical one, and the results indicated that the first model enabled a more direct interpretation regarding tissue or interface properties. The better tissue discrimination markers appeared to be in the 10 kHz-1 MHz frequency range, through model parameters that accounts for the  $\beta$  tissue dispersion, or by a single frequency phase measurement in this range.

**Chapter IV:** The fourth chapter detailed the results obtained on the *in vitro* cardiac fibrosis model, based on the culture of human cardiac fibroblasts exposed to a growth factor (TGF- $\beta$ 1) inducing their differentiation into myofibroblasts. It addressed an impedance-based method for real-time monitoring of *in vitro* fibrosis evolution using the xCELLigence instrument (provides an impedimetric index (CI) tracking cell adhesion, proliferation and morphological changes) for the electrical characterization. We performed in parallel a biological characterization with immunocytochemistry. The CI of cultures exposed to TGF- $\beta$ 1 was always lower than the culture without TGF- $\beta$ 1, and this was confirmed by the statistical analysis performed on the data. A deeper frequency exploration was achieved using the Solartron 1260 impedancemeter, and again, the cultures exposed to TGF- $\beta$ 1 presented lower impedance values than the cultures without TGF- $\beta$ 1. This finer frequency exploration also revealed properties of the electrodes-cell interface that were masked in the xCelligence CI calculation. Finally, the decrease in the CI of cultures having more differentiated myofibroblasts is consistent with the *ex vivo* experiments that characterized a decrease in impedance for collagenous tissues.

**Chapter V:** The last chapter of this manuscript presented the exploration of impedance embedded measurements using custom circuits. Preliminary EIS experiments were conducted on cardiac cells or tissues using fast broadband impedance spectroscopy. *In vitro* characterization was used as a proof-of-concept where a multisine excitation signal was generated with an IMS-custom stimulator. A second portable system, developed by our ETIS partners, and that carried out an algorithm originally used in digital telecommunication, was also successfully tested. We finally wanted to confront the EIS cardiac tissue characterization to more severe experimental conditions, closer to the *in vivo* ones, as the implant-induced fibrosis is a complex and long-term phenomenon. The results proved that it is feasible to identify the tissue nature using EIS and highlight the key specifications of a broadband algorithm.

## Perspectives

These preliminary results on the cardiac fibrosis characterization using impedance spectroscopy open different perspectives for the future research work in the team.

At the cellular level, a deeper biological exploration could bring additional information, especially developing co-cultures of cardiac fibroblasts and cardiomyocytes [141]. This would allow us to complete the fibrosis model and to go forward in the understanding of the cellular mechanism during the fibrosis development. For further analysis, it has been recently proven that the myofibroblasts have reversible properties to go back to the

fibroblasts phenotype [132], our characterization technique would make a good candidate to test pharmacological compounds targeting fibrotic metabolic endpoints [117], [142].

At the tissue level, different aspects can be further explored. First of all, the proportion of tissue scanned with our impedance characterization is only a certain percentage of all the fibrotic encapsulation occurring along the lead. Indeed, over the years, the lead is totally wrapped with fibrotic tissue, creating strong adherences in the cardiac cavities and also in the venous region. In our work we perform a macroscopic empirical analysis of the tissue present between the proximal and distal electrodes. One possibility is to simulate, with dedicated finite elements algorithms, the current lines in the tissue between these two measuring electrodes, to have an estimation of the quantity of tissue analysed. This could open a discussion about the signal energy necessary to go through the fibrotic tissue to the electrically active myocardium. Furthermore, with a growing fibrotic tissue, the distance between the stimulating electrode and the treated healthy myocardium region grows over time. This could be an explanation to the need of stimulation threshold increase with the years of implantation.

Then, an exploration in higher frequencies could allow us to improve the modelling work already perform. We would be able to better estimate the  $\beta$  and  $f_{\beta}$  parameters regarding the tissue condition.

Finally, conducting *in vivo* and chronic measurements (over few months), using broadband signals, could help us taking a step forward to the understanding of the fibrosis development at the electrode interface, but also to have a better overview of the conditions of *in vivo* measurements (beating cardiac muscle, blood flow).



# BIBLIOGRAPHY

- [1] R. Zak, "Development and proliferative capacity of cardiac muscle cells," *Circ. Res.*, vol. 35, no. 2, pp. II-17-II-26, 1974.
- [2] A. Nag, "Study of non-muscle cells of the adult mammalian heart: a fine structural analysis and distribution," *Cytobios*, vol. 28, no. 109, pp. 41–61, 1980.
- [3] Y. Rudy, "Molecular basis of cardiac action potential repolarization," *Ann. N. Y. Acad. Sci.*, vol. 1123, pp. 113–118, 2008.
- [4] F. Pettersen, "Bioimpedance as a tool in cardiac resynchronisation therapy," University of Oslo, 2017.
- [5] M. N. Levy and A. J. Pappano, *Cardiovascular physiology*. Mosby, 2007.
- [6] F. KAVALER, V. J. FISHER, and J. H. STUCKEY, "The Potentiated Contraction and Ventricular 'Contractility'." *Bull. N. Y. Acad. Med.*, vol. 41, pp. 592–601, 1965.
- [7] A. G. KLÉBER and Y. RUDY, "Basic Mechanisms of Cardiac Impulse Propagation and Associated Arrhythmias," *Physiol. Rev.*, vol. 84, no. 2, pp. 431–488, 2004.
- [8] J. M. T. De Bakker *et al.*, "Slow conduction in the infarcted human heart: 'Zigzag' course of activation," *Circulation*, vol. 88, no. 3, pp. 915–926, 1993.
- [9] M. J. Janse and A. L. Wit, "Electrophysiological mechanisms of ventricular arrhythmias resulting from myocardial ischemia and infarction," *Am. Physiol. J.*, vol. 69, no. 4, pp. 1049–1168, 1989.
- [10] A. de Micheli-Serra, P. Iturralde-Torres, and R. Izaguirre-Ávila, "How electricity was discovered and how it is related to cardiology," *Arch. Cardiol. México*, vol. 82, no. 3, pp. 252–259, 2012.
- [11] M. Cobb, "Exorcizing the animal spirits: Jan Swammerdam on nerve function," *Nat. Rev. Neurosci.*, vol. 3, no. 5, pp. 395–400, 2002.
- [12] L. Galvani and G. Aldini, *De Viribus Electricitatis In Motu Musculari Comentarium Cum Joannis Aldini Dissertatione Et Notis; Accesserunt Epistolae Ad Animalis Electricitatis Theoriam Pertinentes*, Apud Socie. 1792.
- [13] A. Volta, "On the electricity excited by the mere contact of conducting substances of different kinds," *Philos. Trans. R. Soc. London*, pp. 403–431, 1800.
- [14] K. Jelved, A. D. Jackson, and O. Knudsen, *Selected Scientific Work of Hans Christian Orsted*. Princeton University Press, 2014.
- [15] S. Grimnes and Ø. G. Martinsen, *Bioimpedance and Bioelectricity Basics*, Elsevier. 2015.
- [16] C. Matteucci, "Sur le courant électrique de la grenouille : second mémoire sur l'électricité animale faisant suite à celui sur la torpille," *Ann Chim Phys*, vol. 6:301, 1842.
- [17] A. D. Waller, "A demonstration on man of electromotive changes accompanying the heart's beat," *J. Physiol.*, 1887.
- [18] A. D. Waller and W. Reid, "On the action of the excised mammalian heart," *Philos. Trans. R. Soc. B*, pp. 215–256, 1887.

- [19] W. Einthoven, "The string galvanometer and the human electrocardiogram," *R. Netherlands Acad. Arts Sci. Proc.*, vol. 6, no. September, pp. 107–115.
- [20] W. Einthoven, G. Fahr, and A. de Waart, "On the direction and manifest size of the variations of potential in the human heart and on the influence of the position of the heart on the form of the electrocardiogram," *Am. Heart J.*, vol. 40, no. 2, pp. 163–211, 1950.
- [21] P. M. Zoll, A. J. Linenthal, W. Gibson, M. H. Paul, and L. R. Norman, "Termination of ventricular fibrillation in man by externally applied electric countershock," *N. Engl. J. Med.*, vol. 254, no. 16, pp. 727–732, 1956.
- [22] O. Aquilina, "A brief history of cardiac pacing," *Images Paediatr. Cardiol.*, vol. 8, no. 2, pp. 17–81, 2006.
- [23] C. W. Lillehei, V. L. Gott, P. C. Hodges, D. M. Long, and E. E. Bakken, "Transistor pacemaker for treatment of complete atrioventricular dissociation," *J. Am. Med. Assoc.*, vol. 172, no. 18, pp. 76–80, 1960.
- [24] R. Elmqvist and A. Senning, "An implantable pacemaker for the heart," *Med. Electron. Proc. Second Int. Conf. Med. Electron.*, pp. 253–254, 1959.
- [25] H. G. Mond, J. R. Helland, K. Stokes, G. A. Bornzin, and R. McVenes, "The electrode-tissue interface: The revolutionary role of steroid-elution," *PACE - Pacing Clin. Electrophysiol.*, vol. 37, no. 9, pp. 1232–1249, 2014.
- [26] A. Kypta *et al.*, "First Autopsy Description of Changes 1 Year After Implantation of a Leadless Cardiac Pacemaker: Unexpected Ingrowth and Severe Chronic Inflammation," *Can. J. Cardiol.*, vol. 32, no. 12, pp. 1578.e1-1578.e2, 2016.
- [27] V. Y. Reddy *et al.*, "Retrieval of the Leadless Cardiac Pacemaker: A Multicenter Experience," *Circ. Arrhythmia Electrophysiol.*, vol. 9, no. 12, pp. 1–6, 2016.
- [28] J. M. Morais, F. Papadimitrakopoulos, and D. J. Burgess, "Biomaterials/tissue interactions: Possible solutions to overcome foreign body response," *AAPS J.*, vol. 12, no. 2, pp. 188–196, 2010.
- [29] C. A. Souders, S. L. K. Bowers, and T. A. Baudino, "Cardiac fibroblast: The renaissance cell," *Circ. Res.*, vol. 105, no. 12, pp. 1164–1176, 2009.
- [30] P. Camelliti, T. K. Borg, and P. Kohl, "Structural and functional characterisation of cardiac fibroblasts," *Cardiovasc. Res.*, vol. 65, no. 1, pp. 40–51, 2005.
- [31] G. Krenning, E. M. Zeisberg, and R. Kalluri, "The origin of fibroblasts and mechanism of cardiac fibrosis," *J. Cell. Physiol.*, vol. 225, no. 3, pp. 631–7, 2010.
- [32] T. A. Baudino, W. Carver, W. Giles, and T. K. Borg, "Cardiac fibroblasts: friend or foe?," *Am. J. Physiol. Circ. Physiol.*, vol. 291, no. 3, pp. H1015–H1026, 2006.
- [33] R. S. Smith, T. J. Smith, T. M. Blieden, and R. P. Phipps, "Fibroblasts as sentinel cells. Synthesis of chemokines and regulation of inflammation," *Am. J. Pathol.*, vol. 151, no. 2, pp. 317–22, 1997.
- [34] M. J. Ivey and M. D. Tallquist, "Defining the Cardiac Fibroblast," *Circ. J.*, vol. 80, no. 11, pp. 2269–2276, 2016.
- [35] J. G. Travers, F. A. Kamal, J. Robbins, K. E. Yutzey, and B. C. Blaxall, "Cardiac fibrosis: The fibroblast awakens," *Circ. Res.*, vol. 118, no. 6, pp. 1021–1040, 2016.

- [36] R. T. Kendall and C. A. Feghali-Bostwick, "Fibroblasts in fibrosis: Novel roles and mediators," *Front. Pharmacol.*, vol. 5 MAY, no. May, pp. 1–14, 2014.
- [37] J. Baum and H. S. Duffy, "Fibroblasts and Myofibroblasts: What Are We Talking About?," *J. Cardiovasc. Pharmacol.*, vol. 57, no. 4, pp. 376–379, 2011.
- [38] F. A. Van Nieuwenhoven and N. A. Turner, "The Role of Cardiac Fibroblasts in the Transition from Inflammation to Fibrosis Following Myocardial Infarction," *Vascul. Pharmacol.*, vol. 58, no. 3, pp. 182–188, 2013.
- [39] J. D. Lajiness and S. J. Conway, "The dynamic role of cardiac fibroblasts in development and disease," *J. Cardiovasc. Transl. Res.*, vol. 5, no. 6, pp. 739–748, 2012.
- [40] S. Chacar, N. Farès, P. Bois, and J. F. Faivre, "Basic Signaling in Cardiac Fibroblasts," *J. Cell. Physiol.*, vol. 232, no. 4, pp. 725–730, 2017.
- [41] D. MacKenna, S. R. Summerour, and F. J. Villarreal, "Role of mechanical factors in modulating cardiac fibroblast function and extracellular matrix synthesis," *Cardiovasc. Res.*, vol. 46, no. 2, pp. 257–263, 2000.
- [42] E. C. Goldsmith *et al.*, "Organization of fibroblasts in the heart," *Dev. Dyn.*, vol. 230, no. 4, pp. 787–794, 2004.
- [43] K. E. Porter and N. A. Turner, "Cardiac fibroblasts: At the heart of myocardial remodeling," *Pharmacol. Ther.*, vol. 123, no. 2, pp. 255–278, 2009.
- [44] E. Ongstad and P. Kohl, "Fibroblast-Myocyte Coupling in the Heart: Potential Relevance for Therapeutic Interventions," *J. Mol. Cell. Cardiol.*, vol. 91, pp. 238–246, 2016.
- [45] P. Kohl and P. Camelliti, "Fibroblast-myocyte connections in the heart," *Hear. Rhythm*, vol. 9, no. 3, pp. 461–464, 2012.
- [46] W. Chen and N. G. Frangogiannis, "Fibroblasts in post-infarction inflammation and cardiac repair," *Biochim. Biophys. Acta - Mol. Cell Res.*, vol. 1833, no. 4, pp. 945–953, 2013.
- [47] M. Kawaguchi *et al.*, "Inflammasome activation of cardiac fibroblasts is essential for myocardial ischemia/reperfusion injury," *Circulation*, vol. 123, no. 6, pp. 594–604, 2011.
- [48] S. van Putten, Y. Shafieyan, and B. Hinz, "Mechanical control of cardiac myofibroblasts," vol. 93, pp. 133–142, 2015.
- [49] I. A. Darby, B. Laverdet, F. Bonté, and A. Desmoulière, "Fibroblasts and myofibroblasts in wound healing," *Clin. Cosmet. Investig. Dermatol.*, pp. 301–311, 2014.
- [50] J. M. Anderson, A. Rodriguez, and D. T. Chang, "Foreign body reaction to biomaterials," *Semin. Immunol.*, vol. 20, no. 2, pp. 86–100, 2008.
- [51] G. Wick *et al.*, "The Immunology of Fibrosis," *Annu. Rev. Immunol.*, vol. 31, no. 1, pp. 107–135, 2013.
- [52] N. G. Frangogiannis, "The immune system and cardiac repair," *Pharmacol. Res.*, vol. 58, no. 2, pp. 88–111, 2008.
- [53] M. G. St. John Sutton and N. Sharpe, "Left ventricular remodeling after myocardial

- infarction: Pathophysiology and therapy," *Circulation*, vol. 101, no. 25, pp. 2981–2988, 2000.
- [54] P. Kong, P. Christia, and N. G. Frangogiannis, "The Pathogenesis of Cardiac Fibrosis," *Cell. Mol. life Sci.*, vol. 71, no. 4, pp. 91–103, 2014.
- [55] N. G. Frangogiannis, "Pathophysiology of myocardial infarction," *Compr. Physiol.*, vol. 5, no. 4, pp. 1841–1875, 2015.
- [56] K. Stokes, J. Anderson, R. McVenes, and C. McClay, "The encapsulation of polyurethane-insulated transvenous cardiac pacemaker leads," *Cardiovasc. Pathol.*, vol. 4, no. 3, pp. 163–171, 1995.
- [57] A. Wrzeszcz *et al.*, "Hydrogel coated and dexamethasone releasing cochlear implants: Quantification of fibrosis in guinea pigs and evaluation of insertion forces in a human cochlea model," *J. Biomed. Mater. Res. - Part B Appl. Biomater.*, vol. 103, no. 1, pp. 169–178, 2015.
- [58] W. Kenneth Ward, "A review of the foreign-body response to subcutaneously-implanted devices: the role of macrophages and cytokines in biofouling and fibrosis.," *J. Diabetes Sci. Technol.*, vol. 2, no. 5, pp. 768–77, 2008.
- [59] A. Lecomte, "Conception and characterization of flexible microelectrodes for implantable neuroprosthetic development," 2016.
- [60] C. Newbold *et al.*, "Changes in biphasic electrode impedance with protein adsorption and cell growth.," *J. Neural Eng.*, vol. 7, no. 5, p. 056011, 2010.
- [61] A. Bohl *et al.*, "Development of a specially tailored local drug delivery system for the prevention of fibrosis after insertion of cochlear implants into the inner ear," *J. Mater. Sci. Mater. Med.*, vol. 23, no. 9, pp. 2151–2162, 2012.
- [62] D. Schwartzman, I. Chang, J. J. Michele, M. S. Mirotznik, and K. R. Foster, "Electrical Impedance Properties of Normal and Chronically Infarcted Left Ventricular Myocardium," *J. Interv. Card. Electrophysiol.*, vol. 3, no. 3, pp. 213–224, 1999.
- [63] J. Picálek and J. Kolafa, "Molecular dynamics study of conductivity of ionic liquids: The Kohlrausch law," *J. Mol. Liq.*, vol. 134, no. 1-3 SPEC. ISS., pp. 29–33, 2007.
- [64] S. Gabriel, R. W. Lau, and C. Gabriel, "The dielectric properties of biological tissues: II. Measurements in the frequency range 10 Hz to 20 GHz," *Phys. Med. Biol.*, vol. 41, no. 11, pp. 2251–2269, 1996.
- [65] J. Malmivuo and R. Plonsey, *Bioelectromagnetism, Principle and applications of Bioelectric and Biomagnetic Fields*, Oxford Uni. 1995.
- [66] R. Plonsey and R. C. Barr, *Bioelectricity, a quantitative approach*, Springer. 2007.
- [67] H. P. Schwan, "Electrical properties of tissues and cell suspensions: mechanisms and models," *Proc. 16th Annu. Int. Conf. IEEE Eng. Med. Biol. Soc.*, pp. 70–71, 1994.
- [68] C. Gabriel, S. Gabriel, and E. Corthout, "The dielectric properties of biological tissues: I. Literature survey," *Phys. Med. Biol.*, vol. 41, no. 11, pp. 2231–2249, 1996.
- [69] S. Gabriel, R. W. Lau, and C. Gabriel, "The dielectric properties of biological tissues: III. Parametric models for the dielectric spectrum of tissues," *Phys. Med. Biol.*, vol. 41, no. 11, pp. 2271–2293, 1996.
- [70] H. P. Schwan and S. Takashima, "Electrical Conduction and Dielectric Behavior in

Biological Systems," *Encycl. Appl. Phys.*, 2003.

- [71] K. S. Cole, *Membranes, Ions, and Implulses*, Springer. 1976.
- [72] E. H. Grant, "Biological effects of microwaves and radio waves," *IEE Proc. A Phys. Sci. Meas. Instrumentation. Manag. Educ. Rev.*, vol. 128, no. 9, pp. 602–606, 1981.
- [73] D. A. Dean, T. Ramanathan, D. Machado, and R. Sundararajan, "Electrical Impedance Spectroscopy Study of Biological Tissues," *Bone*, vol. 23, no. 1, pp. 1–7, 2011.
- [74] K. S. Cole and R. H. Cole, "Dispersion and Absorption in Dielectrics I. Alternating Current Characteristics," *J. Chem. Phys.*, vol. 9, no. 4, p. 341, 1941.
- [75] H. P. Schwan and C. F. Kay, "The Conductivity of Living Tissues," *Ann. N. Y. Acad. Sci.*, vol. 65, no. 6, pp. 1007–1013, 1957.
- [76] A. L. Hodgkin and A. F. Huxley, "A quantitative description of membrane current and its application to conduction and excitation in nerve," *J. Physiol.*, vol. 117, pp. 500–544, 1952.
- [77] H. Fricke and S. Morse, "The electric resistance and capacity of blood for frequencies between 800 and 4,5 million cycles," *J. Gen. Physiol.*, vol. 9, no. 2, pp. 153–167, 1925.
- [78] H. Fricke, "A MATHEMATICAL TREATMENT OF THE ELECTRIC CONDUCTIVITY AND CAPACITY OF DISPERSE SYSTEMS," *Phys. Rev.*, vol. 26, no. 5, pp. 678–681, 1925.
- [79] E. T. McAdams and J. Jossinet, "Tissue impedance: A historical overview," *Physiol. Meas.*, vol. 16, no. 3A, 1995.
- [80] H.-J. Yoo and C. van Hoof, *Bio-Medical CMOS ICs*. 2011.
- [81] L. a Geddes, "Historical evolution of circuit models for the electrode-electrolyte interface," *Ann. Biomed. Eng.*, vol. 25, no. 1, pp. 1–14, 1997.
- [82] D. R. Merrill, M. Bikson, and J. G. R. Jefferys, "Electrical stimulation of excitable tissue: Design of efficacious and safe protocols," *J. Neurosci. Methods*, vol. 141, no. 2, pp. 171–198, 2005.
- [83] A. J. Bard and L. R. Faulkner, *Electrochemical Methods: Fundamentals and Applications*, John Wiley. 2001.
- [84] P. Ben Ishai, M. S. Talary, A. Caduff, E. Levy, and Y. Feldman, "Electrode polarization in dielectric measurements: a review," *Meas. Sci. Technol.*, vol. 24, no. 10, p. 102001, 2013.
- [85] H. Helmholtz, "Studien über Electriche Grenzsichten," *Ann. der Phys. und Chemie*, vol. 7, p. 22, 1879.
- [86] H. Fricke, "The theory of electrolytic polarization," *London, Edinburgh, Dublin Philos. Mag. J. Sci.*, vol. 14, no. 90, pp. 310–318, 1932.
- [87] J. R. MacDonald and W. B. Johnson, *Impedance Spectroscopy: Emphasizing Solid Materials and Systems*, Australia: 1987.
- [88] H. P. Schwan, "Electrode Polarization Impedance and Measurements in Biological Materials," *Ann. N. Y. Acad. Sci.*, vol. 148, no. 1, pp. 191–209, 1968.
- [89] E. Jorge, G. Amorós-Figueras, T. García-Sánchez, R. Bragós, J. Rosell-Ferrer, and J. Cinca, "Early detection of acute transmural myocardial ischemia by the phasic systolic-diastolic changes of local tissue electrical impedance," *Am. J. Physiol. Circ.*

- Physiol.*, vol. 310, no. 3, pp. H436–H443, 2016.
- [90] M. Min, R. Land, T. Paavle, T. Parve, P. Annus, and D. Trebbels, “Broadband spectroscopy of dynamic impedances with short chirp pulses,” *Physiol. Meas.*, vol. 32, no. 7, pp. 945–958, 2011.
- [91] U. Pliquet, “Time-domain based impedance measurement: Strengths and drawbacks,” *J. Phys. Conf. Ser.*, vol. 434, no. 1, 2013.
- [92] T. Sun, S. Gawad, C. Bernabini, N. G. Green, and H. Morgan, “Broadband single cell impedance spectroscopy using maximum length sequences: Theoretical analysis and practical considerations,” *Meas. Sci. Technol.*, vol. 18, no. 9, pp. 2859–2868, 2007.
- [93] B. Sanchez, G. Vandersteen, R. Bragos, and J. Schoukens, “Basics of broadband impedance spectroscopy measurements using periodic excitations,” *Meas. Sci. Technol.*, vol. 23, no. 10, 2012.
- [94] S. Grimnes and Ø. G. Martinsen, “Sources of error in tetrapolar impedance measurements on biomaterials and other ionic conductors,” *J. Phys. D. Appl. Phys.*, vol. 40, no. 1, pp. 9–14, 2007.
- [95] T. K. Bera, “Bioelectrical impedance methods for noninvasive health monitoring: A review,” *J. Med. Eng.*, vol. 2014, 2014.
- [96] D. A. Schoeller, “Bioelectrical Impedance Analysis What Does It Measure?,” *Ann. N. Y. Acad. Sci.*, vol. 904, no. 1, pp. 159–162, 2000.
- [97] L. W. Pinto, S. V. Gandra, M. D. C. Alves, I. Gomes, and E. B. Sternick, “Bioelectrical impedance analysis of body composition : influence of a newly implanted cardiac device,” vol. 8, no. May, pp. 60–65, 2017.
- [98] A. P. Hills and N. M. Byrne, “Bioelectrical impedance and body composition assessment,” *Malays. J. Nutr.*, vol. 4, pp. 107–112, 1998.
- [99] M. Nahvi and B. S. Hoyle, “Electrical Impedance Spectroscopy Sensing for Industrial Processes,” *Sensors J.*, vol. 9, no. 12, pp. 1808–1816, 2009.
- [100] A. Lasia, “Electrochemical Impedance Spectroscopy and its Applications,” *Mod. Asp. Electrochem.*, vol. 32, pp. 143–248, 1999.
- [101] M.-G. Olivier and M. Poelman, *Use of Electrochemical Impedance Spectroscopy (EIS) for the Evaluation of Electrocoatings Performances, Recent Researches*. InTech, 2012.
- [102] J. Estrela Da Silva, J. P. Marques De Sá, and J. Jossinet, “Classification of breast tissue by electrical impedance spectroscopy,” *Med. Biol. Eng. Comput.*, vol. 38, no. 1, pp. 26–30, 2000.
- [103] A. Akhavan and F. Rajabipour, “Evaluating ion diffusivity of cracked cement paste using electrical impedance spectroscopy,” *Mater. Struct. Constr.*, vol. 46, no. 5, pp. 697–708, 2013.
- [104] M. Tiitta and H. Olkkonen, “Electrical impedance spectroscopy device for measurement of moisture gradients in wood,” *Rev. Sci. Instrum.*, vol. 73, no. 8, p. 3093, 2002.
- [105] S. Mancuso, *Measuring Roots, an updated approach*. 2012.
- [106] S. Ha *et al.*, “Microfluidic Electric Impedance Spectroscopy for,” *Int. Conf.*

*Miniaturized Syst. Chem. Life Sci.*, vol. 29, pp. 1960–1962, 2012.

- [107] A. Alsamuraee and H. Jaafer, “Electrochemical impedance spectroscopic evaluation of corrosion protection properties of polyurethane /polyvinyl chloride blend coatings on steel,” *Am. J. Sci. Ind. Res.*, vol. 2, no. 5, pp. 761–768, 2011.
- [108] P. M. Gomadam and J. W. Weidner, “Analysis of electrochemical impedance spectroscopy in proton exchange membrane fuel cells,” *Int. J. Energy Res.*, vol. 29, no. 12, pp. 1133–1151, 2005.
- [109] J. Yu and C. C. Liu, “Microfabricated thin film impedance sensor & AC impedance measurements,” *Sensors*, vol. 10, no. 6, pp. 5845–5858, 2010.
- [110] M. Grossi and B. Riccò, “Electrical impedance spectroscopy (EIS) for biological analysis and food characterization: A review,” *J. Sensors Sens. Syst.*, vol. 6, no. 2, pp. 303–325, 2017.
- [111] H. H. Woltjer, H. J. Bogaard, and P. M. J. M. De Vries, “The technique of impedance cardiography,” *Eur. Heart J.*, vol. 18, no. 9, pp. 1396–1403, 1997.
- [112] R. P. Patterson, “Fundamentals of Impedance Cardiography,” *Eng. Med. Biol. Mag.*, vol. 8, no. 1, pp. 35–38, 1989.
- [113] B. H. Brown, “Electrical impedance tomography (EIT): A review,” *J. Med. Eng. Technol.*, vol. 27, no. 3, pp. 97–108, 2003.
- [114] T. K. Bera, “Noninvasive Electromagnetic Methods for Brain Monitoring: A Technical Review,” *Intell. Syst. Ref. Libr.*, vol. 74, pp. 51–95, 2015.
- [115] M. H. F. Ribeiro, R. W. Dos Santos, L. P. S. Barra, and F. C. Peters, “Simulation study on the determination of cardiac ejection fraction by electrical impedance tomography using a hybrid heuristic approach,” *J. Med. Imaging Heal. Informatics*, vol. 4, no. 1, pp. 113–121, 2014.
- [116] G. Amorós-Figueras, E. Jorge, T. García-Sánchez, R. Bragós, J. Rosell-Ferrer, and J. Cinca, “Recognition of Fibrotic Infarct Density by the Pattern of Local Systolic-Diastolic Myocardial Electrical Impedance,” *Front. Physiol.*, vol. 7, no. August, 2016.
- [117] S. Park, N. B. Nguyen, A. Pezhouman, and R. Ardehali, “Cardiac fibrosis: potential therapeutic targets,” *Transl. Res.*, vol. 209, pp. 121–137, 2019.
- [118] M. A. Branch, T. F. Coleman, and Y. Li, “A subspace, interior, and conjugate gradient method for large-scale bound-constrained minimization problems\*,” *SIAM J. Sci. Comput.*, vol. 21, no. 1, pp. 1–23, 1999.
- [119] M. J. D. Powell, “An efficient method for finding the minimum of a function of several variables without calculating derivatives,” *Comput. J.*, vol. 7, no. 2, pp. 155–162, 1964.
- [120] ACEA Biosciences, “RTCA MP Instrument Operator’s Manual,” *RTCA MP Instrum. Oper. Man.*, no. October, p. 14, 2017.
- [121] XCELLigence, *Real-Time and Dynamic Monitoring of Cell Proliferation and Viability for Adherent Cells*, no. 1. 2013, pp. 1–8.
- [122] ACEA Biosciences, “Calculation principles of RTCA Software,” *xCELLigence Syst. Tech. Note No. 2*, no. 2, 2010.
- [123] H. E. Olivey, N. A. Mundell, A. F. Austin, and J. V. Barnett, “Transforming growth

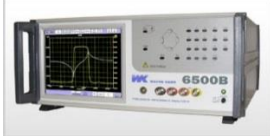
- factor- $\beta$  stimulates epithelial-mesenchymal transformation in the proepicardium," *Dev. Dyn.*, vol. 235, no. 1, pp. 50–59, 2006.
- [124] N. Guan, J. Deng, T. Li, X. Xu, J. T. Irelan, and M. W. Wang, "Label-free monitoring of T cell activation by the impedance-based xCELLigence system," *Mol. Biosyst.*, vol. 9, no. 5, pp. 1035–1043, 2013.
- [125] V. V. Petrov, R. H. Fagard, and P. J. Lijnen, "Stimulation of collagen production by TGF- $\beta$  1 during differentiation of cardiac fibroblasts to myofibroblasts," *Am. J. Hypertens.*, vol. 39, no. 2, pp. 285–263, 2002.
- [126] T. M. Jayawardena *et al.*, "MicroRNA-mediated in vitro and in vivo direct reprogramming of cardiac fibroblasts to cardiomyocytes," *Circ. Res.*, vol. 110, no. 11, pp. 1465–1473, 2012.
- [127] F. Spörl *et al.*, "Real-time monitoring of membrane cholesterol reveals new insights into epidermal differentiation," *J. Invest. Dermatol.*, vol. 130, no. 5, pp. 1268–1278, 2010.
- [128] S. K. Steinbach *et al.*, "Directed differentiation of skin-derived precursors into functional vascular smooth muscle cells," *Arterioscler. Thromb. Vasc. Biol.*, vol. 31, no. 12, pp. 2938–2948, 2011.
- [129] B. Mammadov, N. Karakas, and S. Isik, "Comparison of long-term retinoic acid-based neural induction methods of bone marrow human mesenchymal stem cells," *Vitr. Cell. Dev. Biol. - Anim.*, vol. 47, no. 7, pp. 484–491, 2011.
- [130] G. Rajaraman *et al.*, "Optimization and scale-up culture of human endometrial multipotent mesenchymal stromal cells: Potential for clinical application," *Tissue Eng. - Part C Methods*, vol. 19, no. 1, pp. 80–92, 2013.
- [131] A. H. Kramer, J. Joos-Vandewalle, A. L. Edkins, C. L. Frost, and E. Prinsloo, "Real-time monitoring of 3T3-L1 preadipocyte differentiation using a commercially available electric cell-substrate impedance sensor system," *Biochem. Biophys. Res. Commun.*, vol. 47, no. 5, 2013.
- [132] C. K. Nagaraju *et al.*, "Myofibroblast Phenotype and Reversibility of Fibrosis in Patients With End-Stage Heart Failure," *J. Am. Coll. Cardiol.*, vol. 73, no. 18, pp. 2267–2282, 2019.
- [133] H. Zhao *et al.*, "Microengineered in vitro model of cardiac fibrosis through modulating myofibroblast mechanotransduction.," *Biofabrication*, vol. 6, no. 4, p. 045009, 2014.
- [134] G. Yan *et al.*, "Application of Real-Time Cell Electronic Analysis System in Modern Pharmaceutical Evaluation and Analysis," *Molecules*, vol. 23, no. 12, p. 3280, 2018.
- [135] B. Sanchez, G. Vandersteen, R. Bragos, and J. Schoukens, "Basics of broadband impedance spectroscopy measurements using periodic excitations," *Meas. Sci. Technol.*, vol. 23, no. 10, 2012.
- [136] B. Sanchez, G. Vandersteen, R. Bragos, and J. Schoukens, "Optimal multisine excitation design for broadband electrical impedance spectroscopy," *Meas. Sci. Technol.*, vol. 22, no. 11, 2011.
- [137] S. Nag and N. V. Thakor, "Implantable neurotechnologies: electrical stimulation and applications," *Med. Biol. Eng. Comput.*, vol. 54, no. 1, pp. 63–76, 2016.

- [138] J. Castelli *et al.*, “An IC-based controllable stimulator for respiratory muscle stimulation investigations,” *Proc. Annu. Int. Conf. IEEE Eng. Med. Biol. Soc. EMBS*, pp. 1970–1973, 2017.
- [139] S. B. Weinstein and P. M. Ebert, “Data transmission by frequency-division multiplexing using the Discrete Fourier Transform,” *IEEE Trans. Commun. Technol.*, vol. 19, no. 5, pp. 628–634, 1971.
- [140] E. De Roux *et al.*, “Orthogonal Multitone Electrical Impedance Spectroscopy (OMEIS) for the Study of Fibrosis Induced by Active Cardiac Implants,” *J. Sensors*, vol. 2019, pp. 1–14, 2019.
- [141] J. Rother *et al.*, “Crosstalk of cardiomyocytes and fibroblasts in co-cultures,” *Open Biol.*, vol. 5, no. 6, 2015.
- [142] X. Zhao, J. Y. Y. Kwan, K. Yip, P. P. Liu, and F.-F. Liu, “Targeting metabolic dysregulation for fibrosis therapy,” *Nat. Rev. Drug Discov.*, 2019.

# ANNEXE A

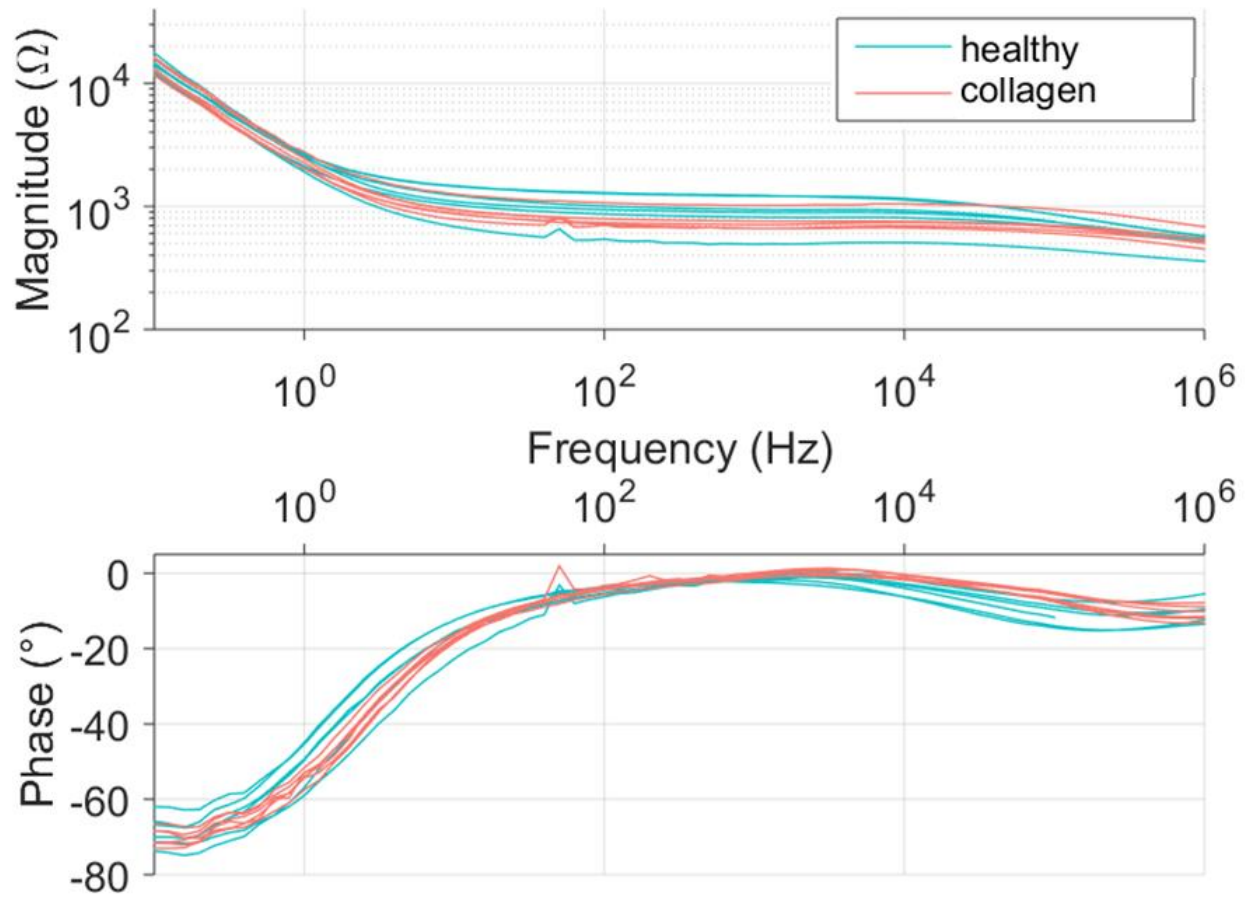
## Summary of different impedance analysers

	<i>Keysight E5061B</i>	<i>Keysight E4990A</i>	<i>Wayne-Kerr 6500B</i>	<i>Solartron 1260A</i>	<i>HIOKI IM3570</i>
<i>Type</i>	Network analyser	Impedance analyser	Impedance analyser	Impedance analyser	Impedance analyser
<i>Frequency range</i>	5 Hz - 30 MHz	20 Hz - 10/20/30/50/120 MHz	20 Hz- 10/15/20/30/50/120 MHz	10 µHz-32 MHz	4 Hz-5 MHz
<i>Resolution</i>	1 mHz	1 mHz	0.1 mHz	10 µHz (dans la gamme 10 µHz - 655.36 Hz voir les détails dans la datasheet)	10 mHz
<i>Measurable impedance range</i>	1 Ω - 20 kΩ	25 mΩ - 40 MΩ	NC	10 mΩ - 100 MΩ	100 mΩ - 100 MΩ
<i>Power output</i>	-45 to 10 dBm	NC	NC	NC	NC
<i>Sweeping</i>	-Linear, logarithmic, segment frequency sweep, -Power sweep, -DC bias sweep.	-Linear, logarithmic, segment frequency sweep, -OSC level -Log DC, DC bias (voltage and current)	-Frequency, -Drive level, -DC bias.	-Frequency (log or lin), -AC/DC voltage, -AC/DC current,	Sweeps with measurement frequency and measurement level
<i>Measurable parameters</i>		Z , θz,  Y , θy, Cp, Cs, Lp, Ls, Rp, Rs (R), D, Q, X, G, B, Complex Z, Complex Y	Z, Ø, C, Dissipation Factor (D), L, Q, R, X, G, B, Y.	Inputs V1, V2, I, V2/V1, V1/V2, <b>V1/I</b> , I/V1, <b>V2/I</b> , I/V2 ( <b>Impedance</b> )	Z, Y, θ, Rs (ESR), Rp, Rdc (DC resistance), X, G, B, Cs, Cp, Ls, Lp, D (tanδ), Q

<i>Precision</i>	2%	0.08%	0.05%	0.1%	0.08%
<i>Connection</i>	3 BNC, ports 1 et 2	4 BNC	4 BNC	6 ports	4 BNC
<i>Communication</i>	USB, GPIB, LAN	USB, GPIB, LAN	GPIB, LAN	GPIB, RS-423, RS 232	GPIB, LAN, RS-232, USB
					

# ANNEXE B

Graph representing all the impedance measurements on the 6 swine ventricles, performed with the SprintQuattro lead.



# ANNEXE C

Graph representing all the impedance measurements on 4 sheeps' ventricles, performed with the SprintQuattro lead.

